A Robust Consistent Hybrid Finite-Volume/Particle Method for Solving the PDF Model Equations of Turbulent Reactive Flows

Reza Mokhtarpoor

A Dissertation
Presented to the Collage of Engineering
of Koc University
in Candidacy for the Degree
of Doctor of Philosophy

Recommended for Acceptance
by the Department of
Mechanical Engineering
Adviser: Associate Professor Metin Muradoglu

August 2014

© Copyright by Reza Mokhtarpoor, 2014.

All rights reserved.

Koc University

Graduate School of Sciences and Engineering

This is to certify that I have examined this copy of a PhD thesis by

Reza Mokhtarpoor

and have found that it is complete and satisfactory in all respects,

and that any and all revisions required by the final

examining committee have been made.

Committee Members:

Metin Muradoglu, Ph. D. (Advisor)

Murat Sozer, Ph. D.

Selman Nas, Ph. D.

Mine Caglar, Ph. D.

Ayse Gul Gungor, Ph. D.

Date: 11.08.2014

Abstract

A new robust hybrid finite-volume (FV)/particle method is developed for solving joint probability density function (JPDF) model equations of statistically stationary turbulent reacting flows. The method is designed to remedy the deficiencies of the hybrid algorithm developed by Muradoglu et al. [40, 39]. The density-based FV solver in the original hybrid algorithm has been found to be excessively dissipative and yet not very robust. To remedy these deficiencies, a pressure-based PISO algorithm in the open source FV package, OpenFOAM, is used to solve the Favre-averaged mean mass and momentum equations while a particle-based Monte Carlo algorithm is employed to solve the fluctuating velocity-turbulence frequency-composition JPDF transport equation. The mean density is computed as a particle field and passed to the FV method. Thus the redundancy of the density fields in the original hybrid method is removed making the new hybrid algorithm more consistent at the numerical solution level. The new hybrid algorithm is first applied to simulate non-swirling cold and reacting bluff-body flows. The convergence of the method is demonstrated. In contrast with the original hybrid method, the new hybrid algorithm is very robust with respect to grid refinement and achieves grid convergence without any unphysical vortex shedding in the cold bluff-body flow case. In addition, the results are found to be in good agreement with the earlier PDF calculations and also with the available experimental data. Then the new hybrid algorithm is successfully applied to simulate the more complicated Sydney swirling bluff-body flame 'SM1'. The method is also very robust for this difficult test case and the results are in good agreement with the available experimental data. In all the cases, the PISO-FV solver is found to be highly resilient to the noise in the mean density field extracted from the particles. Finally the method is coupled with the ISAT algorithm [53] for efficient treatment of detailed chemistry. Extensive calculations have been performed for the swirling and non-swirling bluff-body flames using ISAT.

ÖZET

Reaksiyon içeren türbülanslı akışların modellenmesinde yaygın olarak kullanılan birleşik olasılık yoğunluk fonksiyonu (BOYF) model denklemlerinin istatistiki olarak zamandan bağımsız çözümü için yeni bir gürbüz hibrit sonlu-hacimler/parçacık-tabanlı Monte Carlo metodu geliştirilmiştir. Bu yöntem Muradoğlu vd. [40, 39] tarafından geliştirilen hibrit yöntemin bazı önemli yetersizliklerini gidermek için dizayn edilmiştir. Yapılan birçok alev simülasyonunda, orijinal hibrit algoritmasındaki yoğunluk-tabanlı sonlu-hacimler çözücüsünün aşırı disipatif olduğu ve yeterince gürbüz olmadığı gözlenmiştir. Bu yetersizlikleri gidermek amacıyla, açık kaynak kodlu, OpenFOAM, paketinde mevcut olan basınç-tabanlı PISO algoritması, Favre-ortalamalı kütle ve momentum denklemlerinin çözümü için kullanılmıştır. Buna paralel olarak çalkantı hızları-türbülans frekansı-kimyasal kompozisyon BOYF'nun taşınım denklemi iseparçacık-tabanlı Monte Carlo algoritması kullanılarak çözülmüştür.Bu sonlu-hacimler ve partikül yöntemleri daha sonra tutarlı hibrit metodu çerçevesinde birleştirilmiştir. Sonlu- hacimler ve partikül yöntemleriyle çözülen bütün denklemler doğrudan modellenmiş BOYF taşınım denkleminden elde edildiğinden, mevcut hibrit metot çözülen denklemler açısından tamamıyla tutarlıdır. Buna ilave olarak, eski hibrit metodundan farklı olarak, mevcut hibrit yöntemde ortalama yoğunluk parçacık kodu tarafından hesaplanmakta ve sonlu-hacim algoritmasına gönderilmektedir. Bu sayede orijinal hibrit metodunda gereğinden fazla olan yoğunluk alanı elimine edilmiş ve dolayısı ile yeni hibrit yönteminin sayısal çözüm seviyesinde çok daha tutarlı olmasını sağlamıştır. Ayrıca basınç tabanlı sonlu-hacimler yöntemi sayesinde aşırı sayısal difüzyonun oluşması engellenmiş ve her akış için kalibre edilmesi gereken hiçbir parametreye ihtiyaç kalmamıştır. Yeni hibrit yöntemi ilk olarak reaksiyon içermeyen (soğuk) ve reaksiyon içeren küt-cisim akışlarına uygulanmıştır. Yöntemin istatistiki olarak zamandan bağımsız çözüme başarı ile ulaştığı ve çözüm ağı yakınsaması gösterilmiştir. Orijinal hibrit yönteminin aksine, yeni hibrit algoritmasının çözüm ağının sıklaştırmasına karşı son derece gürbüz olduğu ve hiçbir şekilde fiziksel olmayan akım ayrılmasına yol açmadığı tespit edilmiştir. Ayrıca deterministtik bias hatasının hibrit yöntemde esas itibarı ile elimine edildiği ve dolayısı ile eski hibrit yönteminin en önemli avantajının muhafaza edildiği gösterilmiştir. Buna ek olarak mevcut yöntemle elde edilen sonuçların, daha önceki BOYF hesaplamalarıyla ve deneysel verilerle uyumlu olduğu görülmüştür. Daha sonra yeni hibrit yöntemi çok daha kompleks olan Sydney girdaplı küt-cisim alevi (SM1)'e başarıyla uygulanmıştır. Yöntemin son derece zor olan bu alev için de çok gürbüz olduğu ve hesaplama sonuçlarının deneysel verilerle uyumlu olduğu gösterilmiştir. Son olarak mevcut hibrit yöntemi ISAT algoritmasıyla birleştirilmiş ve bu sayede türbülanslı alevlerin simülasyonlarında detaylı kimyasal kinetik modellerinin kullanılabilmesine imkân sağlanmıştır. ISAT ile birleştirilen yeni hibrit yöntemi ARM2 detaylı kimyasal kinetik modeli kullanılarak girdapsız ve girdaplı küt-cisimle stabilize edilmiş türbülanslı alevlere başarı ile uygulanmış ve sayısal sonuçların daha önceki BOYF simülasyonları ve deneysel verilerle uyumlu olduğu gösterilmiştir. Simülasyonu yapılan bütün akışlarda, partikül kodunda hesaplanan ortalama yoğunluk alanının çok fazla istatistiki gürültü hatası içerse bile basınç-tabanlı sonlu hacimler yönteminde kararsızlığa yol açmadığı ve sonlu- hacimler yönteminin son derece gürbüz olduğu tespit edilmiştir.

Acknowledgements

First of all, I would like to express my special gratitude to my advisor Prof. Metin Muradoglu for all his continuous support, advices and efforts during my PhD research. I would also like to thank my dissertation committee for their encouragement.

It goes without saying that I would love to thank all my friends, house mates and members of my research group for all the great times during this time.

I wish to express my most sincere thanks to my parents for always believing in me and being there for me.

Finally, I am grateful to the Scientific and Technical Research Council of Turkey (TUBITAK) for the support of this research through grant 111M067.

To my parents.

Contents

Abstract iii

Abstract iv

Acknowledgements v

List of Tables x

List of Figures xi

1 Introduction **1**

2 Formulation and Numerical Method **6**

2.1 Conservation Equations 6

2.2 Moment Closure Methods 8

2.3 PDF Methods 11

2.3.1 Definition and properties 11

2.3.2 Compositions joint PDF 13

2.3.3 The velocity-compositions joint PDF 15

2.3.4 The velocity, turbulent frequency and compositions joint PDF model 16

2.4 Model Equations 17

2.4.1 Velocity model 17

2.4.2 Turbulent frequency model 18

2.4.3 Mixing model 18

2.4.4 Chemistry model 19
2.5 The New Hybrid Algorithm 20
2.5.1 FV system 22
2.5.2 Particle system 23
2.5.3 Correction algorithms 24
2.5.4 Local particle time stepping 25
2.5.5 Coupling with the ISAT 27
2.5.6 Overall solution procedure 28

3 Bluff-Body Flows **31**
3.1 Introduction 31
3.2 Sydney Bluff-Body Burner 32
3.3 Non-Reacting Bluff-Body Flow 34
3.4 Bluff-Body Stabilized Flame 'HM1E' 38
3.4.1 Statistical stationary solution 44
3.4.2 Comparison with the earlier PDF simulations and the experimental data 44
3.4.3 Spatial error 47
3.4.4 Bias error 48
3.5 Summary 50

4 Swirling Bluff-Body Flame **60**
4.1 Introduction 60
4.2 Sydney Swirl Burner 63
4.3 Boundary Conditions 65
4.4 Results 67
4.4.1 Statistical stationary solution 67
4.4.2 Grid convergence 67

4.4.3 Comparison with the earlier PDF simulations and the experimental Data . . . 68
4.5 Summary . . . 70

5 Detailed Chemistry Calculations with ISAT **78**
5.1 Introduction . . . 78
5.2 Non-Swirling Bluff-Body Stabilized Flame . . . 83
5.2.1 Results . . . 83
5.3 Swirl-Stabilized Bluff-Body Flame 'SM1' . . . 91
5.3.1 Results . . . 92
5.4 Summary . . . 96

6 Conclusions **114**

A Supplementary Results **117**

B Model Equations in the Cylindrical Coordinate System **128**
B.1 Velocity Model . . . 128
B.2 Turbulent Frequency Model . . . 134
B.3 Mixing and Combustion Model . . . 135

C The ARM2 Augmented Reduced Chemistry Mechanism **136**

Bibliography **138**

List of Tables

2.1 Standard model constants* 19

3.1 The coordinates of probe points used to monitor statistical statinarity. 35

3.2 Flow parameters for the non-swirling bluff-body flame 'HM1E'. 43

3.3 Percentage spatial discretization error for mean and fluctuating quantities obtained with various grid resolutions. 48

3.4 Percentage bias error for mean and fluctuating quantities obtained using various number of particles per cell. 49

4.1 Flow parameters of the case 'SM1'. 65

4.2 The coordinates of the probe points for monitoring convergence history. 67

5.1 Flow parameters of the case 'HM1'. 83

C.1 The global reactions for ARM2 reduced mechanism [61]. 137

List of Figures

2.1 Flow chart of the present hybrid method. 30

3.1 Sketch of the Sydney bluff-body burner, flame propagation length and the measurement locations (left), and the photograph of the flame in operation (right) [75]. 33

3.2 Computational domain of the non-swirling bluff-body flow with boundary conditions. Location of probe points are shown with respect to the bluff-body base. See also Table 3.1 for specifications. The same computational domain is also used for the non-swirling reacting bluff-body flow. 35

3.3 The cold bluff-body flow. Time series of Favre-averaged mean axial velocity and turbulent kinetic energy at the six probe points. 36

3.4 The cold bluff-body flow. The streamlines of the mean velocity in the recirculation zone of the non-reacting bluff-body flow calculated using 256×256 grid. 37

3.5 The cold bluff-body flow. Radial profiles of the mean and rms axial and radial velocities at the axial location $x/D_b = 1.0$ (for non-reacting bluff-body flow). Present results for three different grids, i.e., 64×64, 128×128, and 256×256, are compared with the experimental measurements and previous PDF simulations performed using the old hybrid algorithm. 38

3.6 The cold bluff-body flow. Radial profiles of mean axial velocity compared with experimental data and with the PDF simulations performed using the old hybrid algorithm. 39
3.7 The cold bluff-body flow. Radial profiles of mean radial velocity compared with experimental data and with the PDF simulations performed using the old hybrid algorithm. 40
3.8 The cold bluff-body flow. Radial profiles of rms axial velocity compared with experimental data and with the PDF simulations performed using the old hybrid algorithm. 41
3.9 The cold bluff-body flow. Radial profiles of rms radial velocity compared with experimental data and with the PDF simulations performed using the old hybrid algorithm. 42
3.10 The cold bluff-body flow. The computed radial profiles of the conditional mean frequency compared with the PDF simulations obtained using the old hybrid algorithm at axial locations $x/D_b = 0.4$ and 1.0. 43
3.11 Time series of Favre-averaged mean axial velocity and turbulent kinetic energy at the six probe points. 44
3.12 The streamlines of the mean velocity in the recirculation zone of 'HM1E' flame. The top streamlines are obtained by the new algorithm and the bottom one by the old hybrid algorithm. 46
3.13 The bluff-body flame 'HM1E'. Radial profiles of mean axial velocity compared with the experimental data (symbols) and the earlier PDF simulations of Muradoglu et al. [37] (red dashed lines). 51
3.14 The bluff-body flame 'HM1E'. Radial profiles of mean radial velocity compared with the experimental data (symbols) and the earlier PDF simulations of Muradoglu et al. [37] (red dashed lines). 52

3.15 The bluff-body flame 'HM1E'. Radial profiles of rms axial velocity compared with the experimental data (symbols) and the earlier PDF simulations of Muradoglu et al. [37] (red dashed lines). 53
3.16 The bluff-body flame 'HM1E'. Radial profiles of rms radial velocity compared with the experimental data (symbols) and the earlier PDF simulations of Muradoglu et al. [37] (red dashed lines). 54
3.17 The bluff-body flame 'HM1E'. Radial profiles of mean mixture fraction compared with the experimental data (symbols) and the earlier PDF simulations of Muradoglu et al. [37] (red dashed lines). 55
3.18 The bluff-body flame 'HM1E'. Radial profiles of rms mixture fraction compared with the experimental data (symbols) and the earlier PDF simulations of Muradoglu et al. [37] (red dashed lines). 55
3.19 The bluff-body flame 'HM1E'. Grid convergence: Radial profiles of mean and rms fluctuating axial and radial velocities, mean and rms mixture fraction at axial location $x/D_b = 0.4$. 56
3.20 The bluff-body flame 'HM1E'. Grid convergence: Mean and fluctuating quantities against M^{-2} at selected points. Circles indicate the location at $(x/D_b = 1.0, r/R_j = 1)$, triangles at $(x/D_b = 1.0, r/R_b = 0.5)$, squares at $(x/D_b = 1.0, r/R_b = 1.0)$, and the solid lines show the linear least squares fits to the computational results. 57
3.21 The bluff-body flame 'HM1E'. Bias error: Radial profiles of mean and rms fluctuating axial and radial velocities, mean and rms mixture fraction at axial location $x/D_b = 0.8$. 58

3.22 The bluff-body flame 'HM1E'. Bias error: Mean and fluctuating quantities against $1/N_{pc}$ at selected points. Circles indicate the location at $(x/D_b = 1.0, r/R_j = 1)$, triangles at $(x/D_b = 1.0, r/R_b = 0.5)$, squares at $(x/D_b = 1.0, r/R_b = 1.0)$, and solid lines show the linear least squares fits to the computational results. 59

4.1 Sydney swirl burner [75]. 64

4.2 Computational domain of the swirling bluff-body flame with boundary conditions. Location of monitor points are shown with respect to the bluff-body base. See also Table 4.2. 66

4.3 Time series of Favre-averaged mean axial velocity and turbulent kinetic energy at the probe points. 68

4.4 The streamlines of the mean velocity computed for the swirling bluff-body flame in the vicinity of the recirculation zones. 68

4.5 Grid convergence: the radial profiles of mean and rms fluctuating axial and radial velocities, mean and rms mixture fraction at axial location $x/D_b = 0.8$. Computations are performed using 96×96, 144×144 and 216×216 grids. 71

4.6 The radial profiles of mean axial velocity compared with the experimental data [75] and the numerical results of De Meester et al. [8]. . . 72

4.7 The radial profiles of mean tangential velocity compared with the experimental data [75] and the numerical results of De Meester et al. [8]. 73

4.8 The radial profiles of rms axial velocity compared with the experimental data [75]. 74

4.9 The radial profiles of rms tangential velocity compared with the experimental data [75]. 75

4.10 The radial profiles of mean mixture fraction compared with the experimental data [75] and the numerical results of De Meester et al. [8]. . 76

4.11 The radial profiles of rms mixture fraction compared with the experimental data [75] and the numerical results of De Meester et al. [8]. . . 77

5.1 The detailed chemistry computations of the bluff-body flame 'HM1' using the ARM2 mechanism. The radial profiles of mean axial velocity compared with the experimental data [75] 87

5.2 The detailed chemistry computations of the bluff-body flame 'HM1' using the ARM2 mechanism. The radial profiles of mean radial velocity compared with experimental data [75]. 88

5.3 The detailed chemistry computations of the bluff-body flame 'HM1' using the ARM2 mechanism. The radial profiles of the mean mixture fraction compared with the experimental data [75]. 89

5.4 The detailed chemistry computations of the bluff-body flame 'HM1' using the ARM2 mechanism. The radial profiles of the mean mass fraction of H2O compared with the experimental data [75]. 90

5.5 The detailed chemistry computations of the bluff-body flame 'HM1' using the ARM2 mechanism. The radial profiles of the mean mass fraction of CO2 compared with the experimental data and with the previous numerical simulations of Liu et al. [25]. 91

5.6 The detailed chemistry computations of the bluff-body flame 'HM1' using the ARM2 mechanism. The radial profiles of the mean mass fraction of CO compared with the experimental data and with the previous numerical simulations of Liu et al. [25]. 92

5.7 The detailed chemistry computations of the bluff-body flame 'HM1' using the ARM2 mechanism. The radial profiles of the mean mass fraction of N2 compared with the experimental data [75]. 93

5.8 The detailed chemistry computations of the bluff-body flame 'HM1' using the ARM2 mechanism. The radial profiles of the mean temperature compared with the experimental data and with numerical simulations of Liu et al. [25]. 94

5.9 The detailed chemistry computations of the bluff-body flame 'HM1' using the ARM2 mechanism. Scatter plots of the mass fractions of CO, CO2, and H2O against mixture fraction at the axial location $x/D_b =$ 0.6. The detailed chemistry results (blue-dots) are compared with the flamelet model (dashed-line) and the experimental data (red-dots) [75]. 98

5.10 The detailed chemistry computations of the bluff-body flame 'HM1' using the ARM2 mechanism. Scatter plots of the mass fractions of OH and O2, and temperature against mixture fraction at the axial location $x/D_b = 0.6$. The detailed chemistry results (blue-dots) are compared with the flamelet model (dashed-line) and the experimental data (red-dots) [75]. 99

5.11 The detailed chemistry computations of the bluff-body flame 'HM1' using the ARM2 mechanism. Scatter plots of the mass fractions of CO, CO2, and H2O against mixture fraction at the axial location $x/D_b =$ 1.3. The detailed chemistry results (blue-dots) are compared with the flamelet model (dashed-line) and the experimental data (red-dots) [75]. 100

5.12 The detailed chemistry computations of the bluff-body flame 'HM1' using the ARM2 mechanism. Scatter plots of the mass fractions of OH and O2, and temperature against mixture fraction at the axial location $x/D_b = 1.3$. The detailed chemistry results (blue-dots) are compared with the flamelet model (dashed-line) and the experimental data (red-dots) [75]. 101

5.13 The detailed chemistry computations of the bluff-body flame 'HM1' using the ARM2 mechanism. Scatter plots of the mass fractions of CO, CO2, and H2O against mixture fraction at the axial location $x/D_b = 1.8$. The detailed chemistry results (blue-dots) are compared with the flamelet model (dashed-line) and the experimental data (red-dots) [75]. 102

5.14 The detailed chemistry computations of the bluff-body flame 'HM1' using ARM2 mechanism. Scatter plots of the mass fractions of OH and O2, and temperature against mixture fraction at the axial location $x/D_b = 1.8$. The detailed chemistry results (blue-dots) are compared with the flamelet model (dashed-line) and the experimental data (red-dots) [75]. 103

5.15 The detailed chemistry computations of the swirling bluff-body flame 'SM1' using the ARM2 mechanism. The radial profiles of the mean axial velocity compared with the experimental data [75] and the numerical results of De Meester et al. [8]. 104

5.16 The detailed chemistry computations of the swirling bluff-body flame 'SM1' using the ARM2 mechanism. The radial profiles of the mean axial velocity compared with the experimental data [75] and the numerical results of De Meester et al. [8]. 105

5.17 The detailed chemistry computations of the swirling bluff-body flame 'SM1' using the ARM2 mechanism. The computed radial profiles of the mean mass fraction of H2O (solid line) compared with the experimental data (symbols) [75]. 106

5.18 The detailed chemistry computations of the swirling bluff-body flame 'SM1' using the ARM2 mechanism. The computed radial profiles of the mean mass fraction of CO2 (solid line) compared with the experimental data (symbols) [75] and also with the earlier PDF calculation of De Meester et al. (dashed-line) [8]. 107
5.19 The detailed chemistry computations of the swirling bluff-body flame 'SM1' using the ARM2 mechanism. The computed radial profiles of the mean mass fraction of CO (solid line) compared with the experimental data (symbols) [75]. 108
5.20 The detailed chemistry computations of the swirling bluff-body flame 'SM1' using the ARM2 mechanism. The computed radial profiles of the mean temperature (solid line) compared with the experimental data (symbols) [75]. 109
5.21 The detailed chemistry computations of the swirling bluff-body flame 'SM1' using the ARM2 mechanism. The computed radial profiles of the mean mixture fraction (solid line) compared with the experimental data (symbols) [75] and also with the earlier PDF calculation of De Meester et al. (dashed-line) [8]. 110
5.22 The detailed chemistry computations of the swirling bluff-body flame 'SM1' using the ARM2 mechanism. Scatter plots of temperature and mass fractions of CO2 and CO against mixture fraction at x/D_b = 0.4. The detailed chemistry results (blue-dots) are compared with the flamelet model (dashed-line) and the experimental data (red-dots) [75]. 111

5.23 The detailed chemistry computations of the swirling bluff-body flame 'SM1' using the ARM2 mechanism. Scatter plots of temperature and mass fractions of CO2 and CO against mixture fraction at x/D_b = 0.8. The detailed chemistry results (blue-dots) are compared with the flamelet model (dashed-line) and the experimental data (red-dots) [75]. 112

5.24 The detailed chemistry computations of the swirling bluff-body flame 'SM1' using the ARM2 mechanism. Scatter plots of temperature and mass fractions of CO2 and CO against mixture fraction at x/D_b = 1.5. The detailed chemistry results (blue-dots) are compared with the flamelet model (dashed-line) and the experimental data (red-dots) [75]. 113

A.1 Grid convergence for the cold bluff body flow. The radial profiles of the mean axial velocity for three different grids, i.e., 64×64, 128×128, and 256×256, are compared with the experimental measurements [75]. 118

A.2 Grid convergence for the cold bluff body flow. The radial profiles of the mean radial velocity for three different grids, i.e., 64×64, 128×128, and 256×256, are compared with the experimental measurements [75]. 119

A.3 Grid convergence for the cold bluff body flow. The radial profiles of the rms axial velocity for three different grids, i.e., 64×64, 128×128, and 256×256, are compared with the experimental measurements [75]. 120

A.4 Grid convergence for the cold bluff body flow. The radial profiles of the rms radial velocity for three different grids, i.e., 64×64, 128×128, and 256×256, are compared with the experimental measurements [75]. 121

A.5 Grid convergence for the swirling flame 'SM1'. The radial profiles of the mean axial velocity for three different grids, i.e., 96×96, 144×144, and 216×216, are compared with the experimental measurements [75]. 122

A.6 Grid convergence for the swirling flame 'SM1'. The radial profiles of the mean tangential velocity for three different grids, i.e., 96×96, 144×144, and 216 × 216, are compared with the experimental measurements [75]. 123

A.7 Grid convergence for the swirling flame 'SM1'. The radial profiles of the rms axial velocity for three different grids, i.e., 96 × 96, 144 × 144, and 216 × 216, are compared with the experimental measurements [75]. 124

A.8 Grid convergence for the swirling flame 'SM1'. The radial profiles of the rms tangential velocity for three different grids, i.e., 96 × 96, 144 × 144, and 216 × 216, are compared with the experimental measurements [75]. 125

A.9 Grid convergence for the swirling flame 'SM1'. The radial profiles of the mean mixture fraction for three different grids, i.e., 96 × 96, 144 × 144, and 216 × 216, are compared with the experimental measurements [75]. 126

A.10 Grid convergence for the swirling flame 'SM1'. The radial profiles of the rms mixture fraction for three different grids, i.e., 96 × 96, 144 × 144, and 216 × 216, are compared with the experimental measurements [75]. 127

B.1 Standard cylindrical coordinate system 130

Chapter 1

Introduction

Turbulent combustion continues to be a key technology in energy conversion systems that convert chemical energy stored in fossil fuels first into usable thermal energy and subsequently into mechanical work. Many important global issues such as energy management, climate change and pollution are directly related to the conversion of chemical energy into thermal energy via combustion that usually takes place in turbulent environment mainly due to the enhanced mixing. Accurate prediction of turbulent reacting flows is thus of fundamental importance for designing more efficient energy conversion systems and reducing the impact on the environment.

Although the Navier-Stokes equations are known to be the correct mathematical model for turbulent flows, the direct numerical simulation (DNS) is still limited to simple flows with low or moderate Reynolds numbers due to rapidly increasing computational cost with Reynolds number. In probability density function (PDF) methods, turbulent flows are modeled by a one-point, one-time joint PDF of selected flow properties. The PDF method takes full account of the stochastic nature of turbulent flows and offers the distinct advantages of being able to treat the important processes of convection and non-linear chemical reactions without any assumptions or approximations–a capability not possible by any other approaches. In particular,

the exact treatment of non-linear chemical reactions makes the PDF approach highly attractive for turbulent reacting flows. Owing to these unique features, the joint PDF method coupled with a detailed chemistry model can correctly model the challenging processes of local extinction and re-ignition, i.e., the key processes that critically influence the stability of turbulent flames, quality of combustion and air pollution, as demonstrated by Xu and Pope [71] and Tang et al. [64].

As for any turbulence model, an efficient numerical solution algorithm is of crucial importance in PDF methods. A significant progress has been made in this direction by the development of the consistent hybrid finite-volume (FV)/particle-based Monte Carlo method [40, 39, 20]. It has been shown that the consistent hybrid method is up to 100 times more efficient than the best available alternative solution algorithm, i.e., the self-contained particle-mesh method implemented in *pdf2dv* code [49]. The major advantage of the hybrid method comes from the fact that it combines the best features of the FV and particle methods and avoids their respective deficiencies when used alone. It has been shown that it virtually eliminates the bias error and significantly reduces the statistical noise in mean fields [40, 20].

In addition, the hybrid method can be easily coupled with existing flow solvers including the commercial CFD packages. In the original hybrid method [40, 39], a density-based finite-volume solver is used to solve the mean mass, momentum and energy conservation equations while a particle-based Monte-Carlo algorithm is employed to solve the transport equation of the joint PDF for the fluctuating velocity, turbulent frequency and compositions. The method is fully consistent at the level of the governing equations since they are directly derived from the modeled joint PDF transport equation. In addition, a full consistency at the numerical level is achieved by the correction algorithms developed by Muradoglu et al. [39]. This original hybrid method is referred as *old hybrid* algorithm from now on. Although the old hybrid method coupled with the correction algorithms has been successfully applied to vari-

ous turbulent flames [5, 21, 25, 37], it has been found to be excessively diffusive and yet not very robust mainly due to stiffness of the compressible flow equations in the incompressible or nearly incompressible limit, i.e., when Mach number $Ma \ll 1$ [21]. Preconditioning methods are commonly used to remove the stiffness of the compressible flow equations at low Mach numbers [66, 65]. The major drawback of the preconditioning method is the lack of robustness especially near the stagnation points where the preconditioning matrix becomes nearly singular [10]. The preconditioning method developed by Muradoglu and Caughey [41] was employed in the FV solver used in the old hybrid method. In addition to the well known lack of robustness in the vicinity of stagnation points, it has been found that the preconditioning parameters are very sensitive to flow conditions and must be adjusted carefully for each flow to avoid excessive numerical dissipation while maintaining numerical stability [21].

In particular, the previous versions of the hybrid algorithm failed to achieve a grid convergence for the non-reacting bluff-body flow [21]. When the grid is refined more than a threshold, the loosely-coupled [39] hybrid solver resulted in a vortex shedding that has not been observed experimentally [7]. It was not clear whether this unphysical behavior was due to the models used or due to the excessive numerical dissipation in the density-based FV solver. The primary purpose of the present study is to remedy these deficiencies by replacing the density-based FV solver with a pressure-based FV algorithm and thus create a robust PDF solution algorithm for low Mach number flows. Here "robustness" refers to the ability of the method to maintain the stability with respect to grid refinement for a wide range of flow conditions without excessive numerical dissipation.

For this purpose, the particle based Monte Carlo algorithm is combined with the open source FV package, OpenFOAM [74], that is freely available from the Internet. The OpenFOAM package contains several pressure-based flow solvers and various turbulence models including a variety of Reynolds averaged Navier-Stokes (RANS)

and large eddy simulation (LES) models. In the present study, the constant-density FV solver utilizing the PISO algorithm [18] is first modified for variable density flows and then coupled with the particle algorithm as follows: The mean velocity and mean pressure fields are supplied to the particle code by the FV solver which in turn gets all the Reynolds stresses and mean density fields from the particle code. It is emphasized here that the present hybrid algorithm is completely consistent at the level of governing equations solved by the particle and FV algorithms as in the old hybrid approach. In addition, the velocity and position correction algorithms developed by Muradoglu et al. [39] are used to enforce full consistency at the numerical solution level. The energy correction algorithm is not needed in the present hybrid method since the mean density field is obtained from the particles as a particle field and passed to the FV method. Note that the present study is the first step and paves the way for development of a general purpose RANS/PDF and LES/PDF solution algorithm for reacting turbulent flow simulations within the OpenFOAM framework.

The new hybrid algorithm is first applied to simulate cold and reacting bluff-body flows. It is shown that the new hybrid algorithm is very robust against grid refinement. In the old hybrid method the results for non-reacting bluff-body flow [21] were presented only for grids 32×32 and 64×64 and for finer grids the method produced nonphysical vortex shedding. It has been demonstrated that the new hybrid algorithm does not show such a behavior and flow successfully reaches a statistically stationary state even for much finer grids. For determining the numerical property of the new algorithm, comprehensive calculations are performed for the Sydney buff-body stabilized flame 'HM1E'. In contrast with the old hybrid algorithm, it is found that the new hybrid method correctly captures the flow characteristics of the bluff-body flame in the recirculation region which has not been well-predicted by the original hybrid method. In addition, the convergence of the method is demonstrated for spatial and bias errors. The results are found to be in good agreement with the available exper-

imental data. For demonstrating the robustness of the new solution algorithm, the hybrid method is also applied to simulate more complicated and challenging test case of the Sydney swirl-stabilized flame 'SM1'. The new hybrid algorithm is also found to be very robust for this difficult test case and the results are in good agreement with the available experimental data as well as with the earlier PDF simulations of De Meester et al. [8].

Finally for detailed chemistry calculations, the ISAT [53] algorithm is integrated into the new hybrid algorithm to efficiently perform PDF simulations with finite-rate chemistry. For testing our implementation the Sydney non-swirling bluff-body flame which has been studied numerically by Liu et al. [25] is simulated using the ARM2 finite-rate chemistry model [61]. The results are compared with the experimental data and also with the PDF simulations of Liu et al. [25]. Then similar detailed chemistry calculations are also performed for the Sydney swirling bluff-body flame using the ARM2. The computed results are found to be overall in good agreement with the experimental data.

The thesis is organized as follows: In Chapter 2, the conservation equations for a turbulent reactive flow are described, the PDF method is briefly reviewed, and the new hybrid solution algorithm is presented. In Chapter 3, the hybrid method is applied to the cold and reacting bluff-body flows and numerical properties of the algorithm are examined in details. In Chapter 4, the hybrid algorithm is applied to simulate the swirl-stabilized bluff-body flame. In Chapter 5, the new algorithm is coupled with the ISAT algorithm to outfit the method with detailed chemistry calculations. Finally conclusions are drawn in Chapter 6.

Chapter 2

Formulation and Numerical Method

2.1 Conservation Equations

The state of a gas-phase multi-component system composed of n_s species is completely described by mass fractions $\mathbf{Y} = (Y_1, Y_2, Y_3, ..., Y_{n_s})$, specific enthalpy h, pressure p and velocity $\mathbf{U}$. The evolution of the chemically reacting turbulent flows is governed by conservation of mass, momentum, chemical species, and enthalpy [24]:

$$\begin{aligned}
\frac{\partial \rho}{\partial t} + \frac{\partial}{\partial x_i}(\rho U_i) &= 0, \\
\frac{\partial}{\partial t}(\rho U_i) + \frac{\partial}{\partial x_j}(\rho U_i U_j) &= -\frac{\partial p}{\partial x_i} + \frac{\partial \tau_{ij}}{\partial x_j} + \rho g_i, \\
\frac{\partial}{\partial t}(\rho Y_\alpha) + \frac{\partial}{\partial x_j}(\rho Y_\alpha U_j) &= -\frac{\partial J_i^\alpha}{\partial x_i} + \rho S_\alpha, \\
\frac{\partial}{\partial t}(\rho h) + \frac{\partial}{\partial x_j}(\rho h U_j) &= -\frac{\partial J_i^h}{\partial x_i} + \rho S_h.
\end{aligned} \tag{2.1}$$

In these equations g_i is the body force in the i-th coordinate direction, and τ_{ij} is the shear stress in the i-th coordinate direction on a surface whose outward normal is in the j-th coordinate direction. It is generally considered appropriate to assume that

the fluid in turbulent reacting flows is Newtonian and thus

$$\tau_{ij} = \mu \left(\frac{\partial U_i}{\partial x_j} + \frac{\partial U_j}{\partial x_i} - \frac{2}{3} \frac{\partial U_k}{\partial x_k} \delta_{ij} \right), \tag{2.2}$$

with a mixture-averaged viscosity, μ, and bulk viscosity is neglected [24]. In Eq. (2.1) J_i^h is the energy flux in the i-th coordinate direction due to molecular transport, J_i^α is diffusive mass fluxes of species α in the i-th coordinate direction, S_α is the mass rate of addition of species α due to chemical reaction, S_h is the the source of energy generally due to compressibility, viscous dissipation and radiation. Considering low-Mach number flow and disregarding radiation, S_h represents the source of energy due to the viscous dissipation [52, 24].

System of equations shown above are supplemented by thermal $p = p(\mathbf{Y}, T, \rho)$ and caloric $T = T(\mathbf{Y}, h, \rho)$ equations of state. For a low-Mach-number, ideal-gas, single-phase, multi-component reacting mixture, all necessary quantities (e.g., mixture density and temperature) can be determined normally from the species mass fractions, enthalpy, and a reference pressure p_0 that is, at most, a function of time [51, 16]. The equation for enthalpy can be used to obtain the temperature, given the species mass fractions, mixture specific enthalpy, and fluid properties.

$$h = \sum_{\alpha=1}^{N_s} Y_\alpha \left(\Delta h_{f,\alpha}^0 + \int_{T^0}^{T} C_{p,\alpha}(\acute{T}) d\acute{T} \right). \tag{2.3}$$

Here $\Delta h_{f,\alpha}^0$ is the enthalpy of formation of species α at reference temperature T^0, and $C_{p,\alpha}$ is the constant-pressure specific heat of the species α. Fluid properties include the specific heats $C_{p,\alpha}$ and $C_{v,\alpha}$. For ideal-gas mixtures both specific heats are function of temperature only and $C_{p,\alpha} - C_{v,\alpha} = R_\alpha = R_U / \mathcal{M}_\alpha$. Here R_α is the gas constant, R_U is the universal gas constant, and $\mathcal{M}_\alpha$ is molecular weight of species α. In the numerical solution of low-Mach-number flows, for which a pressure based solver is usually employed, the reference pressure p_0 is used in the thermal equation

of state to compute the mixture density ρ as

$$\rho = \frac{p_0}{RT} = \frac{p_0}{R_U T/\mathcal{M}} = \frac{p_0}{R_U T \sum_{\alpha=1}^{n_s} (\frac{Y_\alpha}{\mathcal{M}_\alpha})}. \tag{2.4}$$

Here R and $\mathcal{M}$ are the gas constant and molecular weight of the mixture, respectively. Conservation equations and equations of state together with the initial and boundary conditions determine the velocity, compositions, and pressure fields provided that S_α, S_h, J_i^α, and J_i^h are known.

Analytic solutions for the system of Eq. (2.1) have been obtained only for simple laminar flows. For turbulent flows, direct numerical simulation (DNS) is the only way for resolving the entire length and time scales. The advantage of this method is that no models are required for the turbulence-chemistry interactions. For inert flows, DNS is established as a numerical technique for predicting some geometrically simple flows at low and moderate Reynolds number. DNS of turbulent reacting flow is many orders of magnitude more demanding than the corresponding inert flow. This is caused by two reasons: first, a reacting flow consists of smaller length and time scales than those in the corresponding non-reacting flow and second, strongly-coupled set of scalar fields with high nonlinear source terms are much more harder to solve than the non-reacting flow equations. It can be concluded that DNS is not feasible for turbulent combustion in the practical devices and will remain so in foreseeable future.

2.2 Moment Closure Methods

An alternative approach is the moment closure methods. Using Reynolds decomposition a scalar quantity ϕ can be split into the Reynolds average mean $\langle\phi\rangle$ and fluctuating part ϕ' as

$$\phi = \langle\phi\rangle + \phi', \tag{2.5}$$

For a reacting flow more easily interpreted conservation equations are obtained by decomposing the flow quantities into the mass-weighted (Favre-averaged) $\tilde{\phi}$ and the respective fluctuating component ϕ'':

$$\phi = \tilde{\phi} + \phi'', \tag{2.6}$$

where the Favre average is defined as

$$\tilde{\phi} = \langle \rho\phi \rangle \, / \, \langle \rho \rangle \, . \tag{2.7}$$

Taking Favre mean of conservation equations of mass, momentum, chemical species, and energy yields

$$\frac{\partial \langle \rho \rangle}{\partial t} + \frac{\partial}{\partial x_i}(\langle \rho \rangle \tilde{U}_i) = 0, \tag{2.8}$$

$$\frac{\partial(\langle \rho \rangle \tilde{U}_i)}{\partial t} + \frac{\partial(\langle \rho \rangle \tilde{U}_i \tilde{U}_j)}{\partial x_j} = -\frac{\partial \langle p \rangle}{\partial x_i} + \frac{\partial \langle \tau_{ij} \rangle}{\partial x_j} - \frac{\partial(\langle \rho \rangle \widetilde{u_i'' u_j''})}{\partial x_j}, \tag{2.9}$$

$$\frac{\partial(\langle \rho \rangle \tilde{\phi}_\alpha)}{\partial t} + \frac{\partial(\langle \rho \rangle \tilde{\phi}_\alpha \tilde{U}_j)}{\partial x_j} = -\frac{\partial \langle J_i^\alpha \rangle}{\partial x_i} + \langle \rho \rangle \tilde{S}_\alpha(\mathbf{\Phi}) - \frac{\partial(\langle \rho \rangle \widetilde{\phi_\alpha'' u_j''})}{\partial x_j}. \tag{2.10}$$

Here $\mathbf{\Phi} = (\phi_1, \phi_2, ..., \phi_{ns+1})$ represents the mass fraction of n_s chemical species and enthalpy. The quantities in the above equations can be considered in three groups:
(i) $\tilde{\mathbf{U}}$, $\tilde{\mathbf{\Phi}}$, $\langle p \rangle$, $\langle \tau_{ij} \rangle$, $\langle J_i^\alpha \rangle$,
(ii) $\widetilde{u_i'' u_j''}$, $\widetilde{\Phi_\alpha'' u_j''}$,
(iii) $\langle \rho \rangle$, $\tilde{S}_\alpha(\mathbf{\Phi})$.
In group (i), $\tilde{\mathbf{U}}$ and $\tilde{\mathbf{\Phi}}$ are subject of the mean momentum and species conservation equations while $\langle p \rangle$ can be obtained by solving a Poisson equation and $\langle \tau_{ij} \rangle$ and $\langle J_i^\alpha \rangle$ can be expressed as functions of $\tilde{\mathbf{U}}$ and $\tilde{\mathbf{\Phi}}$, respectively, and thus can be easily determined. In group (ii) the Reynolds stresses $\widetilde{u_i'' u_j''}$ and turbulent scalar fluxes $\widetilde{\phi_\alpha'' u_j''}$ are unknowns and must be modeled. The principle aim of the turbulence modelling is

to express these terms in terms of known quantities. The quantities in group (iii) are functions of scalars only and most difficult term is mean reaction rate $\tilde{S}_\alpha(\mathbf{\Phi})$ which is a highly nonlinear function of compositions $\mathbf{\Phi}$. Most straightforward approximation is to express the mean reaction rate as a function of the mean scalars

$$\tilde{S}_\alpha(\mathbf{\Phi}) = \hat{S}_\alpha(\tilde{\mathbf{\Phi}}).$$

This approximation can be in error in several orders of magnitude. The mean reaction rate can be determined by the joint probability density function (PDF) of scalars, f_ϕ, by

$$\begin{aligned} \langle\rho\rangle\tilde{S}_\alpha(\mathbf{\Phi}) &= \int \rho(\mathbf{\Psi}) f_\phi(\mathbf{\Psi}) S_\alpha(\mathbf{\Psi}) d\mathbf{\Psi} \\ \text{or} \quad \tilde{S}_\alpha(\mathbf{\Phi}) &= \int \tilde{f}_\phi(\mathbf{\Psi}) S_\alpha(\mathbf{\Psi}) d\mathbf{\Psi}, \end{aligned} \tag{2.11}$$

where $\tilde{f}_\phi(\mathbf{\Psi})$ is the mass-weighted joint PDF of scalars defined as

$$\tilde{f}_\phi(\mathbf{\Psi}) = f_\phi(\mathbf{\Psi})\rho(\mathbf{\Psi})/\langle\rho\rangle,$$

In Eq. (2.11) the integration is carried out over the whole scalar space.

There are two approaches for determining the joint PDF of scalars so that the above integration can be used to calculate the mean reaction rates. The first approach is the *assumed PDF method* in which the joint PDF is assumed to have a particular form which is parametrized by its mean $\langle\phi_\alpha\rangle$ and all second moments $\langle\phi'_\alpha\phi'_\beta\rangle$ for which the modelled conservation equations are solved [13]. The second approach is the *transported PDF method* in which the (modelled) transport equation for f_ϕ or another joint PDF is solved. The transported PDF methods, discussed extensively below, are shorten as *PDF methods* from now on.

2.3 PDF Methods

2.3.1 Definition and properties

Let ϕ be a composition variable at particular time t_0 and space $\mathbf{x_0}$ in a turbulent reactive flow. It is assumed that the flow can be realized any number of times. From each realization a value for ϕ can be obtained; considering the nature of turbulence, these values are different meaning, i.e., ϕ is a random variable. In a given realization, it is not possible to predict the value of ϕ beforehand. But it is possible to ascribe probabilities to its values in a given interval. This is accomplished by a probability density function.

For every random variable, an independent sample-space is introduced. Here ψ is chosen as sample space of ϕ. The *cumulative distribution function* (CDF), $F_\phi(\psi)$, is defined as the probability that ϕ is less than ψ, i.e.,

$$F_\phi(\psi) \equiv \text{Prob}\{\phi < \psi\}. \tag{2.12}$$

The probability density function (PDF) of the scalar ϕ, $f_\phi(\psi)$, can now be defined as the derivative of the cumulative distribution function as

$$f_\phi(\psi) \equiv \frac{dF_\phi(\psi)}{d\psi}. \tag{2.13}$$

It means that the PDF is the probability per unit ψ of the event $\phi = \psi$ or, equivalently, $f_\phi(\psi)d\psi$ is the probability of the event $\psi < \phi < \psi + d\psi$.

Three fundamental properties of the PDF are:

(i) The PDF is non-negative, i.e., $f_\phi \geq 0$.

(ii) It satisfies the normalization condition, i.e., $\int_{-\infty}^{\infty} f_\phi(\psi)d\psi$=1.

(iii) For any function $Q(\phi)$ the mean or the expectation is defined as:

$$\langle Q \rangle = \int_{-\infty}^{\infty} f_\phi(\psi)Q(\psi)d\psi.$$

It is clear that if the PDF of a random variable ϕ is known, then the expectation of any function of ϕ can be calculated. In particular the mean $\langle\phi\rangle$ and the m-th central moment $\langle\phi'^m\rangle$ can be determined.

The PDF definition for a single random variable can be extended to two or more random variables. Take U and ϕ as scalar random variables with corresponding sample spaces V and ψ. The cumulative distribution function (CDF) of the joint variables (U, ϕ) is defined by

$$F_{U\phi}(V, \psi) \equiv \text{Prob}\{\phi < \psi, U < V\}. \tag{2.14}$$

The joint PDF (JPDF) of the scalars U and ϕ, $f_{U\phi}$, can now be defined as the derivative of the CDF, i.e.,

$$f_{U\phi}(V, \psi) \equiv \frac{\partial F_{U\phi}(V, \psi)}{\partial V \partial \psi}. \tag{2.15}$$

Similar to the univariate PDF, the properties of the JPDF, $f_{U\phi}$, are :

(i) The JPDF is non-negative, i.e., $f_{U\phi} \geq 0$.

(ii) It satisfies the normalization condition, i.e., $\int_{-\infty}^{\infty}\int_{-\infty}^{\infty} f_{U\phi}(V, \psi)d\psi dV$=1.

(iii) For any function $Q(U, \phi)$ the mean or the expectation is defined as:

$$\langle Q\rangle = \int_{-\infty}^{\infty}\int_{-\infty}^{\infty} f_{U\phi}(V, \psi)Q(V, \psi)d\psi dV.$$

Furthermore, the marginal PDFs $f_\phi(\psi)$ and $f_U(V)$ are derivable from the JPDF $f_{U\phi}(V, \psi)$. The integration of $f_{U\phi}(V, \psi)$ with respect to V and ψ leads to the marginal PDF $f_\phi(\psi)$ and $f_U(V)$, respectively, i.e.,

$$\begin{aligned} f_U(V) &= \int_{-\infty}^{\infty} f_{U\phi}(V, \psi)d\psi, \\ f_\phi(\psi) &= \int_{-\infty}^{\infty} f_{U\phi}(V, \psi)dV. \end{aligned} \tag{2.16}$$

The conditional PDF $f_{U|\phi}\ (V|\psi)$ (i.e., the probability of $\{V \leq U \leq V + dV\}$ conditioned on the state $\{\psi \leq \phi \leq \psi + d\psi\}$) can be calculated as the ratio of the joint PDF $f_{U\phi}$ and the marginal PDF f_ϕ, i.e.,

$$f_{U|\phi}\ (V|\psi) = \frac{f_{U\phi}(V,\psi)}{f_\phi(\psi)}. \tag{2.17}$$

For a general turbulent reactive flow a set of $n_s + 1$ composition variable $\mathbf{\Phi} = (\phi_1, \phi_2..., \phi_{n_s+1})$ can be considered. Taking $\mathbf{\Psi} = (\psi_1, \psi_2, ..., \psi_{n_s+1})$ as the sample space of $\mathbf{\Phi}$, the joint PDF of $\mathbf{\Phi}$, $f_{\mathbf{\Phi}}(\mathbf{\Psi})$, is defined to be the probability density of compound event $\mathbf{\Phi} = \mathbf{\Psi}$.

The joint PDF defined at a particular location $\mathbf{x_0}$ and time t_0 can be extended for any location $\mathbf{x}$ and time t which can be denoted by $f_{\mathbf{\Phi}}(\mathbf{\Psi}; \mathbf{x}, t)$. This is referred as one-point, one-time joint PDF, i.e., there is no joint information between $\mathbf{\Phi}$ at two or more positions or times. The PDF method based on $f_{\mathbf{\Phi}}(\mathbf{\Psi}; \mathbf{x}, t)$ is called the compositions joint PDF as discussed in the next section.

2.3.2 Compositions joint PDF

The one-point, one-time compositions joint PDF is defined by

$$f_{\mathbf{\Phi}}(\mathbf{\Psi}; \mathbf{x}, t) \equiv \langle \delta(\mathbf{\Psi} - \mathbf{\Phi}) \rangle. \tag{2.18}$$

On the other hand, the compositions evolve according to

$$\frac{\partial}{\partial t}\left(\rho\phi_\alpha\right) + \frac{\partial}{\partial x_j}\left(\rho\phi_\alpha U_j\right) = -\frac{\partial J_j^\alpha}{\partial x_j} + \rho S_\alpha. \tag{2.19}$$

The transport equation of $f_{\mathbf{\Phi}}$ can be derived from Eqs. (2.18–2.19) following the standard procedure described by Pope [52]. It results in

$$\frac{\partial(\rho(\mathbf{\Psi})f_{\mathbf{\Phi}})}{\partial t}+\frac{\partial(\rho(\mathbf{\Psi})\langle\mathbf{U}_j|\mathbf{\Psi}\rangle f_{\mathbf{\Phi}})}{\partial x_j}+\frac{\partial(\rho(\mathbf{\Psi})S_\alpha(\mathbf{\Psi})f_{\mathbf{\Phi}})}{\partial\psi_\alpha}=\frac{\partial}{\partial\psi_\alpha}\left(\langle\frac{\partial J_j^\alpha}{\partial x_j}|\mathbf{\Psi}\rangle f_{\mathbf{\Phi}}\right). \quad (2.20)$$

It is usual to consider the mass-weighted joint PDF $\tilde{f}_{\mathbf{\Phi}}$ and the compositions mass density function $\mathcal{F}_{\mathbf{\Phi}}$:

$$\mathcal{F}_{\mathbf{\Phi}}=\langle\rho\rangle\tilde{f}_{\mathbf{\Phi}}=\rho(\mathbf{\Psi})f_{\mathbf{\Phi}}. \quad (2.21)$$

The term $(\rho(\mathbf{\Psi})(\mathbf{U}_j|\mathbf{\Psi}\rangle)f_{\mathbf{\Phi}})$ in Eq. 2.20 can be re-expressed as

$$\rho(\mathbf{\Psi})\langle U_j|\mathbf{\Psi}\rangle f_\Phi=(\tilde{U}_j+\langle u_j''|\mathbf{\Psi}\rangle)\langle\rho\rangle\tilde{f}_\Phi, \quad (2.22)$$

where the decomposition $U_j=\tilde{U}_j+u_j''$ has been used. Then the mass density function $\mathcal{F}_{\mathbf{\Phi}}$ evolution equation can be written as

$$\frac{\partial\mathcal{F}_{\mathbf{\Phi}}}{\partial t}+\frac{\partial(\tilde{\mathbf{U}}_j\mathcal{F}_{\mathbf{\Phi}})}{\partial x_j}+\frac{\partial(S_\alpha(\mathbf{\Psi})\mathcal{F}_{\mathbf{\Phi}})}{\partial\psi_\alpha}=-\frac{\partial(\langle u_j''|\mathbf{\Psi}\rangle\mathcal{F}_{\mathbf{\Phi}})}{\partial x_j}+\frac{\partial}{\partial\psi_\alpha}\left(\left\langle\frac{1}{\rho}\frac{\partial J_j^\alpha}{\partial x_j}|\mathbf{\Psi}\right\rangle\mathcal{F}_{\mathbf{\Phi}}\right). \quad (2.23)$$

The terms on the left-hand side of Eq. (2.23) are in closed form provided that the mean velocity is known. The first and second terms represent the evolution in time and advection in physical space due to Favre-averaged mean velocity, respectively. The third term denotes the transport in the composition space by chemical reactions. Closed form of this term in the equation is the main advantage of the PDF methods over the other statistical approaches. But the terms on the right-hand side are in unclosed form. The first term is the turbulent scalar flux representing the transport by Favre fluctuating velocity and the final term is the transport in composition space

due to molecular diffusion. Mixing or micro-mixing models are generally employed to close the last term in Eq. (2.23).

The compositions joint PDF equation is not a self-contained model. Favre averaged mean momentum equations must be solved for the velocity $\tilde{\mathbf{U}}$, and a turbulence model (e.g., $k-\epsilon$) is needed to calculate turbulent diffusivity ($\Gamma \sim k^2/\epsilon$) and scalar mixing rate ($\sim \epsilon/k$) used in the stochastic mixing models.

2.3.3 The velocity-compositions joint PDF

Two weaknesses of compositions JPDF approach are that turbulent transport term must be modeled, and the velocity and turbulence fields have to be treated separately. The velocity-compositions joint PDF approach surmounts these weaknesses.

The one-point, one-time, mass-weighted JPDF of velocity $\mathbf{U}$ and compositions $\mathbf{\Phi}$ at a given location and time is defined as

$$\tilde{f}'(\mathbf{V}, \mathbf{\Psi}\ ; \mathbf{x}, t) \equiv \rho(\mathbf{\Psi}) \langle \delta(\mathbf{V}-\mathbf{U}) \delta(\mathbf{\Psi}-\mathbf{\Phi}) \rangle / \langle \rho \rangle, \tag{2.24}$$

where $\mathbf{V}$ and $\mathbf{\Psi}$ are the sample space variables for the velocity $\mathbf{U}$ and the compositions $\mathbf{\Phi}$, respectively. The delta function represents a multidimensional delta function, for instance $\delta(\mathbf{V}-\mathbf{U})$ represents the 3D delta function at $\mathbf{V}=\mathbf{U}$. The evolution equation for $\tilde{f}'$ can be derived from the Navier-Stokes and species conservation equations using the method discussed by Pope [52]. The resulting evolution equation is

$$\begin{aligned} &\frac{\partial \langle \rho \rangle \tilde{f}'}{\partial t} + V_j \frac{\partial \langle \rho \rangle \tilde{f}'}{\partial x_j} - \frac{\partial \langle p \rangle}{\partial x_j} \frac{\partial \tilde{f}'}{\partial V_j} + \frac{\partial}{\partial \psi_\alpha} (\langle \rho \rangle S_\alpha \tilde{f}') = \\ &\frac{\partial}{\partial V_j} \left(\left\langle -\frac{\partial \tau_{ij}}{\partial x_i} + \frac{\partial p'}{\partial x_j} | \mathbf{V}, \mathbf{\Psi} \right\rangle \tilde{f}' \right) + \frac{\partial}{\partial \psi_\alpha} \left(\left\langle \frac{\partial J_i^\alpha}{\partial x_i} | \mathbf{V}, \mathbf{\Psi} \right\rangle \tilde{f}' \right). \end{aligned} \tag{2.25}$$

The terms on the left-hand side of Eq. (2.25) are in closed form and represent convection, acceleration due to the mean pressure gradient and reaction, respectively.

But the terms on the right-hand side are unclosed, representing the effects of viscous stresses, fluctuating pressure gradient and molecular mixing.

It can be seen that the velocity-compositions joint PDF method retains the advantages of treating reaction without approximation, and in addition, treats turbulent convection exactly thus avoiding gradient diffusion assumptions. It also introduces a more complete closure in which the mean velocity, the Reynolds stresses, and indeed all one point velocity-compositions statistics can be calculated from $\tilde{f}'$.

The model equation for $\tilde{f}'$ is not quite self-contained since the one-point, one-time JPDF of velocity and compositions itself does not contain information on the time scale of turbulence. Thus the turbulence frequency is introduced to provide a time scale into the modeled JPDF equation which is described in the following section.

2.3.4 The velocity, turbulent frequency and compositions joint PDF model

Turbulence modeling requires information on the length or time scale of the turbulence, which is not provided by the one-point one-time joint PDF of velocity and compositions. In the PDF methods, the joint velocity-frequency-compositions PDF model is introduced for this purpose [67]. For a turbulent reactive flow, the mass-weighted JPDF of velocity $\mathbf{U}$, compositions $\mathbf{\Phi}$, and turbulence frequency ω is defined as

$$\tilde{f}\ (\mathbf{V}, \mathbf{\Psi}, \theta; \mathbf{x}, t) \equiv \rho(\mathbf{\Psi})\langle\delta(\mathbf{V}-\mathbf{U})\delta(\mathbf{\Psi}-\mathbf{\Phi})\delta(\theta-\omega)\rangle/\langle\rho\rangle, \tag{2.26}$$

where θ is the sample space variable of ω. The evolution equation of $\tilde{f}$ can be derived from its definition in Eq. (2.26) and the Navier-Stokes and the compositions transport equations [52]. The unclosed terms in the resulting equation are then closed by constructing model stochastic differential equations (SDEs). Models are

required only for the pressure-strain-rate correlation, mixing and dissipation. Models for velocity, turbulence frequency and molecular mixing are described in the following section.

2.4 Model Equations

Joint PDF model for velocity-turbulent frequency-compositions offers a complete closure for turbulent reacting flows [48]. The Lagrangian framework is adopted for this model. In the Lagrangian view point the flow is represented by a large set of notional particles whose properties evolve by a set of stochastic differential equations in such a way that the particles exhibit the same JPDF as the one obtained from the solution of the modeled JPDF transport equation. The models for particle velocity, turbulent frequency, scalar mixing and reaction are discussed here.

2.4.1 Velocity model

Various Langevin models have been developed for the evolution of the particle velocity to account for the acceleration due to mean pressure gradient and to provide a closure for the effects of viscous dissipation and fluctuating pressure gradient [17, 50]. In this study, the emphasis is placed on numerical algorithm so we employ the simplest velocity model, namely the simplified Langevin model (SLM), given by

$$dU_i(t) = -\frac{1}{\langle\rho\rangle}\frac{\partial\langle p\rangle}{\partial x_i}dt - \left(\frac{1}{2}+\frac{3}{4}C_0\right)\Omega\left(U_i(t)-\tilde{U}_i\right)dt + \left(C_0\tilde{k}\Omega\right)^{1/2}dW_i, \quad (2.27)$$

where $\tilde{k}$ is the Favre mean turbulent kinetic energy and $\Omega \equiv C_\Omega \frac{\langle\rho\omega|\omega\geq\tilde{\omega}\rangle}{\langle\rho\rangle}$ is the conditional mean turbulent frequency with ω being the turbulent frequency to be defined in the next section. In Eq. (2.27), $\mathbf{W}(t)$ represents an isotropic vector-valued Wiener process. The standard model constants C_0 and C_Ω are introduced in [50] and [67],

respectively and also specified in Table 2.1. Note that SLM model is equivalent to the Rotta's model [55] at the second moment closure level as discussed by Pope [50].

2.4.2 Turbulent frequency model

Turbulent frequency ω is a particle property that provides the time scale needed to close the velocity and mixing models, and evolves by its own model stochastic differential equation. Here we use the modified Jayesh-Pope model [67] given by

$$d\omega(t) = -C_3\left(\omega - \tilde{\omega}\right)\Omega dt - S_\omega \Omega\omega(t)dt + \left(2C_3C_4\tilde{\omega}\Omega\omega\left(t\right)\right)^{1/2} dW, \tag{2.28}$$

where the source term S_ω is defined as $S_\omega = C_{\omega 2} - C_{\omega 1}\mathcal{P}/(\tilde{k}\Omega)$. Here $\mathcal{P} = -\widetilde{u_i u_j}\frac{\partial \tilde{U}_i}{\partial x_j}$ is the turbulence production and W is an independent Wiener process. The standard model constants are introduced in [67] and also given in Table 2.1.

2.4.3 Mixing model

Mixing models are needed to close the molecular diffusion term, i.e., the last term in Eq. (2.25). There are various mixing models employed in the PDF methods [35, 60]. Most scalar mixing models assume that the molecular mixing is independent of velocity, i.e., $\langle \frac{\partial J_i^\alpha}{\partial x_i} | \mathbf{V}, \mathbf{\Psi} \rangle \tilde{f}' = \langle \frac{\partial J_i^\alpha}{\partial x_i} | \mathbf{\Psi} \rangle \tilde{f}'$. Although some recent works [36, 56, 57] indicate that this simplification can give rise to significant error, the simple interaction by exchange with the mean (IEM) mixing model is used here since the main purpose of the present study is to evaluate the performance of the new hybrid solution algorithm. Note that a more consistent mixing model has been recently proposed by Pope [45] but its performance has yet to be tested. In the IEM model [9], particle composition relaxes toward the local mean composition at the rate $1/2C_\phi\Omega$

$$\frac{d\mathbf{\Phi}}{dt} = -\frac{1}{2}C_\phi\Omega(\mathbf{\Phi}(t) - \tilde{\mathbf{\Phi}}(t)) + S(\mathbf{\Phi}). \tag{2.29}$$

In this equation the last term is the rate of change due to chemical reaction, which appears to be in closed form in JPDF model. The constant C_ϕ is the standard model constant specified in Table 2.1.

Table 2.1: Standard model constants*

C_0	$C_{\omega 1}$	$C_{\omega 2}$	C_3	C_4	C_Ω	C_ϕ
2.1	0.5625	0.9	1.0	0.25	0.6893	2.0

* In the simulations the standard values [67] for model constants are used except for $C_{\omega 1}$ which is taken as $C_{\omega 1} = 0.65$ in the present study following Muradoglu et al. [37].

2.4.4 Chemistry model

To reduce computational cost and facilitate extensive simulations but without loss of generality, a simple flamelet model is used for the treatment of chemical reactions. In this approach, the thermo-chemical state is solely determined by a single variable, the mixture fraction ξ. The flamelet library is formed based on the laminar flame calculations at a stretch rate using the GRI 2.1 detailed chemistry model [73]. The definition of the mixture fraction ξ follows the method of Bilger et al. [4]

$$\xi = \frac{\frac{2(Z_C - Z_{C,\mathcal{O}})}{W_C} + \frac{Z_H - Z_{H,\mathcal{O}}}{2W_H} + \frac{Z_O - Z_{O,\mathcal{O}}}{W_O}}{\frac{2(Z_{C,\mathcal{F}} - Z_{C,\mathcal{O}})}{W_C} + \frac{Z_{H,\mathcal{F}} - Z_{H,\mathcal{O}}}{2W_H} + \frac{Z_{O,\mathcal{F}} - Z_{O,\mathcal{O}}}{W_O}}, \tag{2.30}$$

where Z_i is the total mass fraction of element i, W_i is the atomic mass of element i, second subscripts $\mathcal{O}$ and $\mathcal{F}$ denotes the oxidant and fuel streams. In the experimental data sets used in this thesis the mixture fraction is also calculated by the above formula. By flamelet model assumption the IEM mixing model given in Eq. (2.29) simplifies as

$$\frac{d\xi}{dt} = -\frac{1}{2} C_\phi \Omega (\xi - \tilde{\xi}). \tag{2.31}$$

After introducing stochastic models, the transport equation for $\tilde{f}\ (\mathbf{V}, \mathbf{\Psi}\ , \theta; \mathbf{x}, t)$ can be derived from Eqs. (2.27–2.29) by using the same procedure as described in [52]

and is given by

$$\frac{1}{\langle\rho\rangle}\frac{\partial}{\partial t}(\langle\rho\rangle\tilde{f}) = -\frac{1}{\langle\rho\rangle}V_i\frac{\partial}{\partial x_i}(\langle\rho\rangle\tilde{f}) + \frac{\partial\langle p\rangle}{\partial x_i}\frac{\partial\tilde{f}}{\partial V_i}$$
$$+\left(\frac{1}{2}+\frac{3}{4}C_0\right)\Omega\frac{\partial}{\partial V_i}\left[\tilde{f}(V_i-\tilde{U}_i)\right] + \frac{1}{2}C_0\tilde{k}\Omega\frac{\partial^2\tilde{f}}{\partial V_i\partial V_i}$$
$$+\Omega\frac{\partial}{\partial\theta}(\tilde{f}\theta S_\omega) + C_3\Omega\frac{\partial}{\partial\theta}\left[\tilde{f}(\theta-\tilde{\omega})\right] + C_3C_4\Omega\tilde{\omega}\frac{\partial^2}{\partial\theta^2}(\tilde{f}\theta)$$
$$-\frac{\partial}{\partial\psi_\alpha}(\tilde{f}S_\alpha) + \frac{1}{2}C_\phi\Omega\frac{\partial}{\partial\psi_\alpha}\left[\tilde{f}(\psi_\alpha-\phi_\alpha)\right]. \tag{2.32}$$

As can be seen the transport equation for $\tilde{f}$ evolves in a high dimensional space, i.e., one time, three physical, one turbulent frequency, and (n_s+1) compositions space. Conventional numerical techniques such as finite difference and finite volume methods can not deal with such a problem since the computational cost increases exponentially with the number of dimensions in these techniques. This difficulty is overcome using the Monte Carlo method in which the computational cost increases only linearly with the number of sample-space dimensions [52].

2.5 The New Hybrid Algorithm

The consistent hybrid finite-volume/particle method is the favorable solution algorithm for JPDF model equations of turbulent reactive flows. In this approach, the mean velocity and pressure are computed by the finite volume method and supplied to the particle algorithm which in turn solves the model equations for the fluctuating velocity, turbulent frequency and compositions, and provides the mean density and Reynolds stresses to the FV code. This coupling substantially reduces the noise in the mean fields used in the particle equations and thus virtually eliminates the bias error [40]. In the original consistent hybrid method proposed by Muradoglu et al. [40, 39], a density-based finite-volume solver is used to solve the mean mass, momentum and energy conservation equations while a particle-based Monte-Carlo

algorithm is employed to solve the stochastic equations for the fluctuating velocity, turbulent frequency and compositions. Full consistency of the method was enforced by the correction algorithms [39]. The preconditioning method developed by Muradoglu and Caughey [41] was employed in the FV solver used in the old hybrid method. In addition to the well known lack of robustness in the vicinity of stagnation points, it has been found that the solution is highly sensitive to the preconditioning parameters and may be contaminated by the excessive numerical dissipation unless the preconditioning parameters are carefully tuned for each flow [21]. In particular, the previous versions of the hybrid algorithm failed to achieve a grid convergence for the non-reacting bluff-body flow [21]. When the grid is refined beyond a threshold, the old hybrid algorithm resulted in a vortex shedding that has not been observed experimentally [7].

The present hybrid method is designed to remedy the deficiencies of the old hybrid algorithm and thus create a robust PDF solution algorithm for a wide range of flow conditions without any adjustable free parameter. In this approach, a pressure-based FV solver is employed to solve the Favre-averaged variable density incompressible flow equations while a particle-based Monte Carlo algorithm is used to solve the evolution equations for the fluctuating velocity, turbulent frequency and compositions. For this purpose, the constant-density PISO-FV solver that is available in OpenFOAM package [74] has been first modified for a variable density flow and then combined with the particle code. The mean density field is obtained from the particles as a particle field and passed to the FV solver. Note that this is in contrast with the old hybrid method in which the mean energy equation is solved by the FV solver and the mean density is subsequently obtained from the mean equation of state. As a result, the redundant FV density field and associated energy correction used in the old hybrid method are eliminated in the present approach. In the next sections the

equations solved by the FV and particle algorithms are first described and then the coupling is discussed.

2.5.1 FV system

The open source FV package OpenFOAM is employed to solve the mean mass and momentum equations using a pressure based PISO algorithm. The conservation equations are directly derived from the modeled JPDF evolution equation (Eq. (2.32)) and can be written as

$$\frac{\partial \langle\rho\rangle}{\partial t} + \frac{\partial(\langle\rho\rangle \tilde{U}_i)}{\partial x_i} = 0, \tag{2.33}$$

$$\frac{\partial}{\partial t}\left(\langle\rho\rangle\tilde{U}_i\right) + \frac{\partial(\langle\rho\rangle\tilde{U}_i\tilde{U}_j)}{\partial x_j} = -\frac{\partial\langle p\rangle}{\partial x_i} - \frac{\partial\left(\langle\rho\rangle\widetilde{u_i u_j}\right)}{\partial x_j}. \tag{2.34}$$

Assuming that the flow is statistically stationary, the time derivative in the mass conservation equation can ben neglected and the continuity equation becomes

$$\frac{\partial}{\partial x_i}(\langle\rho\rangle \tilde{U}_i) = 0. \tag{2.35}$$

Here $\mathbf{u} = \mathbf{U} - \tilde{\mathbf{U}}$ is the Favre fluctuating velocity. The mean mass and momentum equations are closed since the mean density $\langle\rho\rangle$ and the Reynolds stresses $\langle\rho\rangle\widetilde{u_i u_j}$ are evaluated as particle mean fields and passed to the FV code in each outer iteration. These particle quantities are time-averaged using the same procedure as Muradoglu et al. [39] to reduce the statistical error. Note that the FV solver is found to be very robust even when the mean density and Reynolds stresses are not time-averaged and thus contain significant statistical fluctuations. This is of crucial importance especially for unsteady RANS/PDF and LES/PDF simulations.

2.5.2 Particle system

In the context of the hybrid method, the particle algorithm is used to solve the evolution equations for the fluctuating velocity, turbulence frequency and compositions. In a Largrangian point of view, the flow is represented by a set of particles which evolve by the model stochastic differential equations. These equations represent particle properties in a way that the particles exhibit the same JPDF as the solution of the modeled JPDF transport equation. Each particle has a set of properties $(m^*, \mathbf{X}^*, \mathbf{U}^*, \mathbf{\Phi}^*, \omega^*)$ where m^* represents the mass of the particle, $\mathbf{X}^*$ its coordinates, $\mathbf{U}^*$ the velocity, $\mathbf{\Phi}^*$ the compositions vector, and ω^* the turbulence frequency. Note that the superscript $(*)$ denotes that the quantity is a particle property. In the hybrid method the mean velocity field is taken from the FV solver. Therefore, the mean velocity evolution equation is subtracted from the velocity model to obtain the evolution equation for the fluctuating part. The SLM model for the fluctuating part of the velocity is then given by

$$du_i^* = \left[\frac{1}{\langle\rho\rangle}\frac{\partial\left(\langle\rho\rangle\widetilde{u_i u_j}\right)}{\partial x_j}\right]^* dt - u_j^*\frac{\partial\tilde{U}_i^*}{\partial x_j}dt - \left(\frac{1}{2}+\frac{3}{4}C_0\right)\Omega^* u_i^*(t)dt + \left(C_0\tilde{k}^*\Omega^*\right)^{1/2} d\mathcal{W}_i. \tag{2.36}$$

The particles move with the local flow velocity according to

$$d\mathbf{X}^* = \left(\tilde{\mathbf{U}}^* + \mathbf{u}^*\right)dt, \tag{2.37}$$

where $\tilde{\mathbf{U}}^*$ is the Favre-averaged mean velocity interpolated from the FV field on the particle locations while $\mathbf{u}^*$ is obtained from solution of Eq. (2.36). Note that the interpolation scheme developed by Jenny et al. [20] is used to evaluate $\tilde{\mathbf{U}}^*$ in Eq. (2.37). The particle algorithm also solves the evolution equations for the turbulent frequency (Eq. (2.28)) and compositions (Eq. (2.31)).

The model equations have been presented in the Cartesian coordinates so far. However cylindrical coordinates are more convenient for statistically axi-symmetric flow simulations. For this purpose, the model equations are transformed into the cylindrical coordinates in Appendix B.

2.5.3 Correction algorithms

Although the present hybrid method is fully consistent at the level of governing equations, inconsistencies may occur due to accumulation of numerical error. Velocity and position correction algorithms developed by Jenny et al. [20] and Muradoglu et al. [39] are employed to achieve a full consistency at the numerical solution level.

The first consistency condition that needs to be satisfied states that the Favre mean of the fluctuating velocity must remain zero, i.e.,

$$\tilde{\mathbf{u}}^* = 0. \tag{2.38}$$

This condition is not automatically satisfied due to accumulation of numerical error, so it is enforced using the simple velocity correction algorithm proposed by Jenny et al. [20]. In this method, before the correction, the mean fluctuating velocity is extracted from the particles by using the kernel estimation technique [15, 11] and denoted by $\mathbf{u}^*_{bc}$. Then it is time averaged and interpolated on to the particles denoted by $\tilde{\mathbf{u}}^*_{bc,TA}$. Then the correction is performed by subtracting $\tilde{\mathbf{u}}^*_{bc,TA}$ from the particle fluctuating velocity $\mathbf{u}^*_{bc}$. The algorithm is summarized as

$$\mathbf{u}^* = \mathbf{u}^*_{bc} - \tilde{\mathbf{u}}^*_{bc,TA}. \tag{2.39}$$

The second consistency condition is that the time averaged particle mass density, q_{TA}, matches the mean fluid density $\langle\rho\rangle_{TA}$, i.e.,

$$q_{TA} = \langle\rho\rangle_{TA}. \tag{2.40}$$

The mean fluid density is obtained from chemical compositions of particles and the particle mass density for the cell α is defined as

$$q_\alpha \equiv \frac{M_\alpha^P}{V_\alpha^P}, \tag{2.41}$$

where M_α^P and V_α^P denote the total mass of particles in the cell and the cell volume, respectively. The basic principle of position correction scheme proposed by Muradoglu et al. [39] is to compute a correction velocity $\mathbf{U}_c^*$ to be added to the particle instantaneous velocity such that the time averaged particle mass density matches the fluid density in each grid cell.

In the old hybrid algorithm the mean energy conservation equation was also solved by the FV method and mean density was subsequently computed from the mean equation of state. So another consistency condition was needed to match the particle and FV sensible internal energies. In the present hybrid algorithm there is no need for solving mean energy equation so it makes the method more consistent at the numerical solution level and eliminates the need for the energy correction algorithm.

2.5.4 Local particle time stepping

Local time stepping is an effective way of accelerating convergence to a statistically stationary state when a highly stretched non-uniform grid is used. Its purpose is to use a local CFL criterion to determine the particle time step, while still solving for the same steady-state modeled joint PDF equation of turbulent reactive flows.

Assume that the local particle time increment dt is related to the global time increment ds through

$$dt = \gamma(\mathbf{x}, s)ds, \tag{2.42}$$

where $\gamma(\mathbf{x}, s)$ is a strictly positive, non-dimensional field. The particle evolution equations for mass m, numerical weight μ, and position $\mathbf{X}$ are

$$\frac{dm}{ds} = 0, \tag{2.43}$$

$$\frac{d\mu}{ds} = \gamma\beta\mu, \tag{2.44}$$

$$\frac{d\mathbf{X}}{ds} = \gamma\mathbf{U}, \tag{2.45}$$

$$d\mathbf{U} = \gamma\mathbf{A}ds + \sqrt{2\gamma B}dW, \tag{2.46}$$

where the field $\beta(\mathbf{U}, \mathbf{x}, s)$ is to be determined. Note that for $\gamma = 1$ and $\beta = 0$ these equations revert to their constant-time counterparts. For this system, the mass density function is defined as

$$\hat{\mathcal{F}}(\mathbf{V}, \mathbf{x}, s) = \langle \mu m \delta(\mathbf{U} - V)\delta(\mathbf{X} - x)\rangle. \tag{2.47}$$

When standard techniques [52] are used, the evolution equation for $\hat{\mathcal{F}}$ can be derived to yield

$$\frac{1}{\gamma}\frac{\partial\hat{\mathcal{F}}}{\partial s} - \hat{\mathcal{F}}\left\{\beta - \frac{V_i}{\gamma}\frac{\partial\gamma}{\partial x_i}\right\} = -\frac{\partial}{\partial V_i}[\hat{\mathcal{F}}A_i] - V_i\frac{\partial\hat{\mathcal{F}}}{\partial x_i} + \frac{\partial^2}{\partial V_i\partial V_i}[\hat{\mathcal{F}}B]. \tag{2.48}$$

It can be observed that the right-hand side of this equation is identical to that of the corresponding constant time-step equation. Hence, if β can be specified so that the left-hand side of Eq. (2.48) vanishes in the steady state solutions, then Eq. (2.48) yields

the same steady state solutions as its constant time-step counterpart. Muradoglu and Pope [38] choose $\gamma(\mathbf{x}, t)$ to be a function of a local CFL criterion. Assuming a Gaussian velocity distribution, the maximum particle velocity is estimated in a statistically two-dimensional flow as

$$U_{max,i} = |\tilde{U}_i| + 2u_i, \qquad i = 1, 2 \tag{2.49}$$

where $\tilde{U}_i$ and u_i are the mean and rms velocities. The local time step is specified by

$$\Delta t_{i,j} = \min[\Delta_{lim}, \Delta t_{x_{i,j}}, \Delta t_{y_{i,j}}, \Delta t_{\Omega}]. \tag{2.50}$$

The parameter Δt_{lim} sets an upper limit to local time step and it is typically taken as $\Delta t_{lim} = \kappa_t \Delta t_{min}$, where Δt_{min} is the minimum value of $\Delta t_{x_{i,j}} = \left(\frac{C_U U_{max,1}}{\Delta x}\right)_{i,j}^{-1}$, $\Delta t_{y_{i,j}} = \left(\frac{C_U U_{max,2}}{\Delta y}\right)_{i,j}^{-1}$, and $\Delta t_{\Omega_{i,j}} = \left(\frac{C_\Omega}{\Omega}\right)_{i,j}$ over the entire computational domain. The parameters C_U, C_Ω, and κ are taken as 0.4, 0.2, and 20, respectively.

After calculating the time steps at all grid points as described, the time step is represented as a linear spline and interpolated onto particles. The local time step is stored as a particle property and the numerical weight μ is updated as

$$\mu^{n+1} = \mu^n (\Delta t^{n+1} / \Delta t^n). \tag{2.51}$$

In the present study, the local time stepping method developed by Muradoglu and Pope [38] and briefly derived above has been employed to accelerate the convergence rate of the new hybrid algorithm.

2.5.5 Coupling with the ISAT

The use of detailed chemical kinetic models in real combustor simulations is crucial for the accurate prediction of performance characteristics such as prediction of emissions,

ignition, lean blow-out, etc. The detailed description of combustion typically involves tens of species, hundreds of reactions, and time scales from 10^{-9} s to 1 s. Thus the computational cost of performing computations for turbulent flames using a detailed chemistry model is usually deemed to be prohibitive mainly due to the stiffness of chemical kinetic equations caused by the large disparity of time scales. A detailed chemistry model consisting of hundreds of reactions and tens of species can be simplified into a reduced chemistry model consisting of a few steps and species. While the reduced mechanisms are computationally efficient, they are usually inadequate for accurate predictions. On the other hand, the high computational cost of integrating the reaction equations prevents the inclusion of detailed chemistry models. The *in situ adaptive tabulation* scheme (ISAT) proposed by Pope [53] has significantly alleviated this problem by facilitating the efficient integration of the reaction equations via a unique combination of direct integration and dynamic creation of a look-up table, thus allowing for the implementation of detailed chemistry schemes in turbulent reacting flow calculations.

Although the simple flamelet chemistry model is employed in the most results presented in this thesis mainly to facilitate extensive numerical simulations needed to quantify the performance of the new hybrid algorithm, the latest version of ISAT package (ISAT-CK7) [46] is incorporated into the hybrid algorithm to allow simulations with detailed chemistry. The further details of coupling and sample detailed chemistry calculations are presented in Chapter 5.

2.5.6 Overall solution procedure

The FV and particle methods are periodically used in the hybrid algorithm to solve their respective equations as shown in Fig. 2.1. Following Muradoglu et al. [40, 39], each period is called an outer iteration which consists of FV and particle inner iterations. The pressure base FV algorithm of OpenFOAM [74] is used to solve the mean

mass and momentum equations (Eqs. (2.34), (2.35)), while a particle/mesh method is used to solve the modeled transport equation of the JPDF for the fluctuating velocity, turbulent frequency, and compositions. The particle and FV codes are linked to close the particle and mean equations as follows. The mean velocity and pressure are provided to particle code by the FV code while the FV code gets the mean density and Reynolds stresses as obtained from the particle code and kept the same during each FV inner iteration. The particle code runs for a few (typically 3) time steps in each particle inner iteration. The particle fields needed to close the equations solved by the FV and particle algorithms are computed using the cloud-in-cell (CIC) method [15] and subsequently time-averaged to reduce the statistical error. Following Muradoglu et al. [39], a particle mean field Q is time-averaged as

$$Q_{TA}^{k} = \left(1 - \frac{1}{N_{TA}}\right) Q_{TA}^{k-1} + \frac{1}{N_{TA}} Q^{k}, \tag{2.52}$$

where Q_{TA}^{k} and Q^{k} are the time-averaged and instantaneous values evaluated at k^{th} particle time step. The parameter N_{TA} is a time-averaging factor that is selected relatively small in the initial stage of simulation and gradually increased to its final value when a statistically stationary solution is approached. The FV fields are not time-averaged. It is emphasized here that the hybrid method is very robust even when the particle fields are not time-averaged and contains significant statistical fluctuations.

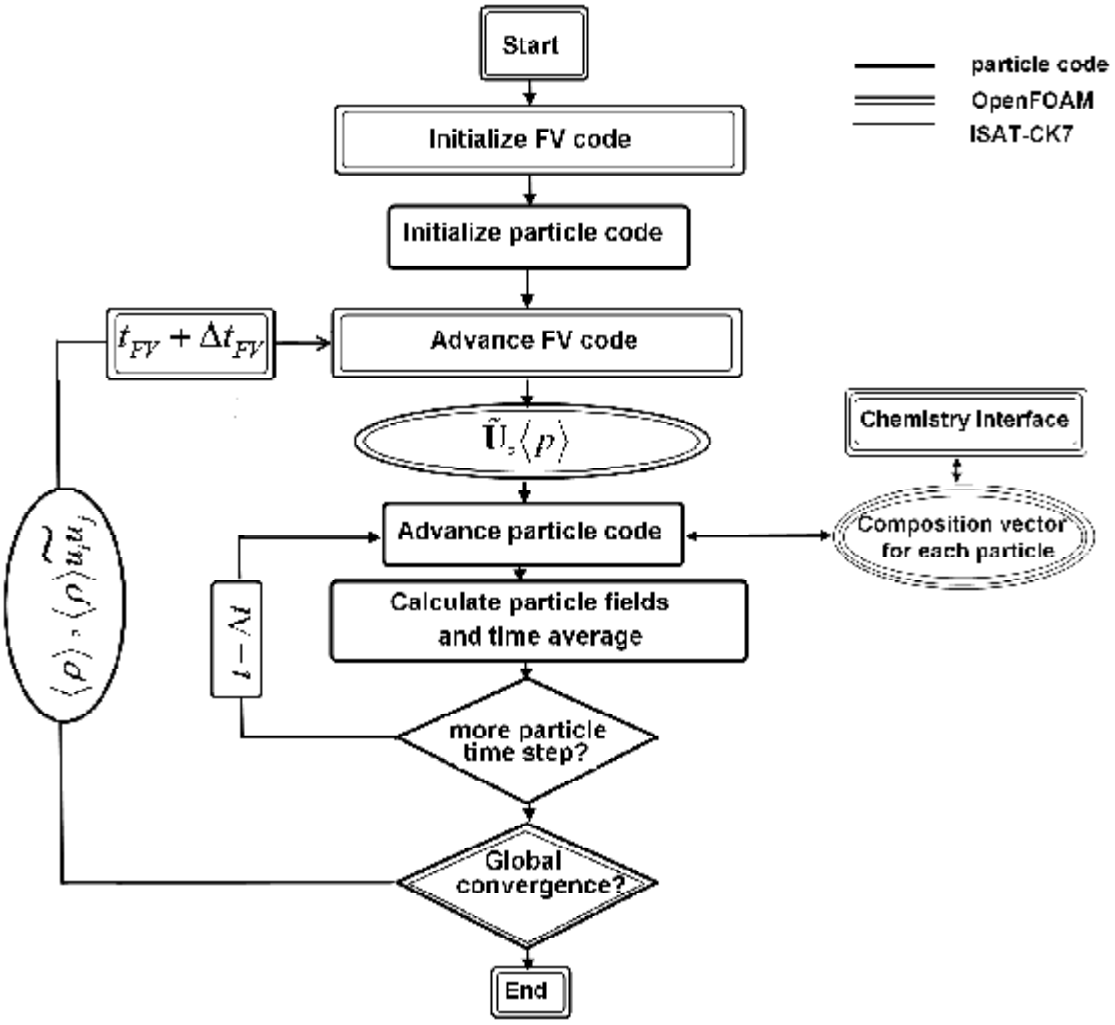


Figure 2.1: Flow chart of the present hybrid method.

Chapter 3

Bluff-Body Flows

3.1 Introduction

In this chapter the new hybrid algorithm is applied to simulate cold and reacting bluff-body flows studied experimentally by Masri et al. [33] and Dally et al. [6, 7]. In the old hybrid method the results for non-reacting bluff-body flow [21] were presented only for grids containing 32×32 and 64×64 cells and the method produced nonphysical vortex shedding when the grid was further refined. Hence the robustness of the algorithm is first demonstrated for non-reacting bluff-body flow. Then the numerical properties of the new method are studied extensively for the buff-body stabilized flame 'HM1E'.

A simple flamelet model is used for the treatment of chemical reactions in order to reduce the computational cost and facilitate extensive simulations. The flamelet library is formed based on the laminar flame calculations at a moderate strain rate of $a = 100$ 1/s using the GRI 2.1 detailed chemistry model [73]. In Chapter 5 the detailed chemistry calculations will be presented for the bluff-body flame.

3.2 Sydney Bluff-Body Burner

The bluff-body flames have been selected among target flames in the turbulent non-premixed flames (TNF) workshops [3] due to their relevance to numerous engineering applications such as bluff-body stabilized combustors widely used in industrial applications because of their enhanced mixing characteristics, improved flame stability and ease of combustion control [6, 7]. Besides their practical significance, the bluff-body flows provide an excellent but challenging test case for the numerical solution algorithms as well as the chemistry and turbulence models due to their simple and well defined initial and boundary conditions, and their ability to maintain the flame stabilization for a wide range of inlet flow conditions with a complex recirculation zone [6, 33]. For the bluff-body flame, extensive measurements of temperature, compositions, and emission of pollutants have been made for a range of flame conditions with various fuel mixtures. The data are collected at different axial and radial locations along the full length of the most flames and are presented in the form of ensemble means, root-mean-square (rms) fluctuations, probability density functions (PDF) and scatter plots. All the experimental data are available from the Internet [75, 3].

Figure 3.1 shows a sketch of the Sydney bluff-body burner with flame propagation length and measurement locations. A full description of the Sydney bluff-body burner and the measurement locations can be found in [6, 33, 75]. In this burner a fuel jet is surrounded by a bluff-body and a co-flowing air stream. The burner is placed in a wind tunnel that has an exit cross section of 230×230 mm^2. The diameter of the bluff-body is $D_b = 50$ mm, and that of the jet is $D_j = 2R_j = 3.6$ mm. There is a recirculation zone immediately after the bluff-body surface which stabilizes the flame. Downstream of the recirculation zone is called the neck zone where strong turbulence-chemistry interactions take place. Thus a simple flamelet model is expected to be less accurate in this region. Experiments were performed for various fuels and flow conditions. In the next sections we will present some simulation results of the cold

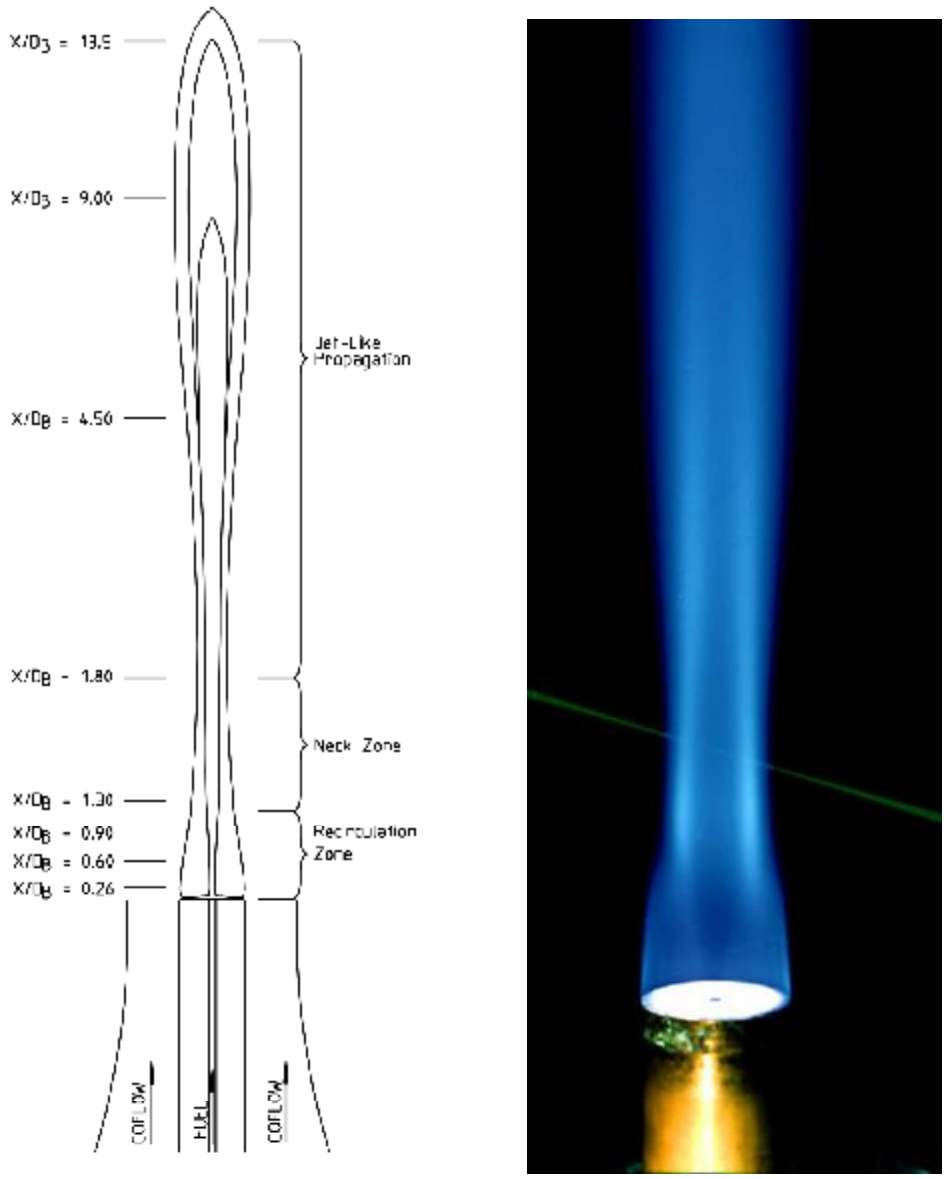


Figure 3.1: Sketch of the Sydney bluff-body burner, flame propagation length and the measurement locations (left), and the photograph of the flame in operation (right) [75].

bluff-body flow and then numerical properties and performance of our new algorithm are demonstrated for the flame 'HM1E'.

3.3 Non-Reacting Bluff-Body Flow

Non-reacting bluff-body flow has been studied experimentally by Dally et al. [7]. Full experimental data sets are available on the website of the University of Sydney [75]. The measurements have been reported three times using two different facilities. The data set1 is from the measurements obtained in 1995 while the data set2 and 3 are newer data measured in 1998 using the improved facility, so set 2 and 3 are expected to be more accurate. In this flow, air is issued from the jet at bulk velocity of 61 m/s into a co-flow of air at 20 m/s. PDF simulations of this flow were carried out using the old hybrid algorithm by Jenny et al. [21]. It is found that the old loosely-coupled hybrid method consistently resulted in unphysical vortex shedding when the grid was refined beyond a threshold, i.e., the grid containing 64×64 cells. It was not clear whether this unphysical behavior was due to the deficiency of models used or due to excessive numerical dissipation in the numerical solutions. Therefore the new hybrid method is used to simulate this flow using the same sub-models, initial and boundary conditions as in Jenny et al. [21].

For the numerical simulations, the flow is assumed to be axisymmetric so a cylindrical coordinate system is adopted with x representing the axial direction aligned with the jet axis and r the radial direction as sketched in Fig. 3.2. The origin of the coordinate system is placed at the center of the jet in the exit plane. The computational domain is $10D_b$ long in the axial direction and extends to $4D_b$ in the radial direction. The Cartesian grid is stretched both in the axial and radial directions. The initial and boundary conditions are specified in the same way as in Jenny et al. [20] for all the quantities. Computations are performed using 64×64, 128×128 and 256×256 grids. To show the statistical stationarity of the numerical solutions, time series of mean axial velocity and turbulent kinetic energy are monitored at six probe locations as specified in Table 3.1. Figure 3.3 depicts the time histories of mean axial velocity and turbulent kinetic energy at these probe points. The present hybrid algorithm

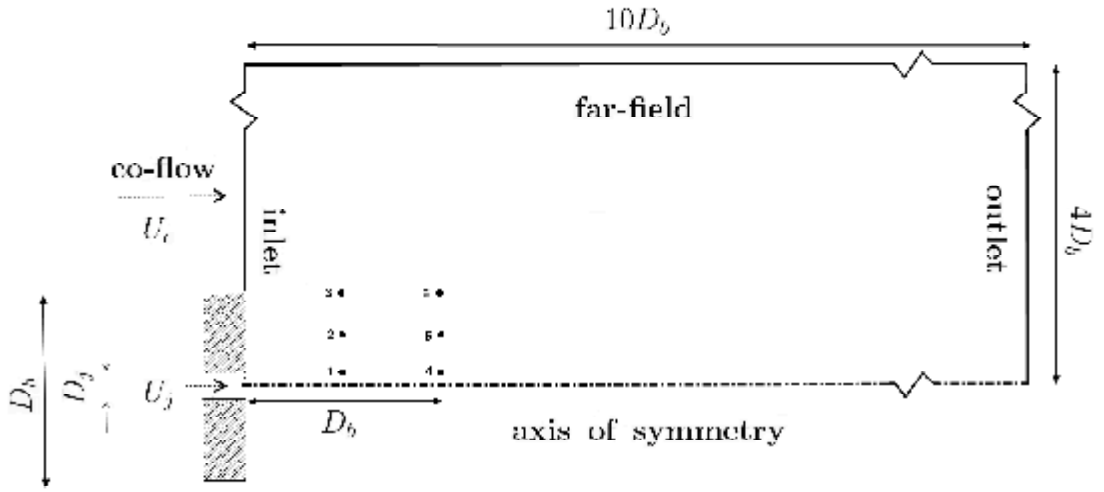


Figure 3.2: Computational domain of the non-swirling bluff-body flow with boundary conditions. Location of probe points are shown with respect to the bluff-body base. See also Table 3.1 for specifications. The same computational domain is also used for the non-swirling reacting bluff-body flow.

reaches a statistically stationary solution successfully after about 10000 time steps without any sign of vortex shedding even for the 256×256 grid. Figure 3.4 shows the mean streamlines in the vicinity of the recirculation zone (RZ) computed using the 256×256 grid. This demonstrates that the unphysical vortex shedding observed in the old loosely-coupled hybrid algorithm was mainly caused by the excessive numerical dissipation in its density-based FV solver. The flow field depicted in Fig. 3.4 is qualitatively in good agreement with the experimental observations [7]: There are two vortices, i.e., an outer vortex located close to the co-flowing air with the center at about $(x/D_b, r/R_b) \approx (0.7, 0.25)$ and an inner vortex located between the outer vortex and the central jet with the center at $(x/D_b, r/R_b) \approx (0.6, 0.75)$. The length of the recirculation region is predicted as $\ell_r/D_b \approx 1.1$ which compares reasonably well

Table 3.1: The coordinates of probe points used to monitor statistical statinarity.

Points	1	2	3	4	5	6
x	$1/2D_b$	$1/2D_b$	$1/2D_b$	D_b	D_b	D_b
r	R_j	$D_b/4$	$D_b/2$	R_j	$D_b/4$	$D_b/2$

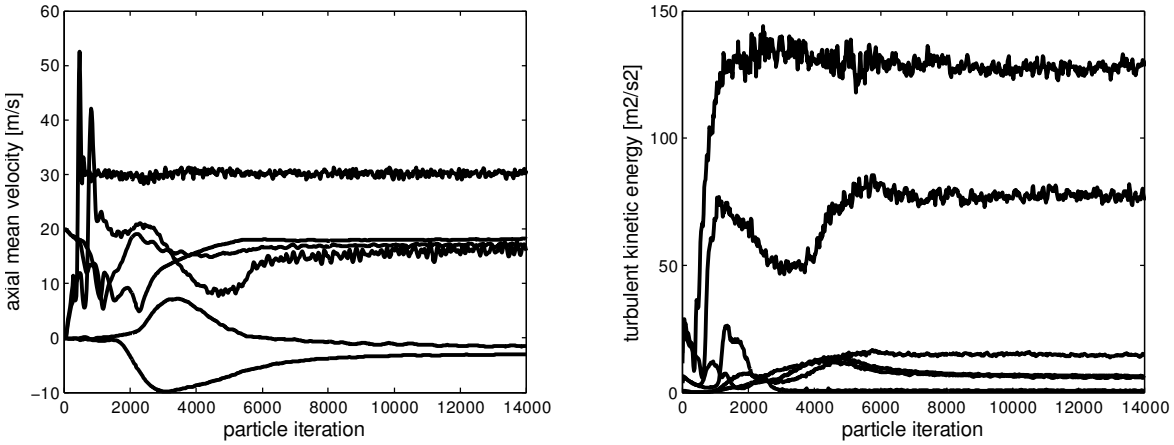


Figure 3.3: The cold bluff-body flow. Time series of Favre-averaged mean axial velocity and turbulent kinetic energy at the six probe points.

with the experimental value of $\ell_r/D_b \approx 1$ [7]. The radial profiles of the mean and rms velocities in the axial and radial directions computed using three different grids are plotted in Fig. 3.5 at axial location $x/D_b = 1.0$ and compared with the experimental data as well as with the PDF simulations performed using the old loosely-coupled hybrid method [21]. As seen in this figure, the grid convergence is achieved for the 128×128 grid. The full grid convergence results are given in Appendix A. This demonstrates that the unphysical vortex shedding observed in the old hybrid algorithm was mainly caused by the excessive numerical dissipation in its density-based FV solver.

Figures 3.6–3.9 compare the profiles of the mean and rms axial and radial velocities with the experimental data and also with the results obtained using the old hybrid solution algorithm [21]. As can be seen in Fig. 3.6 the present hybrid algorithm predicts the mean axial velocity better than the old hybrid algorithm especially inside the recirculation region. In the further downstream of the recirculation region, i.e., at axial locations x/D_b =1.2, 1.3 and 1.8, the axial mean velocity is underpredicted especially near the centerline. The computed mean axial velocities at axial locations x/D_b =2.4, 3.4, and 4.4 are in good agreement with the experimental data. Figure 3.7

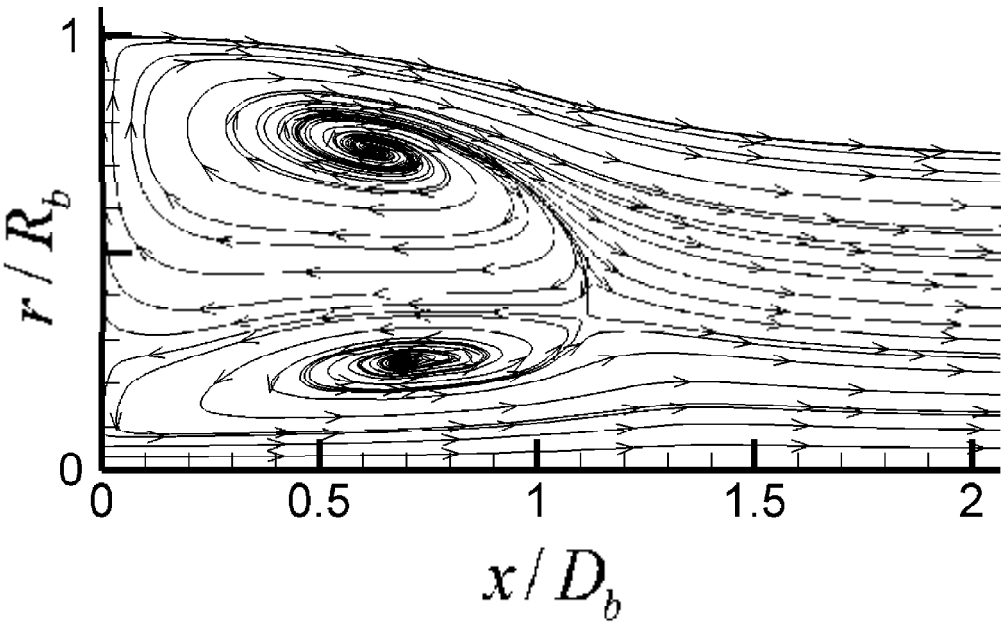


Figure 3.4: The cold bluff-body flow. The streamlines of the mean velocity in the recirculation zone of the non-reacting bluff-body flow calculated using 256×256 grid.

shows the profiles of the mean radial velocities at different axial locations. In spite of the small magnitude of radial velocities with respect to axial velocities the computed results are in reasonable agreement with the experimental data. The profiles of the rms axial and radial velocities are shown in Figs. 3.8–3.9. The computed results are in good agreement with the newer experimental data, i.e., set2 and set3, except in the axial location $x/D_b = 1.3$ where there is no newer experimental data. It is found that the present computed rms axial and radial velocities are in better agreement with the results obtained by the old hybrid algorithm [21]. Figure 3.10 compares the conditional mean frequency computed using the present and the old hybrid algorithms in the axial locations $x/D_b = 0.4$ and 1.0. It can be said that this quantity is underpredicted by the old algorithm. To sum up, it is found that the present results are overall in better agreement with the experimental data than the results obtained using the old hybrid solution algorithm.

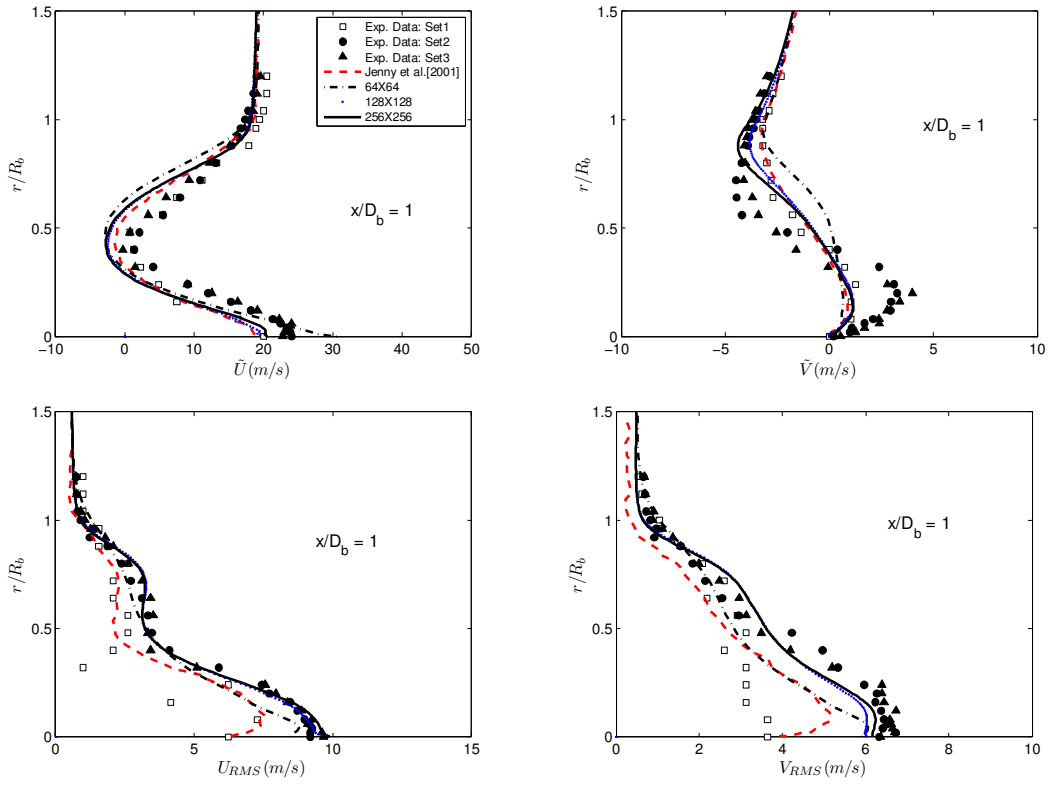


Figure 3.5: The cold bluff-body flow. Radial profiles of the mean and rms axial and radial velocities at the axial location $x/D_b = 1.0$ (for non-reacting bluff-body flow). Present results for three different grids, i.e., 64×64, 128×128, and 256×256, are compared with the experimental measurements and previous PDF simulations performed using the old hybrid algorithm.

3.4 Bluff-Body Stabilized Flame 'HM1E'

The numerical properties and performance of the present hybrid method are examined using the bluff-body stabilized flame studied experimentally by Dally et al. [6, 7] and computationally using the old consistent hybrid algorithm by Muradoglu et al. [37] and Liu et al. [25]. Here we consider the 'HM1E' flame whose details are specified in Table 3.2. In this table, U_c is the velocity of co-flowing air, U_j is the velocity of fuel jet and T_{in} is the temperature of fuel at jet exit plane and ξ_{st} is the stoichiometric mixture fraction. For the numerical simulations, the flame is assumed to be axisymmetric so a cylindrical coordinate system is adopted with x representing the axial direction aligned with the jet axis and r the radial direction as sketched in Fig. 3.2. The origin

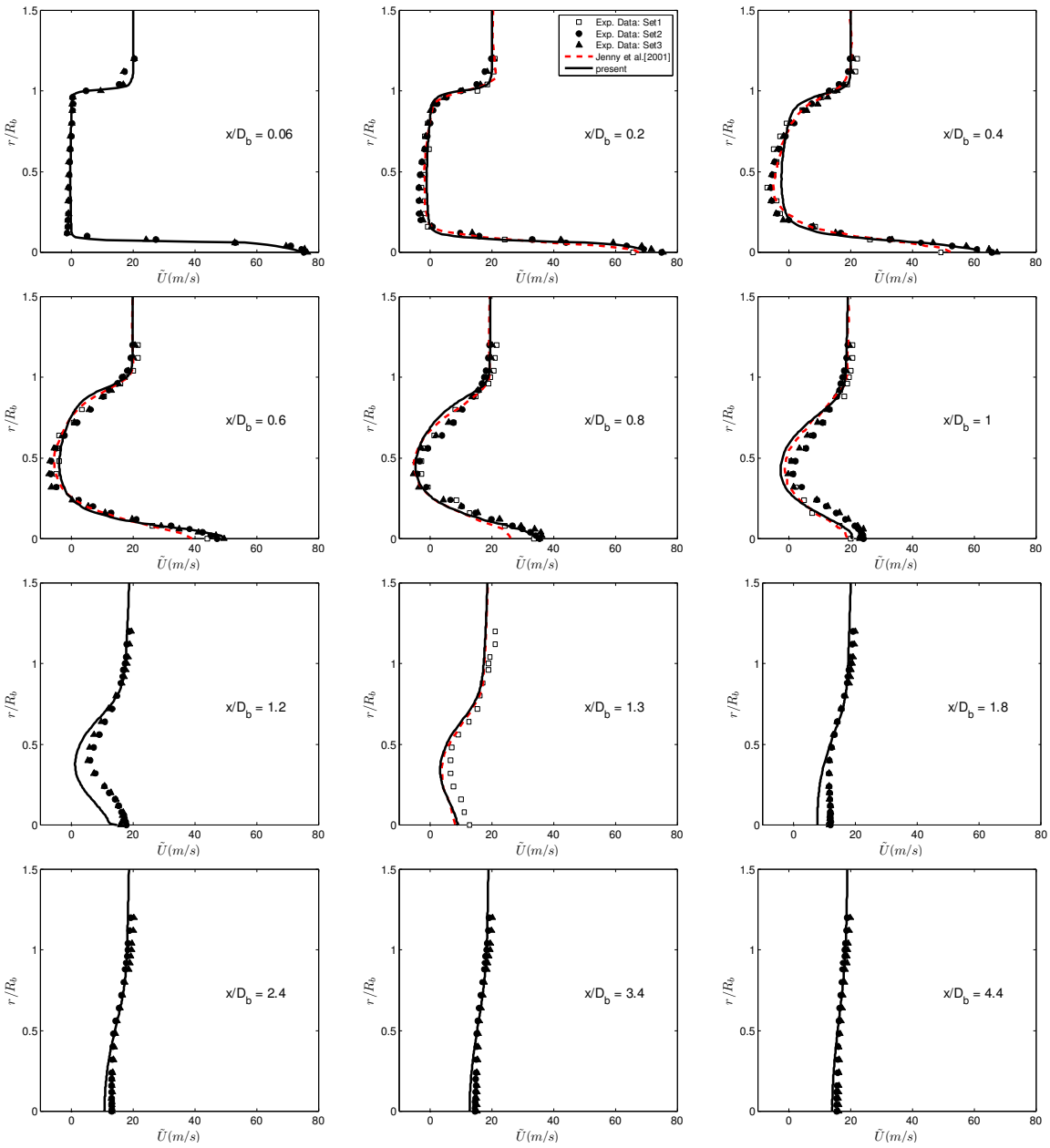


Figure 3.6: The cold bluff-body flow. Radial profiles of mean axial velocity compared with experimental data and with the PDF simulations performed using the old hybrid algorithm.

of the coordinate system is placed at the center of the fuel jet in the exit plane. The computational domain is $10D_b$ long in the axial direction and extends to $4D_b$ in the radial direction. A tensor product, orthogonal Cartesian grid is used with total of

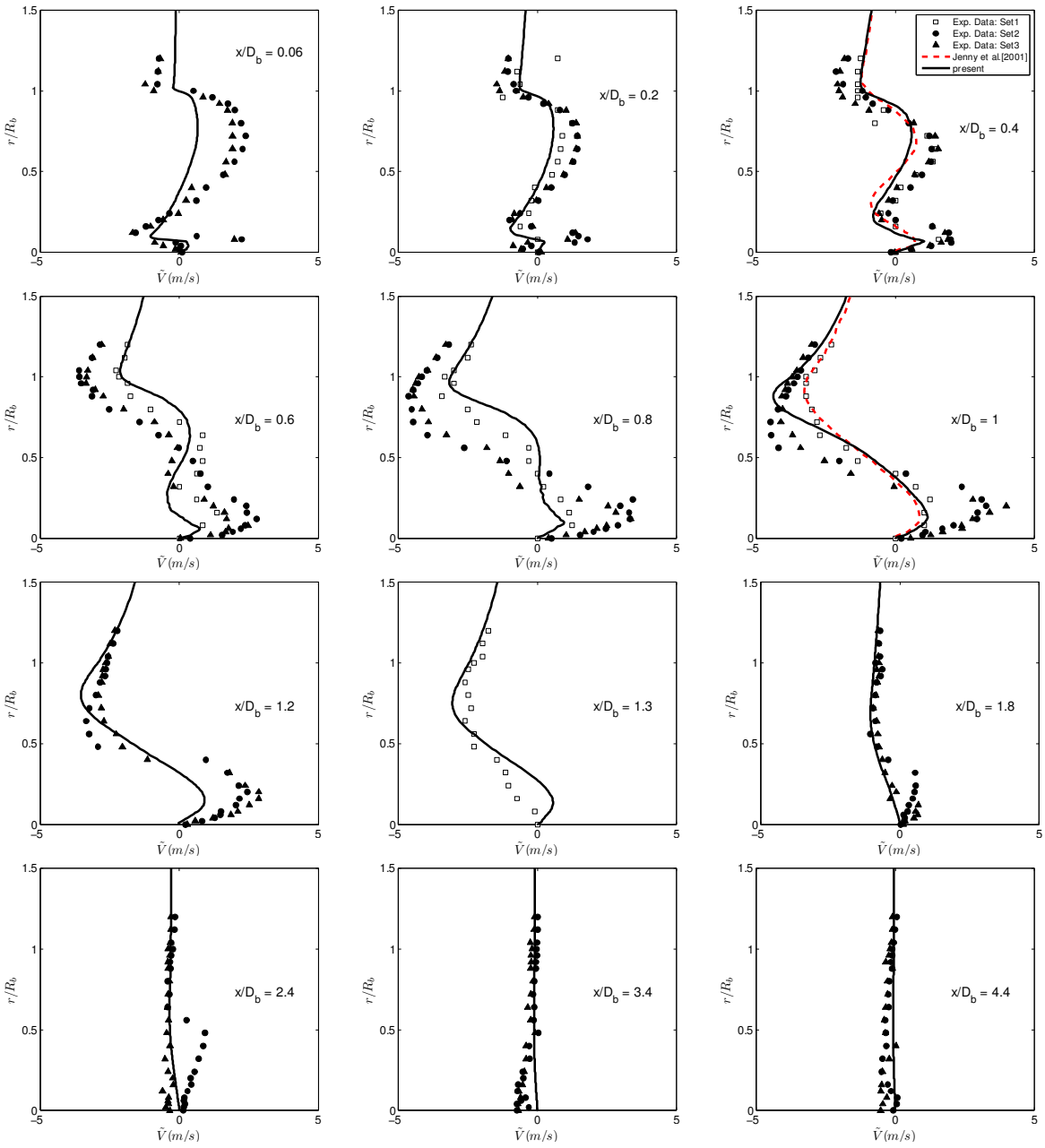


Figure 3.7: The cold bluff-body flow. Radial profiles of mean radial velocity compared with experimental data and with the PDF simulations performed using the old hybrid algorithm.

$M^2 = N_x \times N_r$ non-uniform cells. The grid is stretched both in the axial and radial directions.

The initial and boundary conditions are specified in the same way as in Muradoglu et al. [37] for all the quantities. The axial mean velocity is specified based on the

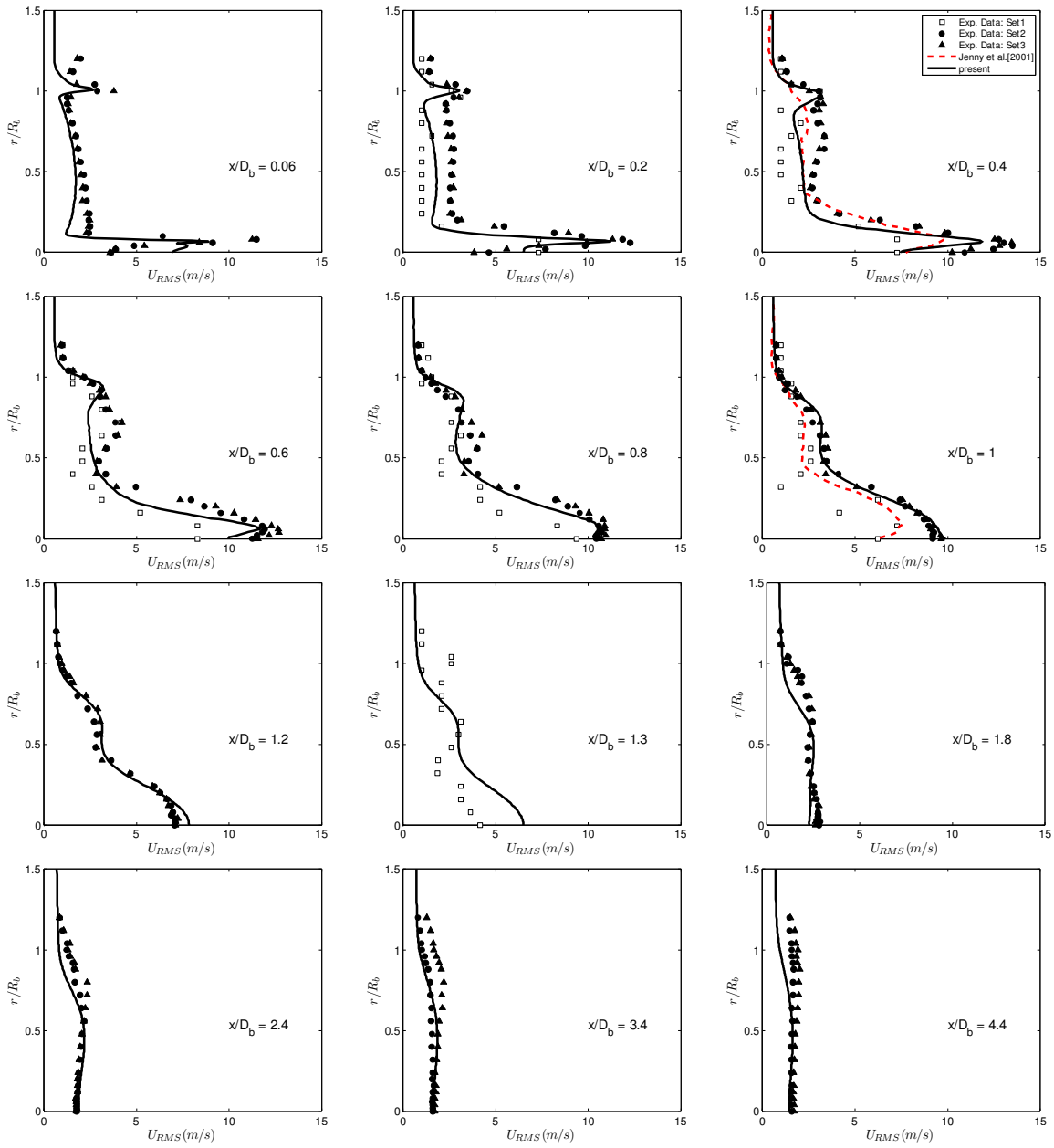


Figure 3.8: The cold bluff-body flow. Radial profiles of rms axial velocity compared with experimental data and with the PDF simulations performed using the old hybrid algorithm.

assumption of a fully developed turbulent pipe flow in the jet region while it is interpolated from the experimental data in the co-flow region. The axial and radial rms fluctuating velocities (U_{RMS} and V_{RMS}) are also interpolated from the experimental data both in the jet and co-flow regions, and the mean turbulent shear stress is then

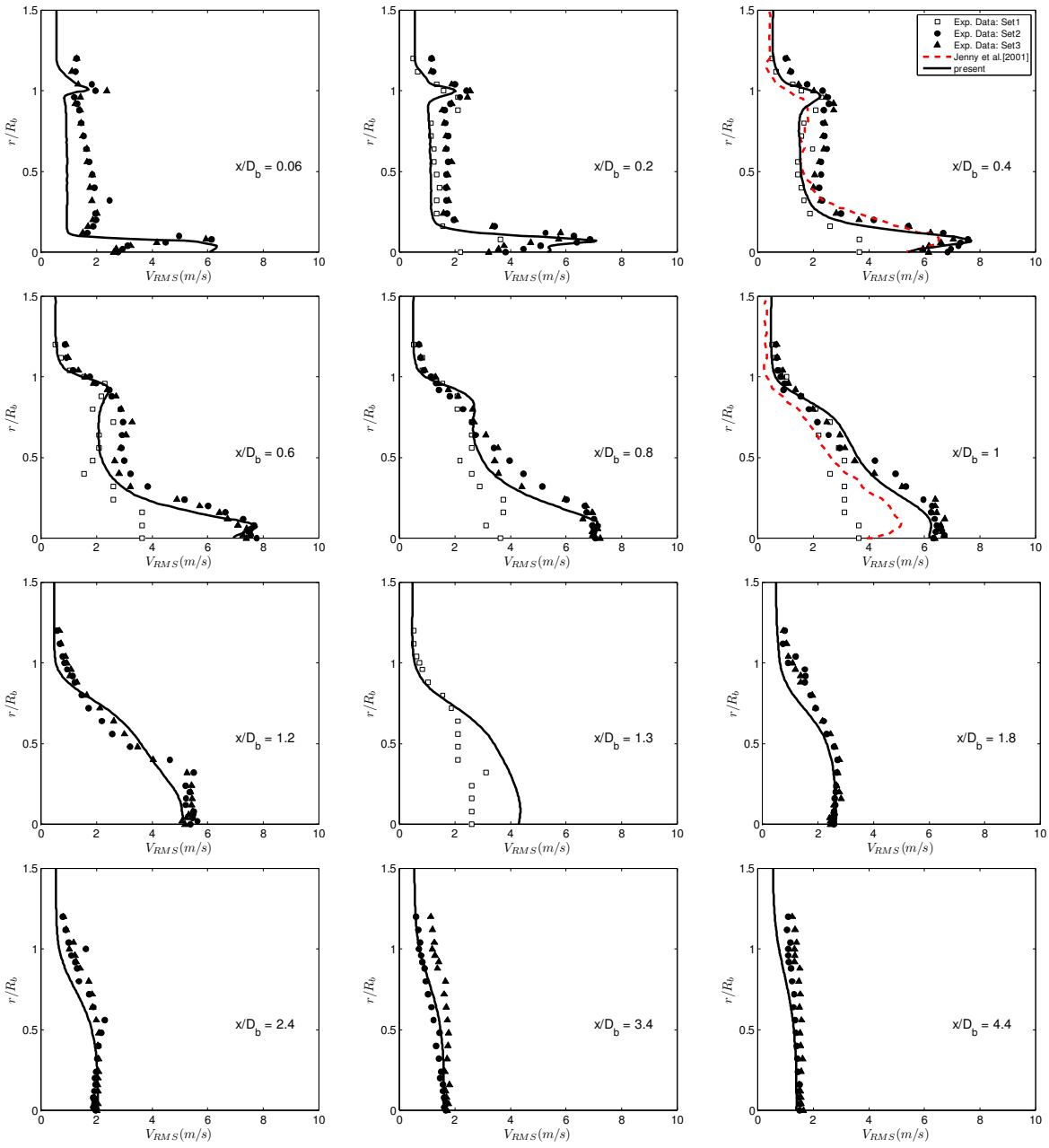


Figure 3.9: The cold bluff-body flow. Radial profiles of rms radial velocity compared with experimental data and with the PDF simulations performed using the old hybrid algorithm.

calculated as

$$\widetilde{uv} = \rho_{12}\sqrt{u^2 v^2}, \tag{3.1}$$

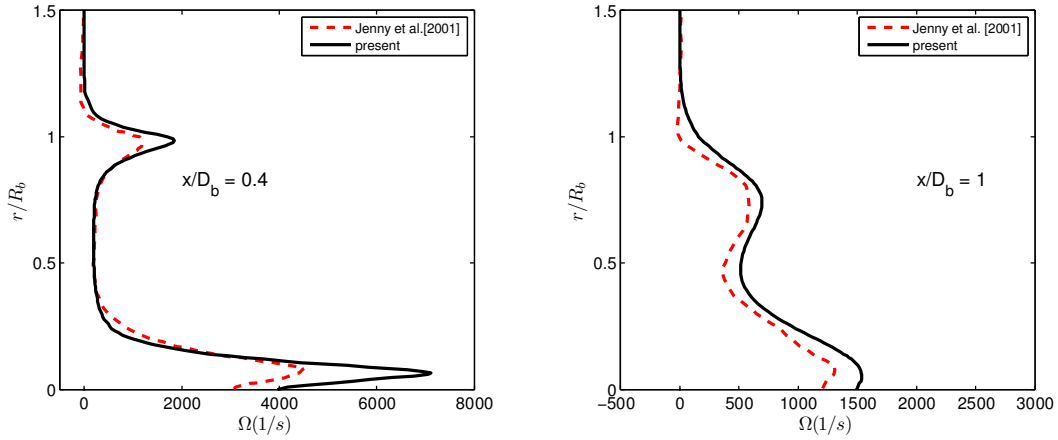


Figure 3.10: The cold bluff-body flow. The computed radial profiles of the conditional mean frequency compared with the PDF simulations obtained using the old hybrid algorithm at axial locations $x/D_b = 0.4$ and 1.0.

where $\rho_{12} = -0.4$ and $\rho_{12} = 0.5(r/R_j)$ in the co-flow and jet regions, respectively. Velocity components are specified at the inlet such that the fluctuating velocity PDF is joint normal with zero means. Based on the assumption of equilibrium between the production and dissipation, the mean turbulent frequency is calculated as

$$\tilde{\omega} = -\frac{\widetilde{uv}}{\tilde{k}}\frac{\partial \tilde{U}}{\partial r}. \tag{3.2}$$

Since the flow is dominated by the large recirculation zones and hence there is no need to resolve the boundary layer, perfect slip and no penetration boundary conditions are applied on the buff-body surface. The symmetry and far field boundary conditions are applied at the centerline and the outer boundaries, respectively. Pressure is fixed at the atmospheric pressure at the exit plane.

Table 3.2: Flow parameters for the non-swirling bluff-body flame 'HM1E'.

case	fuel (volume ratio)	U_c (m/s)	U_j (m/s)	T_{in} (K)	ξ_{st}
'HM1E'	CH4:H2(1:1)	35	108	298	0.05

3.4.1 Statistical stationary solution

The present hybrid method is designed to simulate statistically stationary flows. To show the statistical stationarity of the numerical solutions, time series of Favre-averaged mean axial velocity and turbulent kinetic energy are monitored at six probe locations as specified in Table 3.1. Figure 3.11 depicts the time histories of mean axial velocity and turbulent kinetic energy at these probe points. The results are obtained using a 114×114 grid and the number of particles per cell $N_{pc} = 50$. It can be seen that a statistical stationary solution is obtained after about 8000 particle time steps, which is comparable with the old hybrid algorithm.

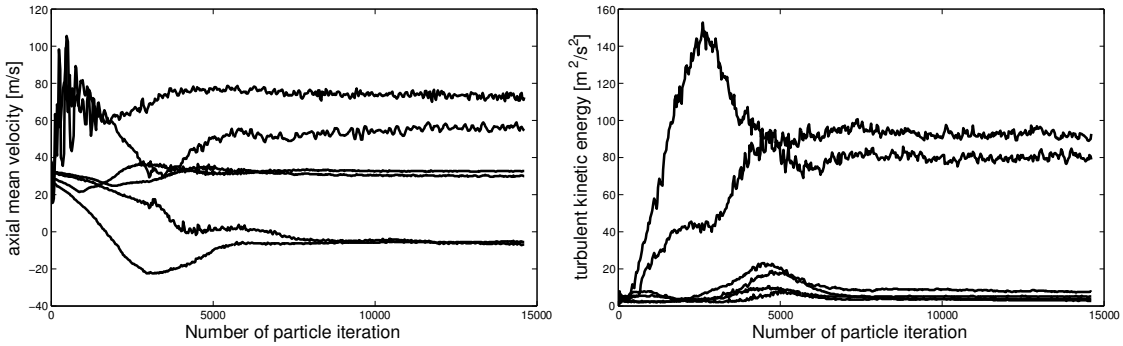


Figure 3.11: Time series of Favre-averaged mean axial velocity and turbulent kinetic energy at the six probe points.

3.4.2 Comparison with the earlier PDF simulations and the experimental data

The results are now compared with the earlier PDF simulations performed using the old hybrid algorithm [37] and also with the experimental data [75]. Note that two sets of experimental data have been reported for the 'HM1E' flame by the same group [75]. The new data sets were measured using a new experimental facility in the University of Sydney and thus expected to be more accurate. However the mixture

fraction measurements were not included in the new data sets. Therefore, the flow field quantities are compared with the latest experimental data while the mean and rms mixture fraction are compared with the old experimental data in which the jet and co-flow bulk velocities are set to 118 m/s and 40 m/s, respectively. An extensive study of numerical accuracy of the hybrid algorithm with respect to the grid convergence and bias error has been performed. It is found that all the results presented here are numerically accurate within 5% error tolerance as will be discussed in sections 3.4.3 and 3.4.4.

First the mean streamlines are computed using both the old and new hybrid algorithm and plotted in the vicinity of the recirculation zone (RZ) in Fig. 3.12. Since the streamlines were not reported by Muradoglu et al. [37], the computations are repeated using the old loosely-coupled hybrid code *HYB2D* [39]. In spite of qualitative similarity of streamline patterns in Fig. 3.12, the length of the recirculation zone is predicted as $\ell_r/D_b \approx 1.65$ and $\ell_r/D_b \approx 1.4$ by the present and old hybrid algorithms, respectively. Note that the present result is in better agreement with the experimental value of $\ell_r/D_b \approx 1.6$ [7]. In addition, the shape and length of RZ obtained by the new algorithm are consistent with the LES results reported by Raman and Pitsch [54] who give the length of the recirculation region as $\ell_r/D_b \approx 1.65$. For a better quantitative comparison, the radial profiles of mean axial velocity ($\tilde{U}$), mean radial velocity ($\tilde{V}$), the rms axial fluctuating velocity (U_{RMS}) and the rms radial fluctuating velocity (V_{RMS}) are plotted in Figs. 5.1-3.16, respectively, at the axial locations of $x/D_b = 0.06, 0.2, 0.4, 0.8, 1.0, 1.4, 1.8, 2.4$ and 3.4. These figures show that there is overall good agreement between the present results and the results obtained by the old hybrid algorithm demonstrating the accuracy of the present hybrid method. Only exception is the axial location of $x/D_b = 1.4$ where the edge of RZ is located and thus the axial velocity is significantly under predicted near the centerline by the old hybrid algorithm. In addiction, there is good agreement between the present

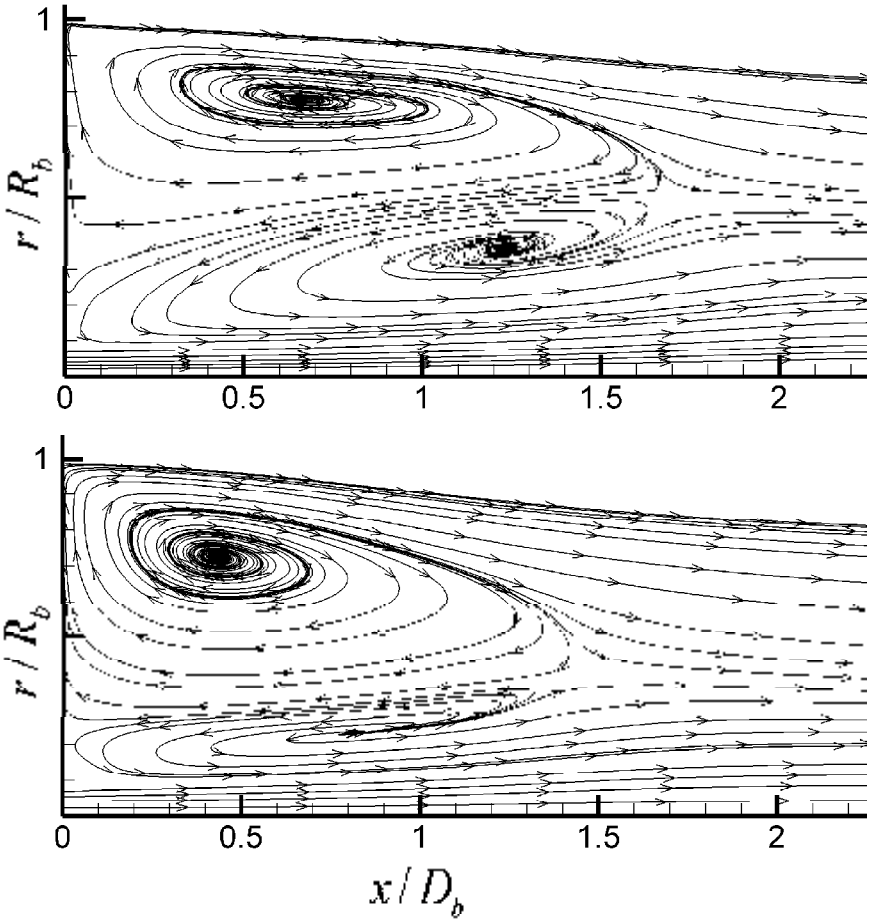


Figure 3.12: The streamlines of the mean velocity in the recirculation zone of 'HM1E' flame. The top streamlines are obtained by the new algorithm and the bottom one by the old hybrid algorithm.

calculations and the experimental data at the axial locations up to the end of RZ. Starting from the axial location $x/D_b = 1.8$, the results deteriorate especially near the axis of symmetry for the mean axial velocity. The rms velocities are predicted very well at most of axial locations especially before $x/D_b = 2.4$ as can bee seen in Figs. 3.15–3.16. Finally, the radial profiles of the mean and rms of mixture fraction are plotted in Figs. 3.17–3.18 at six axial locations together with the experimental data and with the earlier PDF simulations. As can be seen in these figures, the present results are overall in good agreement with the earlier PDF simulations. Compared to the experimental data, both quantities are reasonably well predicted in most of the axial locations except for the very downstream location of $x/D_b = 2.4$ where the

mean mixture fraction is under predicted and between $x/D_b = 0.9$ and $x/D_b = 1.8$ where the rms mixture fraction is over predicted near the centerline.

In summary, the present results are found to be in a good agreement with the earlier PDF simulations performed using the old hybrid solution algorithm demonstrating the accuracy of the new hybrid method. Thus the differences between computational and experimental results are mainly attributed to the deficiency of the sub-models. However, considering the fact that the simplest sub-models are used in the present calculations, the performance of the PDF model is remarkable and is expected to improve significantly when more advanced models are employed.

3.4.3 Spatial error

Extensive simulations are performed to demonstrate grid convergence of the present hybrid method by successively refining the computational grid from 64×64 up to 216×216. The spatial error results from the spatial discretization in the finite-volume method and also from the kernel estimation and interpolation schemes used in the particle algorithm. All the simulations are performed with the number of particles per cell $N_{pc} = 50$ and the time-averaging factor $N_{TA} = 500$. The time-averaged profiles of mean axial and radial velocity, rms axial and radial velocities, and mean and rms mixture fraction are plotted in Fig. 3.19 at the axial location $x/D_b = 0.4$ to show overall dependence of the calculated results on the grid refinement. As can seen in these figures, the difference among the profiles is decreasing with grid refinement, indicating that grid convergence is achieved. To verify the second-order spatial accuracy of the method, the mean quantities, $\tilde{U}$, Ω, U_{RMS}, V_{RMS}, $\tilde{\xi}$ and ξ_{RMS} are also plotted against the inverse of total number of grid cells M^{-2} at the locations $(x/D_b, r/R_j) = (1,1)$, $(x/D_b, r/R_b) = (1,0.5)$ and $(x/D_b, r/R_b) = (1,1)$ in Fig. 3.20 where the symbols represent the numerical data and the solid lines are the linear least-squares fits to the data. As can be seen in this figure, the approximate linear

relationship between the mean quantities and M^{-2} confirms the expected second-order spatial accuracy of the method. Assuming a second order accuracy and using the Richardson extrapolation, the spatial error free values are obtained from Fig. 3.20 as $M \to \infty$ and then the relative error is computed as

$$\epsilon = \frac{|Q_M - Q_\infty|}{|Q_\infty|}, \tag{3.3}$$

where Q_M is the numerical result obtained using a grid with M^2 grid cells and Q_∞ is predicted using Richardson extrapolation as $M \to \infty$. Table 3.3 summarizes the average percentage spatial error at the six probe points. As can be seen in this table, a grid containing 216×216 cells is sufficient for the spatial error to be less than 5% in all the mean quantities at these locations.

Table 3.3: Percentage spatial discretization error for mean and fluctuating quantities obtained with various grid resolutions.

Quantities	$\tilde{U}$	$\tilde{V}$	U_{RMS}	V_{RMS}	Ω	$\tilde{\xi}$	ξ_{RMS}
64×64	16.5	21.2	23.2	31.0	15.5	12.2	21.1
96×96	12.8	16.3	15.0	20.2	10.5	8.5	14.0
144×144	7.8	9.1	4.7	8.5	6.6	4.0	6.4
216×216	4.7	4.9	2.6	2.9	2.0	2.8	3.1

3.4.4 Bias error

Bias error is a deterministic numerical error caused by the fluctuations in the particle mean fields used in the equations solved by the particle method. The bias error is expected to scale as N_{pc}^{-1} where N_{pc} is the number of particles per cell [72]. Although the bias error was a major problem in the stand alone particle method [72], it has been shown that it is virtually eliminated in the consistent hybrid approach [40, 21, 39]. Extensive simulations are performed here to quantify the bias error in the present hybrid method using a 216×216 grid. The time-averaged profiles of the mean axial

and radial velocities, the rms fluctuating axial and radial velocities, and the mean and rms mixture fraction at the axial location $x/D_b = 0.8$ are plotted in Fig. 3.22 for $N_{pc} = 30, 60, 120$ and 240. Time averaging parameter is set to $N_{TA} = 500$ to reduce the statistical fluctuations. As can be seen in this figure, the profiles are close to each other indicating that the bias error is small. Figure 3.22 shows the time-averaged and normalized mean and fluctuating values of flow quantities against N_{pc}^{-1} at the locations $(x/D_b, r/R_j) = (1, 1)$, $(x/D_b, r/R_b) = (1, 0.5)$ and $(x/D_b, r/R_b) = (1, 1)$. The approximate linear relationship between the mean quantities and N_{pc}^{-1} confirms the expected scaling of the bias error. The slopes of the lines indicate the sensitivity of the solutions to the bias error. The average bias error at the six probe points are summarized in Table 3.4. The relative bias error is calculated as

$$\epsilon = \frac{|Q_{N_{pc}} - Q_{N_{pc}\to\infty}|}{|Q_{N_{pc}\to\infty}|}, \tag{3.4}$$

where $Q_{N_{pc}}$ is the numerical result obtained using N_{pc} particles per cell and $Q_{N_{pc}\to\infty}$ is predicted using the Richardson extrapolation as $N_{pc} \to \infty$. It can be seen that the bias error for a given value of N_{pc} in the present hybrid method is much smaller than the stand-alone particle/mesh method [72], and comparable to the bias error in the old hybrid algorithm. It is also seen in these figures that $N_{pc} = 50$ is sufficient to virtually eliminate the bias error compared to the spatial error on a typical grid used.

Table 3.4: Percentage bias error for mean and fluctuating quantities obtained using various number of particles per cell.

Quantities	$\tilde{U}$	$\tilde{V}$	U_{RMS}	V_{RMS}	Ω	$\tilde{\xi}$	ξ_{RMS}
$N_{pc} = 30$	8.7	9.2	6.0	5.4	7.5	2.7	7.3
$N_{pc} = 60$	2.5	3.3	2.9	1.3	3.9	1.8	3.4
$N_{pc} = 120$	2.4	2.7	1.9	1.1	3.3	0.6	2.9
$N_{pc} = 240$	1.2	1.5	1.6	1.0	1.0	0.4	0.6

3.5 Summary

In this chapter the new hybrid algorithm is first applied to the cold bluff-body flow. In the old hybrid method the results for non-reacting bluff-body flow [21] were presented for grids containing 32×32 and 64×64 cells and for finer grids the old loosely coupled method produced nonphysical vortex shedding. It has been demonstrated that the new hybrid algorithm does not show such a behavior and flow successfully reaches a statistically stationary state even when much finer grid is used. It is found that the new hybrid algorithm is generally very robust against grid refinement both for non-reacting and reacting bluff-body flows. For determining the numerical property of the new algorithm, comprehensive calculations are performed for buff-body stabilized flame 'HM1E'. It is found that the new hybrid method captures the flow characteristics of the bluff-body flame in the recirculation region better than the original hybrid method. In addition, the convergence of the method is demonstrated for spatial and bias errors. The results are found to be in good agreement with available experimental data. In the next chapter the robustness of the new algorithm is further studied for much complicated flow of the Sydney swirling bluff-body flame.

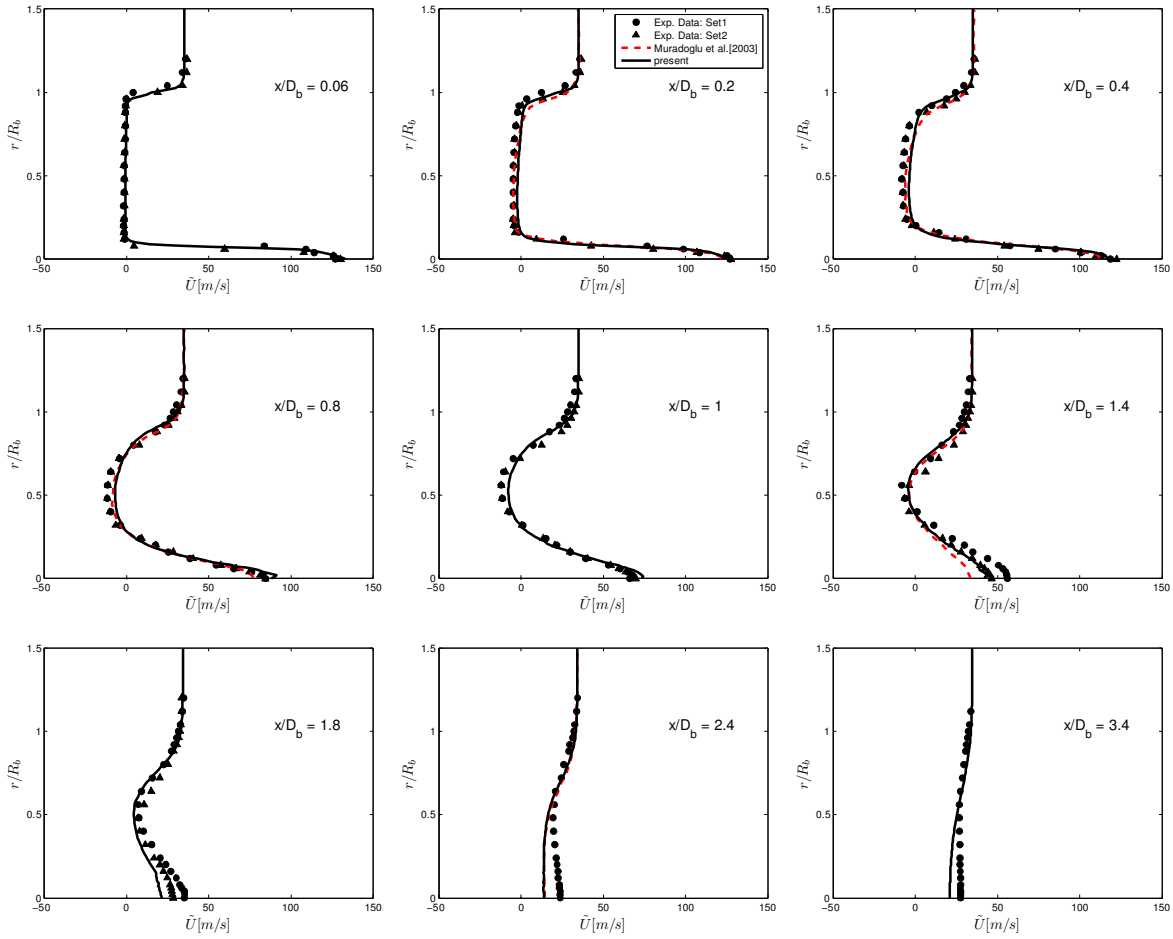


Figure 3.13: The bluff-body flame 'HM1E'. Radial profiles of mean axial velocity compared with the experimental data (symbols) and the earlier PDF simulations of Muradoglu et al. [37] (red dashed lines).

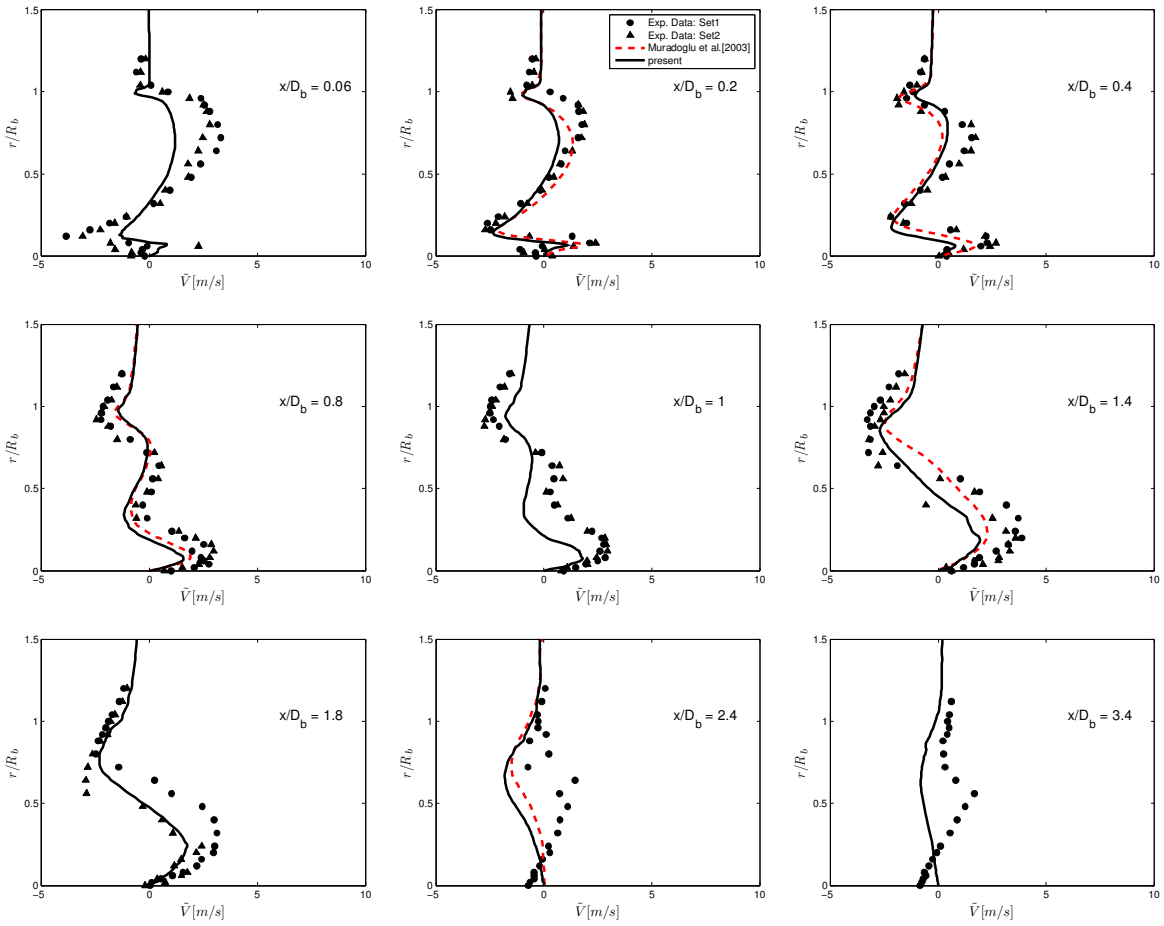


Figure 3.14: The bluff-body flame 'HM1E'. Radial profiles of mean radial velocity compared with the experimental data (symbols) and the earlier PDF simulations of Muradoglu et al. [37] (red dashed lines).

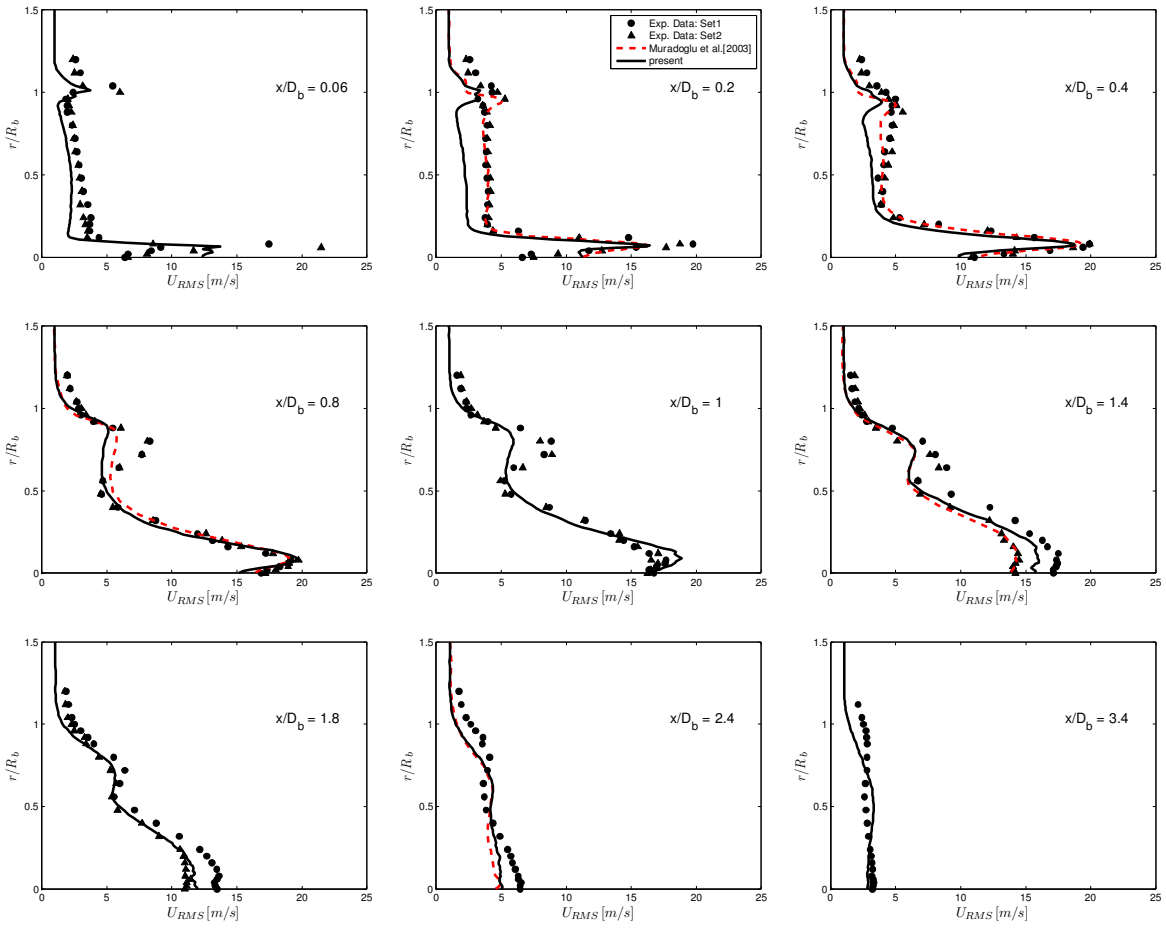


Figure 3.15: The bluff-body flame 'HM1E'. Radial profiles of rms axial velocity compared with the experimental data (symbols) and the earlier PDF simulations of Muradoglu et al. [37] (red dashed lines).

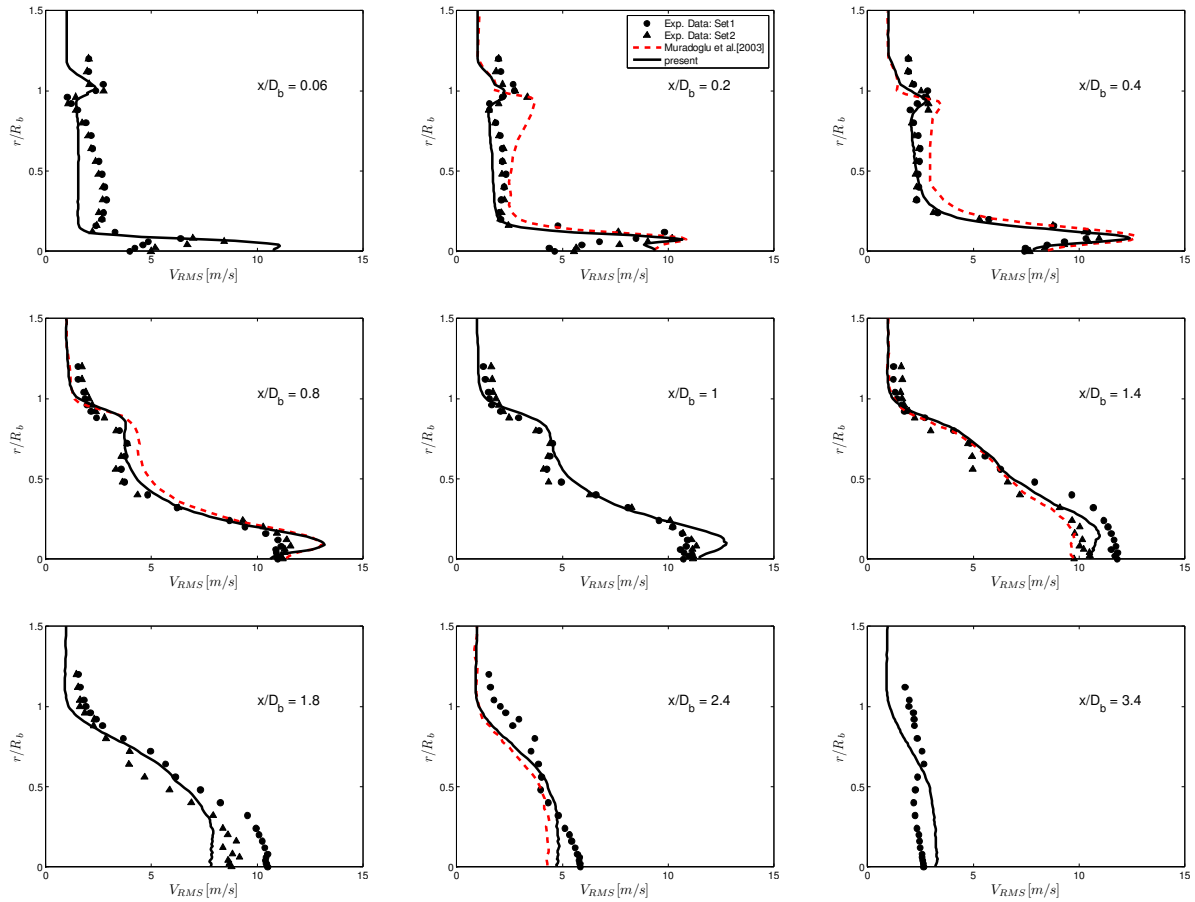


Figure 3.16: The bluff-body flame 'HM1E'. Radial profiles of rms radial velocity compared with the experimental data (symbols) and the earlier PDF simulations of Muradoglu et al. [37] (red dashed lines).

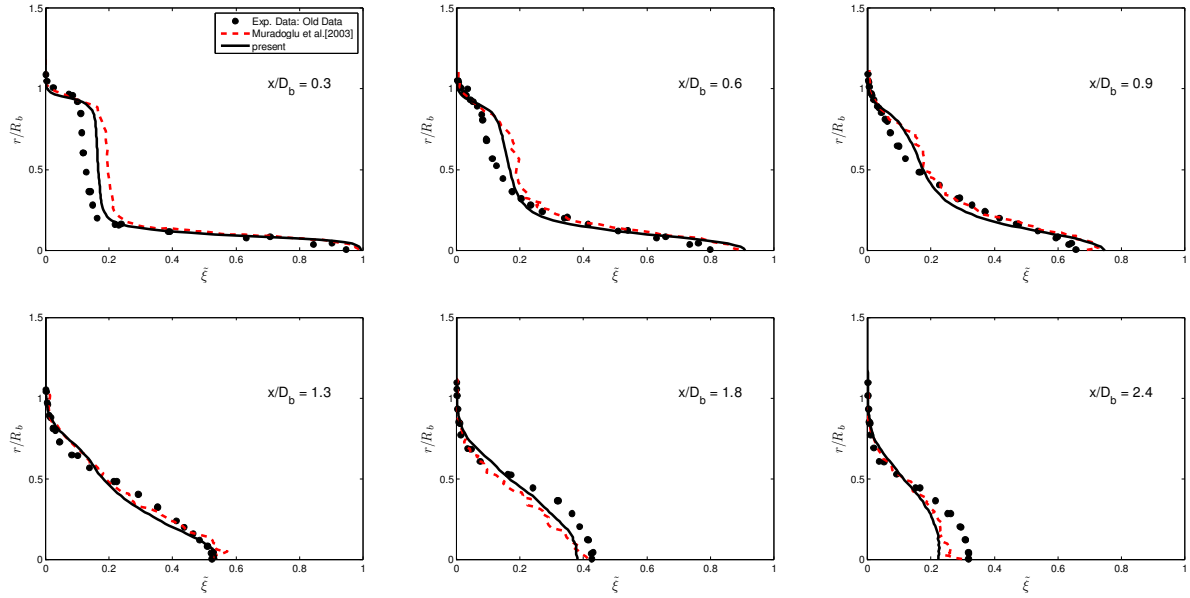


Figure 3.17: The bluff-body flame 'HM1E'. Radial profiles of mean mixture fraction compared with the experimental data (symbols) and the earlier PDF simulations of Muradoglu et al. [37] (red dashed lines).

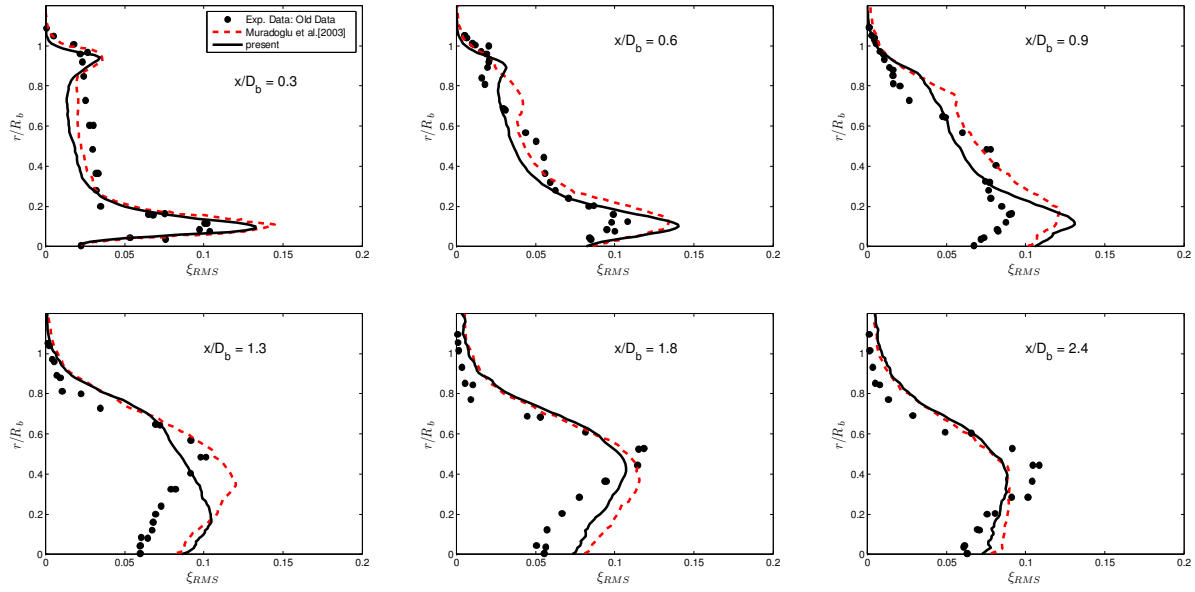


Figure 3.18: The bluff-body flame 'HM1E'. Radial profiles of rms mixture fraction compared with the experimental data (symbols) and the earlier PDF simulations of Muradoglu et al. [37] (red dashed lines).

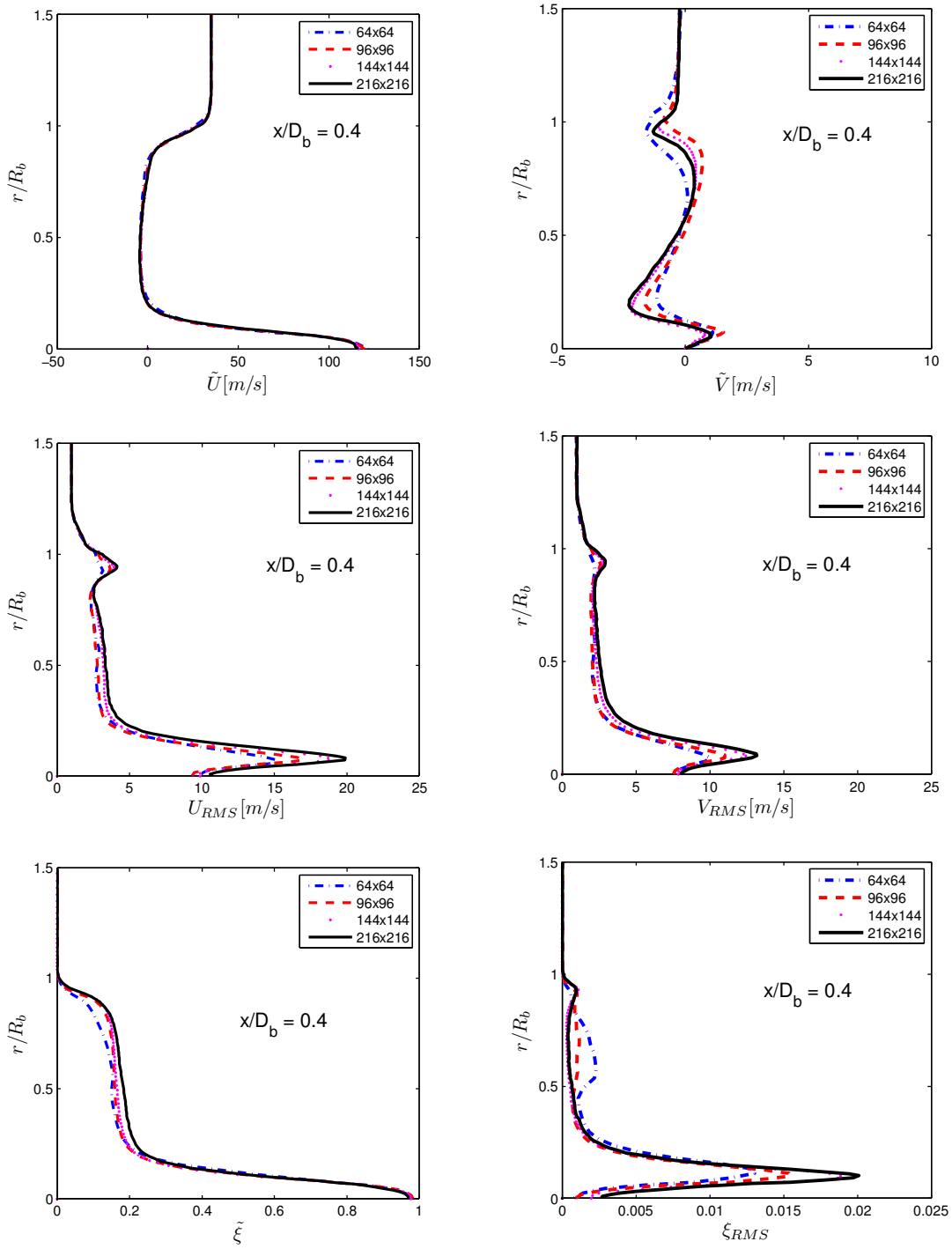


Figure 3.19: The bluff-body flame 'HM1E'. Grid convergence: Radial profiles of mean and rms fluctuating axial and radial velocities, mean and rms mixture fraction at axial location $x/D_b = 0.4$.

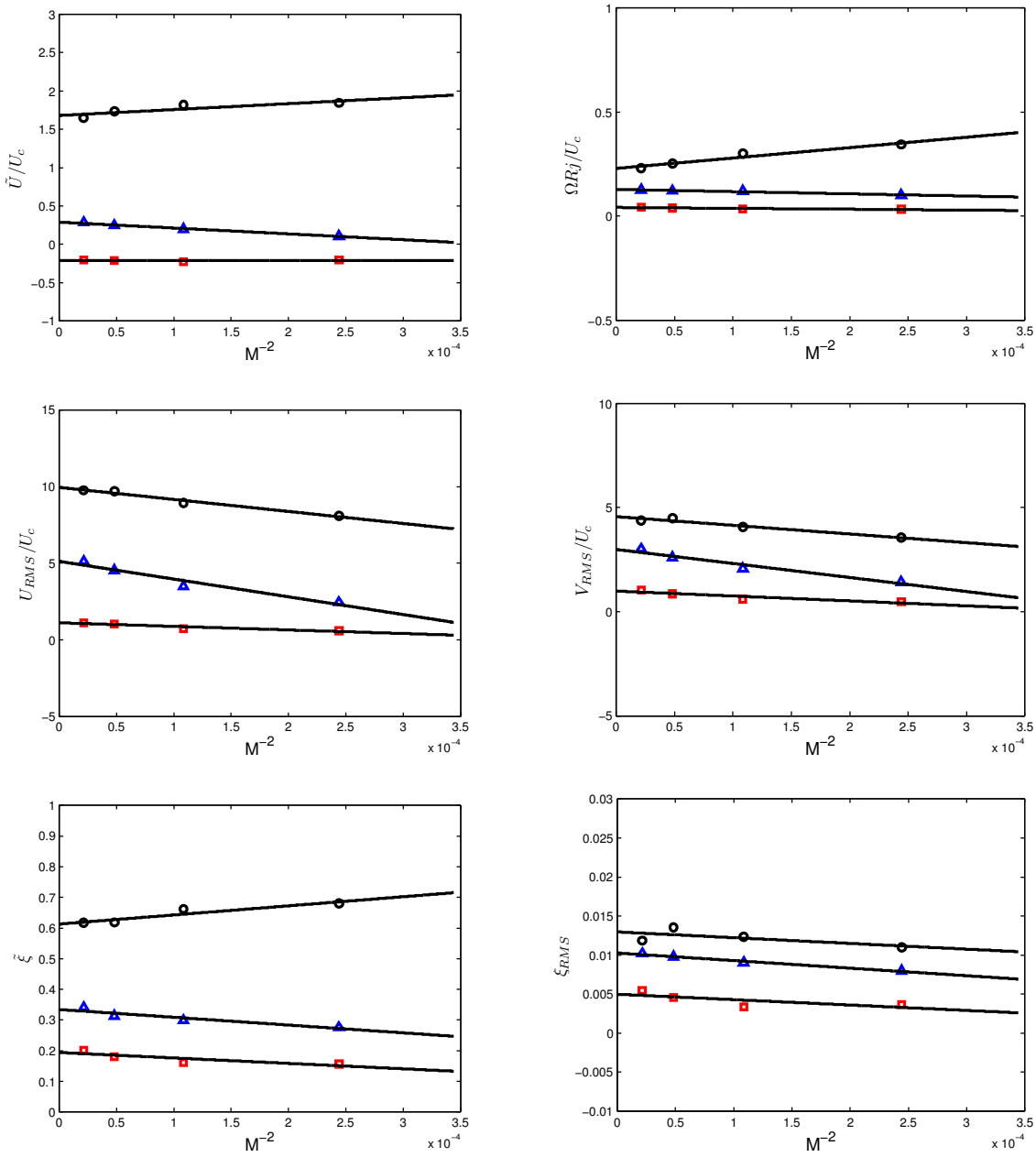


Figure 3.20: The bluff-body flame 'HM1E'. Grid convergence: Mean and fluctuating quantities against M^{-2} at selected points. Circles indicate the location at $(x/D_b = 1.0, r/R_j = 1)$, triangles at $(x/D_b = 1.0, r/R_b = 0.5)$, squares at $(x/D_b = 1.0, r/R_b = 1.0)$, and the solid lines show the linear least squares fits to the computational results.

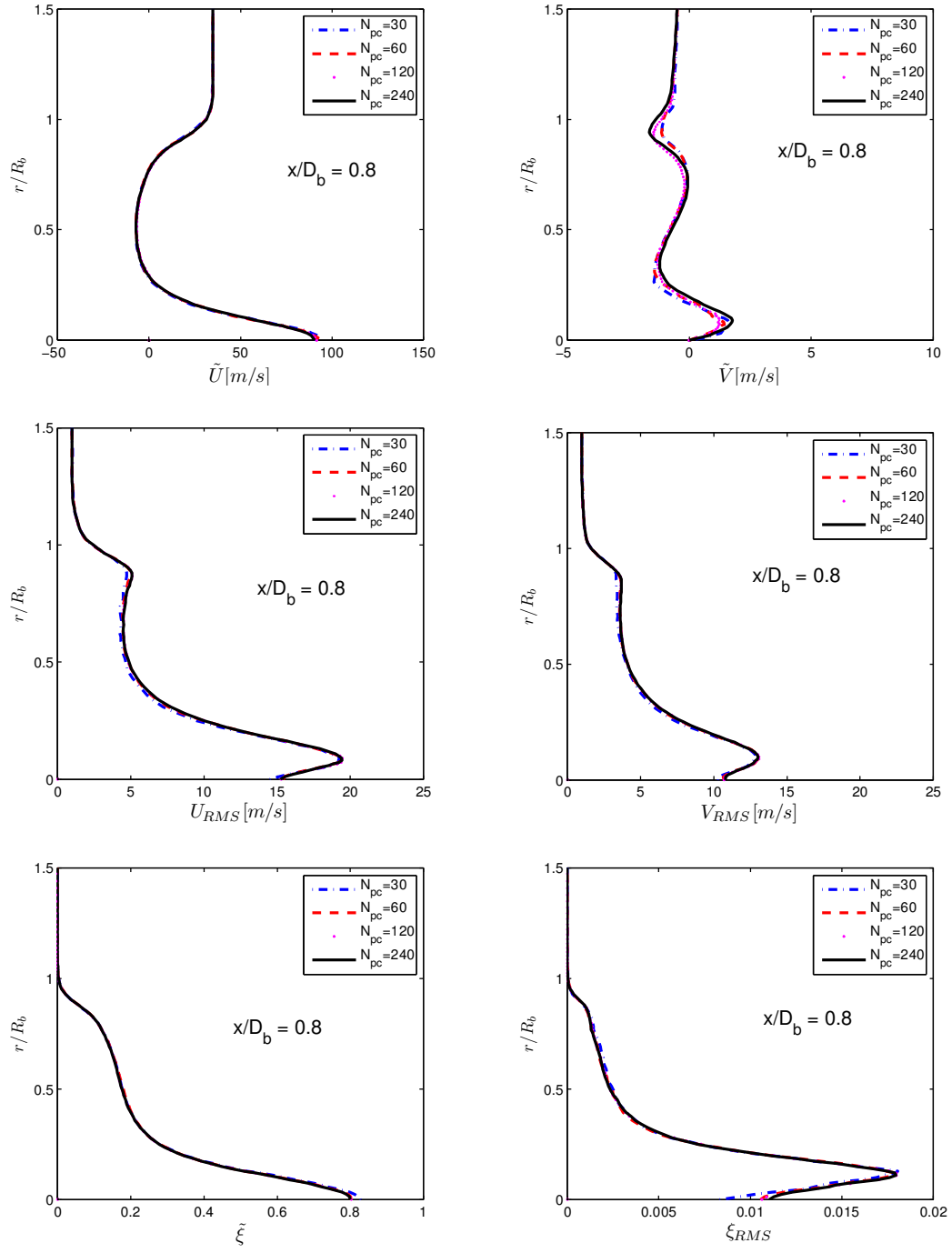


Figure 3.21: The bluff-body flame 'HM1E'. Bias error: Radial profiles of mean and rms fluctuating axial and radial velocities, mean and rms mixture fraction at axial location $x/D_b = 0.8$.

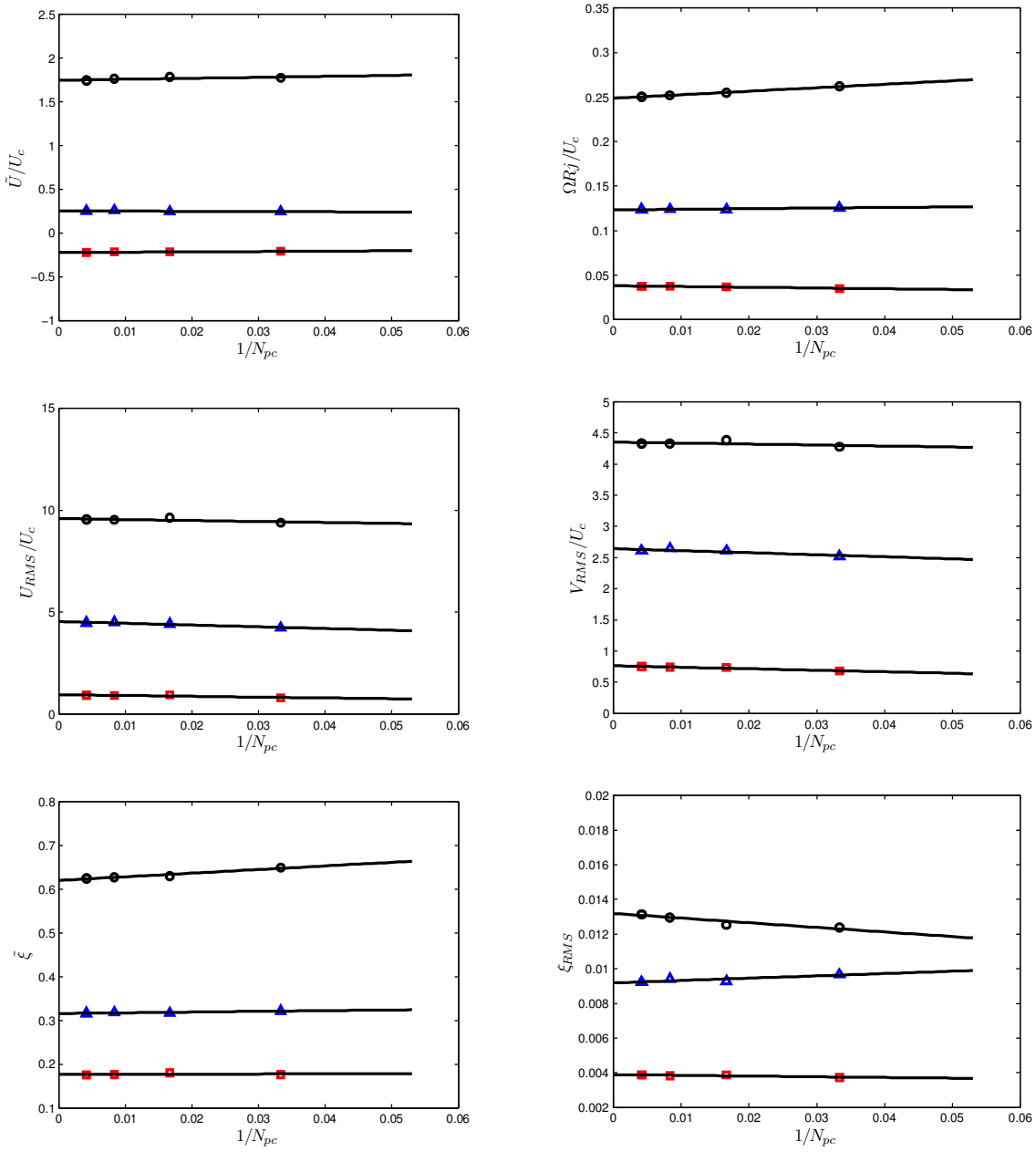


Figure 3.22: The bluff-body flame 'HM1E'. Bias error: Mean and fluctuating quantities against $1/N_{pc}$ at selected points. Circles indicate the location at $(x/D_b = 1.0, r/R_j = 1)$, triangles at $(x/D_b = 1.0, r/R_b = 0.5)$, squares at $(x/D_b = 1.0, r/R_b = 1.0)$, and solid lines show the linear least squares fits to the computational results.

Chapter 4

Swirling Bluff-Body Flame

4.1 Introduction

Swirling flows are observed in nature such as typhoons and tornadoes and have been applied in a wide range of non-reacting and reacting systems for many years. Cyclone separators, spraying systems, and jet pumps are examples of non-reacting applications while gas turbines, utility boilers, industrial furnaces, and internal combustion engines represent the reacting systems. The importance and complexity of these flows have preoccupied researchers for decades.

In industrial burners swirl has been used to stabilize non-premixed flames. A sufficiently strong swirl creates a high depression in the jet core, which leads to a vortex breakdown bubble (VBB). It is a closed, standing, toroidal vortex which forms with flow reversal in the core region. The reverse flow carries hot combustion gases back to the burner exit thus providing a stable source of heat and active species for flame ignition. The enhanced mixing and entertainment of ambient air close to the burner exit provide favourable conditions for efficient combustion. These bring several benefits of practical relevance such as the reduction of the flame length and the expansion of the range of operating parameters at which the burner can function

in a stable regime. It also results in compact combustion processes with reduced emission of nitrogen oxides.

Most of studies on swirling flames consider confined flows since these are more relevant to industrial applications such as combustors in gas turbines and utility boilers. Experimental studies of confined swirling flames were recently reported by, for example, Weigand et al. [69], Meier et al. [34], and Olivani et al. [43]. However, the confinement increases the complexity of the flow due to stronger effects of jet precession and possible acoustic instabilities, presence of additional recirculation zones, and complicates the specification of boundary conditions, as was pointed out by Al-Abdeli and Masri [2]. Although of less practical interest, the unconfined stable swirling flames are considered to be more amenable to computational studies and easily accessible to laser diagnostic techniques [2]. The stable flames in the vortex-breakdown regime are still of a higher level of complexity than e.g., jet diffusion flames, because of the presence of a strong reverse flow, intense mixing of hot products, fuel and air, the occurrence of local extinction and re-ignition. Therefore, even though they are of less practical interest, the unconfined swirling bluff-body flames investigated by the Sydney group [75] were designed to provide benchmark experimental data for the purpose of validating and developing computational methods and introducing the turbulence and combustion models for the swirling flames [1, 31].

The swirling flames have received substantial attention in recent years and modeled using various approaches. However the prediction of the complex flow field with recirculation and vortex breakdown and also unsteady behaviour such as jet precession are computationally difficult. Various models and numerical methods have been applied to predict swirling flames in laboratory scale experiments as well as industrial applications. Reynolds averaged N-S equations along with various turbulent models have been used to predict swirl flows [58, 68]. In general RANS based models are not capable to capture flow feature of swirling flows. Large eddy simulation (LES)

techniques on the other hand solve for large scale unsteady behaviour of turbulent flows. El-Asrag and Menon [12] have carried out LES simulation of Sydney swirling bluff-body flame using linear eddy model for combustion. Their results were in good agreement with the experimental data. Stein and Kempf [59] have also performed LES calculation of Sydney isothermal swirling flow as well as two different swirling flames using laminar flamelet approach. Malalasekera et al. [30, 29] accomplished LES simulations for different isothermal swirling flows and also a reacting case using a steady laminar flamelet model together with a presumed PDF approach as the combustion model.

Although unsteady three dimensional effects are in principle better handled by LES than RANS models, LES requires much higher computational cost. However LES has exactly the same problem as do RANS models since the nonlinear chemical reactions appear to be in unclosed form in both approaches. Here PDF method emerges as an alternative method with its own advantages of dealing with chemical reaction and convection without any approximation. Masri et al. [32] performed PDF calculations of a swirling flame with a simple flamelet model but only mean and rms velocity fields were reported. De Meester et al. [8] recently have performed PDF calculations of a Sydney swirling flame using a scalar PDF approach with a progress variable approach for chemical kinetics.

In Chapter 3 the new hybrid method was applied to simulate the non-swirling cold and reacting bluff-body flows. The numerical performance of the new algorithm was demonstrated for the bluff-body stabilized flame. It was found that the method is very robust for the non-reacting and reacting bluff-body flows. In this chapter the overall performance and particularly robustness of the new hybrid method is studied further by simulating a more complex flow of a Sydney swirl stabilized bluff-body flame. For this purpose, among different swirling flames, the case labeled as 'SM1' is chosen as a test case since it exhibits the least jet precession.

To reduce the computational cost and facilitate extensive simulations a simple flamelet model is used for the treatment of chemical reactions. The flamelet library is formed based on the laminar flame calculations at a moderate strain rate of $a = 100$ 1/s using the GRI 2.1 detailed chemistry model [73] as for the non-swirling case. In Chapter 5 the detailed chemistry calculations of this flame will also be presented.

4.2 Sydney Swirl Burner

Sydney swirl burner is a laboratory-scale burner which closely resembles practical combustors. The criteria considered in designing this burner were i) strong enough swirl to cause vortex breakdown, ii) simple well-defined boundary conditions, iii) amenability to laser diagnostics methods, and iv) region of flame where the interaction between turbulence and chemistry is significant [32]. Design and construction of this burner aimed at understanding the structure of swirling flame and providing comprehensive data bank which can be used as a benchmark for model validation.

A schematic configuration of Sydney swirl burner is shown in Fig. 4.1. Swirl is induced aerodynamically into the primary air stream at a distance of 300 mm upstream of the burner exit. This occurs by three tangential ports that are inclined at 15° upwards and located circumferentially at 120° to each other. Two diametrically opposed ports, also located on the periphery of the burner, but ahead of the tangential inlets which supply the axial air stream [2]. Burner has a 50 mm diameter bluff-body with a 3.6 mm central fuel jet. Swirling air is provided through a 60 mm diameter annulus surrounding the bluff-body. The burner is placed inside a wind tunnel with a square cross section. The wind tunnel provides a secondary air coflow with free stream turbulence level of 2% [31]. Further details of the burner can be found in [2]. Comprehensive experimental measurements have been made for eight flames using this burner and the results have been reported by Al-Abdeli and Masri [1, 2], Kalt et

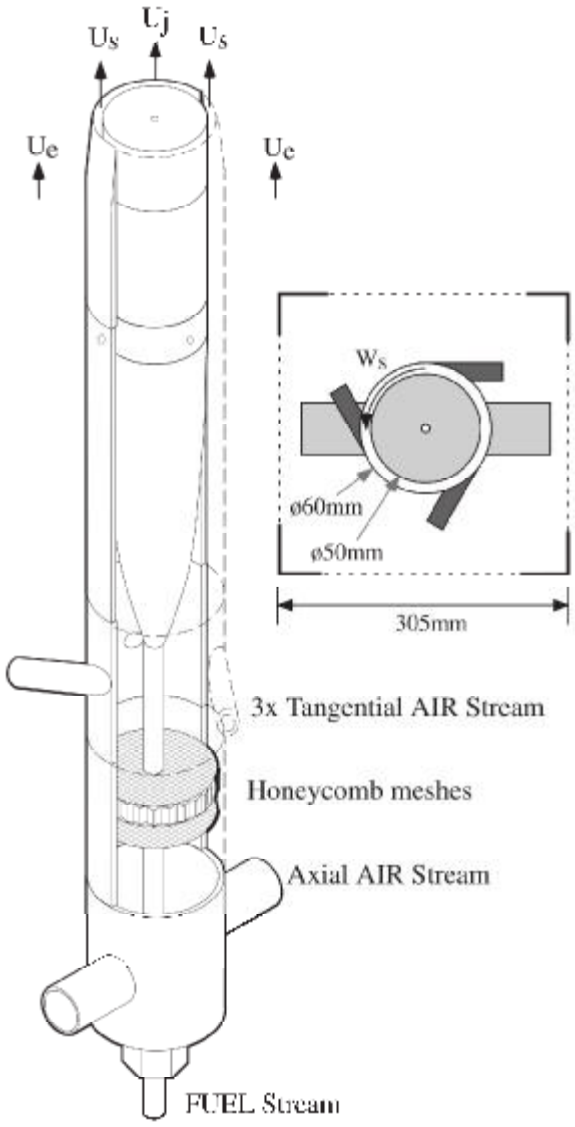


Figure 4.1: Sydney swirl burner [75].

al. [22], and Masri et al. [31]. The complete set of experimental data is also available online [75]. Note that the composition measurements were made at Sandia National Laboratories [22, 31]. Five characteristics distinguish them from each other: the bulk axial velocity of the central jet (U_j), the bulk axial and tangential velocities of the swirling air annulus (U_s and W_s), the bulk axial velocity of the coflow of the wind tunnel (U_e) and also with the type of fuel. It is known that the swirling bluff-body flame exhibit significant unsteadiness due to precessing of the recirculation zone in

axial direction [1, 22, 31]. As mentioned before, the present hybrid method is designed to simulate only statistically stationary flows, so the case labeled as 'SM1' is chosen as a test case here since it exhibits the least precession. Flow parameters of flame 'SM1' are summarized in Table 4.1. Here S_g is geometric swirl number defined as $S_g = W_s/U_s$.

Table 4.1: Flow parameters of the case 'SM1'.

case	fuel	$U_e(m/s)$	$U_j(m/s)$	$U_s(m/s)$	$W_s(m/s)$	S_g
SM1	CH4	20	32.7	38.2	19.1	0.5

4.3 Boundary Conditions

The flow is statistically axisymmetric, so axisymetric boundary conditions are employed at the centerline. A cylindrical coordinate system has been adopted for this purpose. The origin of the coordinate system is on the centerline of the jet exit plane ($x = 0, r = 0$). Figure 4.2 shows the rectangular domain used in the present calculations. Domain is extended 0.5 m ($10D_b$) in the axial direction downstream of the bluff-body and 0.2 m ($4D_b$) in the radial direction, where $D_b = 50$ mm is the diameter of the bluff-body. Similar to the non-swirling case, the axial mean velocity is specified based on the assumption of a fully developed turbulent pipe flow in the jet region while it is interpolated from the experimental data in the co-flow region. In the primary air flow region the mean axial and tangential velocities are assumed to be turbulent fully developed flow and are calculated by the function

$$\tilde{U} = 1.218\, U_B \left(1 - \frac{|y|}{\delta}\right)^n, \tag{4.1}$$

where y is the distance from the center of annulus, $n = 1/7$, and $\delta = 1.01H_a/2$, with H_a being the width of the annulus. The factor of 1.01 is added so that the velocity

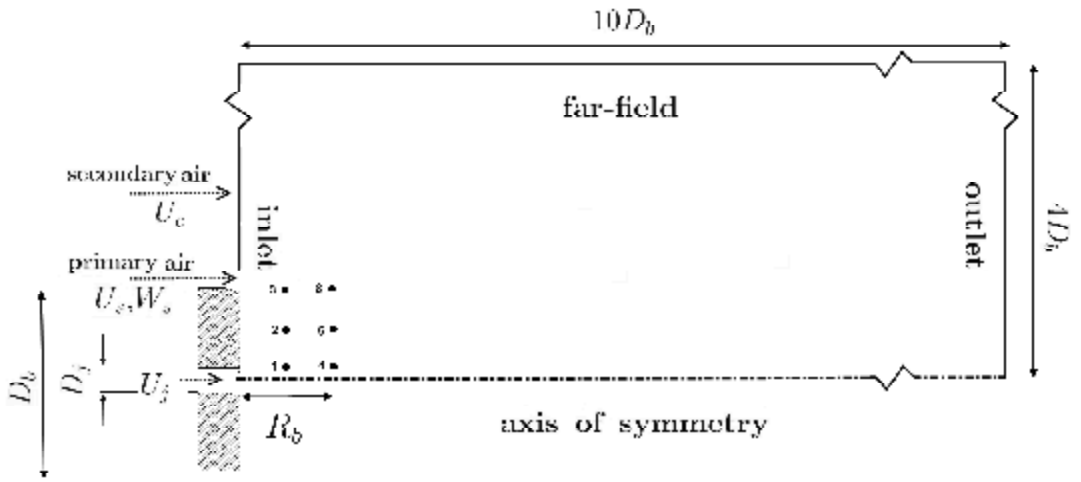


Figure 4.2: Computational domain of the swirling bluff-body flame with boundary conditions. Location of monitor points are shown with respect to the bluff-body base. See also Table 4.2.

gradients are finite at the walls and U_B is equivalent to the bulk velocity of primary air flow.

The axial and radial rms fluctuating velocities (U_{RMS} and W_{RMS}) are interpolated from the experimental data. Following Masri et al. [32], it is assumed that $V_{RMS} = \sqrt{1/2}\, U_{RMS}$ in the jet as well as in the primary and the secondary air streams. The mean turbulent shear stress $\widetilde{uw}$ is interpolated from the experimental measurements while $\widetilde{uv}$ is calculated as

$$\widetilde{uv} = \rho_{12}\sqrt{u^2 v^2}, \tag{4.2}$$

where $\rho_{12} = -0.4$ and $\rho_{12} = 0.5(r/R_j)$ in the co-flow and jet regions, respectively. In the primary air stream it is assumed that $\widetilde{uv} = \widetilde{uw}$. Since the flow is dominated by the large recirculation zones and hence there is no need to resolve the boundary layer, perfect slip and no penetration boundary conditions are applied on the buff-body surface. The symmetry and far field boundary conditions are applied at the

centerline and the outer boundaries, respectively. Pressure is fixed at the atmospheric pressure at the exit plane.

4.4 Results

Calculations have been performed with the SLM velocity model, the JPM turbulent frequency model, the IEM mixing model, and the simple flamelet model for the chemistry. The model constants are the same as specified in Table 2.1.

4.4.1 Statistical stationary solution

To show the statistical stationarity of the numerical solutions, time series of Favre-averaged mean axial velocity and turbulent kinetic energy are monitored at six probe locations as specified in Table 4.2. Figure 4.3 depicts the time histories of mean axial velocity and turbulent kinetic energy at these probe points. The results are obtained using a 144×144 grid and the number of particles per cell N_{pc}= 50. It can be seen that a statistical stationary solution is obtained after about 7000 particle time steps.

Table 4.2: The coordinates of the probe points for monitoring convergence history.

Coordinates	1	2	3	4	5	6
x	$D_b/4$	$D_b/4$	$D_b/4$	$D_b/2$	$D_b/2$	$D_b/2$
r	R_j	$R_b/2$	R_b	R_j	$R_b/2$	R_b

4.4.2 Grid convergence

Extensive simulations are performed to demonstrate grid convergence. For this purpose the computational grid is refined from 96×96 up to 216×216. All the simulations are performed with the number of particles per cell $N_{pc} = 50$ and the time-averaging factor $N_{TA} = 500$. The time-averaged profiles of mean and rms axial

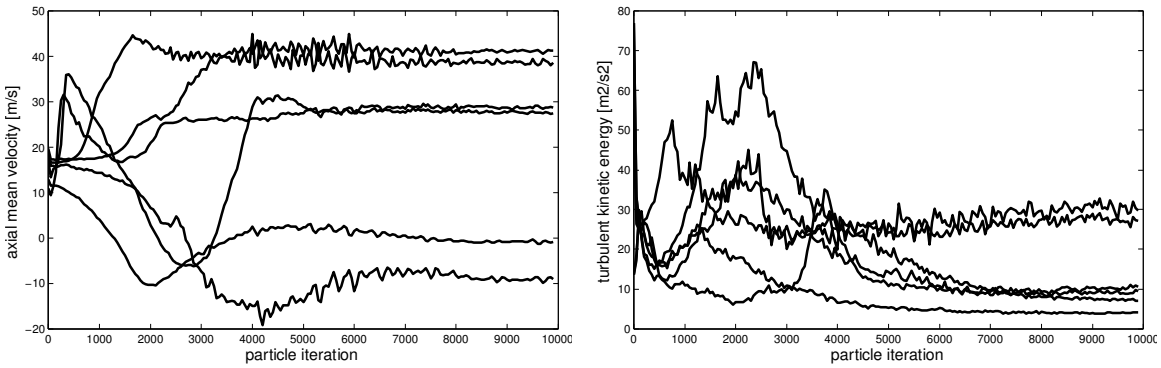


Figure 4.3: Time series of Favre-averaged mean axial velocity and turbulent kinetic energy at the probe points.

and tangential velocities, and mean and rms mixture fractions at the axial location $x/D_b = 0.8$ are shown for three different grids in Fig. 4.5. More results for grid convergence are presented in Appendix A. As seen in these figures, the grid convergence is achieved for the 144×144 grid. In the next section the computational results using 144×144 grid are compared with the experimental data and the earlier PDF simulations of De Meester et al. [8]

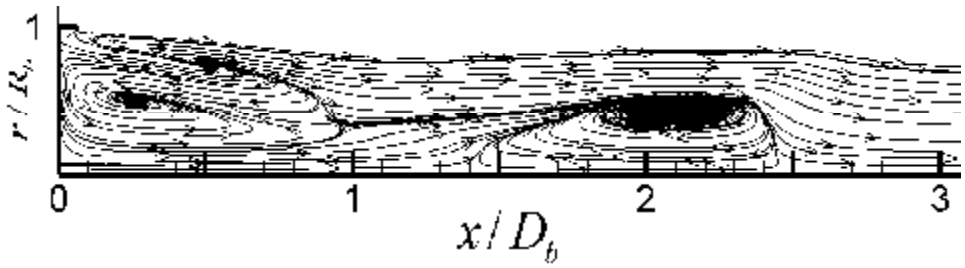


Figure 4.4: The streamlines of the mean velocity computed for the swirling bluff-body flame in the vicinity of the recirculation zones.

4.4.3 Comparison with the earlier PDF simulations and the experimental Data

The results are now compared with the experimental data [75] as well as with the earlier scalar PDF simulations of De Meester et al. [8]. Figure 4.4 depicts the streamlines

of mean velocity in the recirculation region behind the bluff-body. The streamlines show a typical flow feature of a swirling flow past a bluff-body. Two recirculation regions are captured correctly by the simulations. The first one is induced by the circular bluff-body in toroidial shape immediately behind the bluff-body base. The second recirculation is induced by the swirl and a vortex breakdown bubble (VBB) is observed around the centerline. The presence of the second RZ coexists with occurrence of a highly rotating collar-like flow feature. Such collar-like features vary in size and rate of rotation and occur at the axial locations where the flow narrows to form a necking zone. Two recirculation regions are also observed in the experiment [22]. The upstream RZ has two vortices. The center of the first one is located at $x/D_b \approx 0.25$ and the second one is at $x/D_b \approx 0.5$ that extends up to $x/D_b \approx 1.0$. The VBB is located between $x/D_b \approx 1.4$ and $x/D_b \approx 2.4$. Experimental observations indicate that the first RZ extends up to $x/D_b \approx 1.0$ and the second RZ starts at about $x/D_b \approx 1.3$ and extends up to about $x/D_b \approx 2.2$ [22] which shows that our results are in good agreement with the measurements. Figures 4.6–4.7 show the computed radial profiles of mean axial and tangential velocities compared with the experimental data [75] and the PDF simulation of De Meester et al. [8]. It can be seen that there is good agreement between present simulations and the experimental data. In spite of some discrepancies especially at axial location of $x/D_b = 0.8$, the present results are overall in reasonable agreement with the results of De Meester et al. [8]. From the simulations, it can be observed that along the centerline, the fuel jet undergoes a strong deceleration before it stagnates around the axial position $x/D_b \approx 1.4$ where the second RZ starts. Negative axial velocity shows the toroidal, dome-shaped primary recirculation zone which stagnates at about $x/D_b \approx 1.0$ downstream of the bluff-body face where the first RZ ends. The maximum rotational velocity at the axial locations between the upstream and downstream recirculation zones exceeds even that found at the exit of the swirling annulus.

Figures 4.8–4.9 show the computed radial profiles of rms axial and tangential velocities compared with the experimental data. Note that the rms velocities are not reported in the paper of De Meester et al. [8]. It is shown that except in the axial locations of $x/D_b = 0.0136$ and 0.4 the rms velocities are in good agreement with the experiment measurements. Figures 4.10–4.11 show the computed radial profiles of the mean and rms mixture fraction compared with the experimental data and the PDF simulations of De Meester et al. [8]. It is found that except in the axial location of $x/D_b = 0.8$ the mean mixture fraction profiles are in good agreement with the experimental data and also with the results of De Meester et al. [8]. It is also observed that at the most of the axial locations the present rms mixture fraction results are predicted better than the results of De Meester et al. [8].

4.5 Summary

In this chapter the robustness of the new hybrid algorithm is demonstrated for the complicated Sydney swirling flame. For this purpose the 'SM1' flame is selected as a test case since it exhibits the least jet precessing. For this simulation the simplified Langevin model (SLM) for velocity, modified Jayesh-Pope model (JPM) for turbulent frequency and IEM model for mixing are employed. A simple flamelet model is used as the chemistry model. The new hybrid algorithm is found to be very robust for this difficult test case. Additionally it is very successful in capturing two recirculation zones observed in the experiments [1, 22]. In spite of the most simple models used for velocity and chemistry, the results have been found to be in reasonable agreement with the experimental data as well as the PDF simulations of De Meester et al. [8].

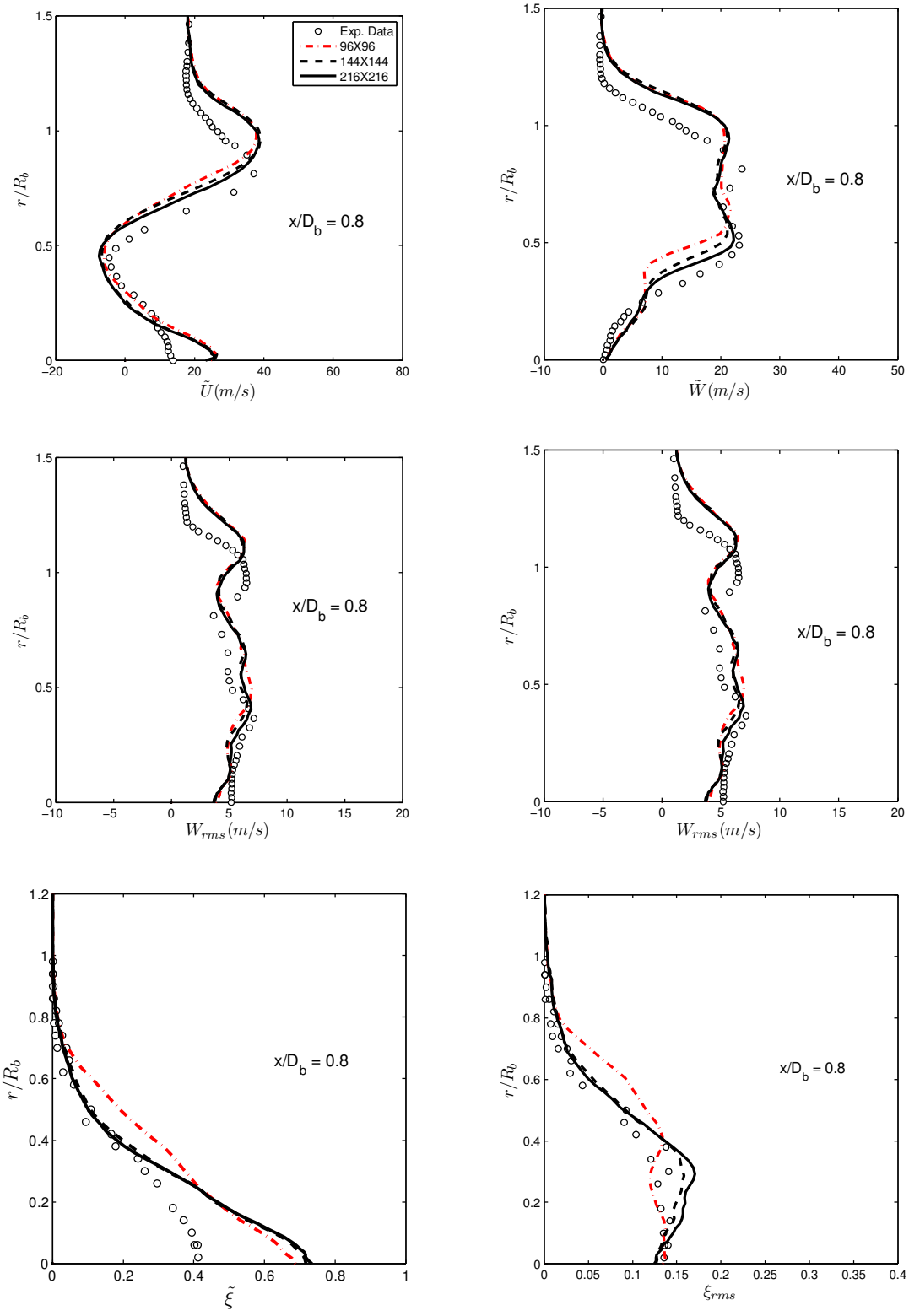


Figure 4.5: Grid convergence: the radial profiles of mean and rms fluctuating axial and radial velocities, mean and rms mixture fraction at axial location $x/D_b = 0.8$. Computations are performed using 96×96, 144×144 and 216×216 grids.

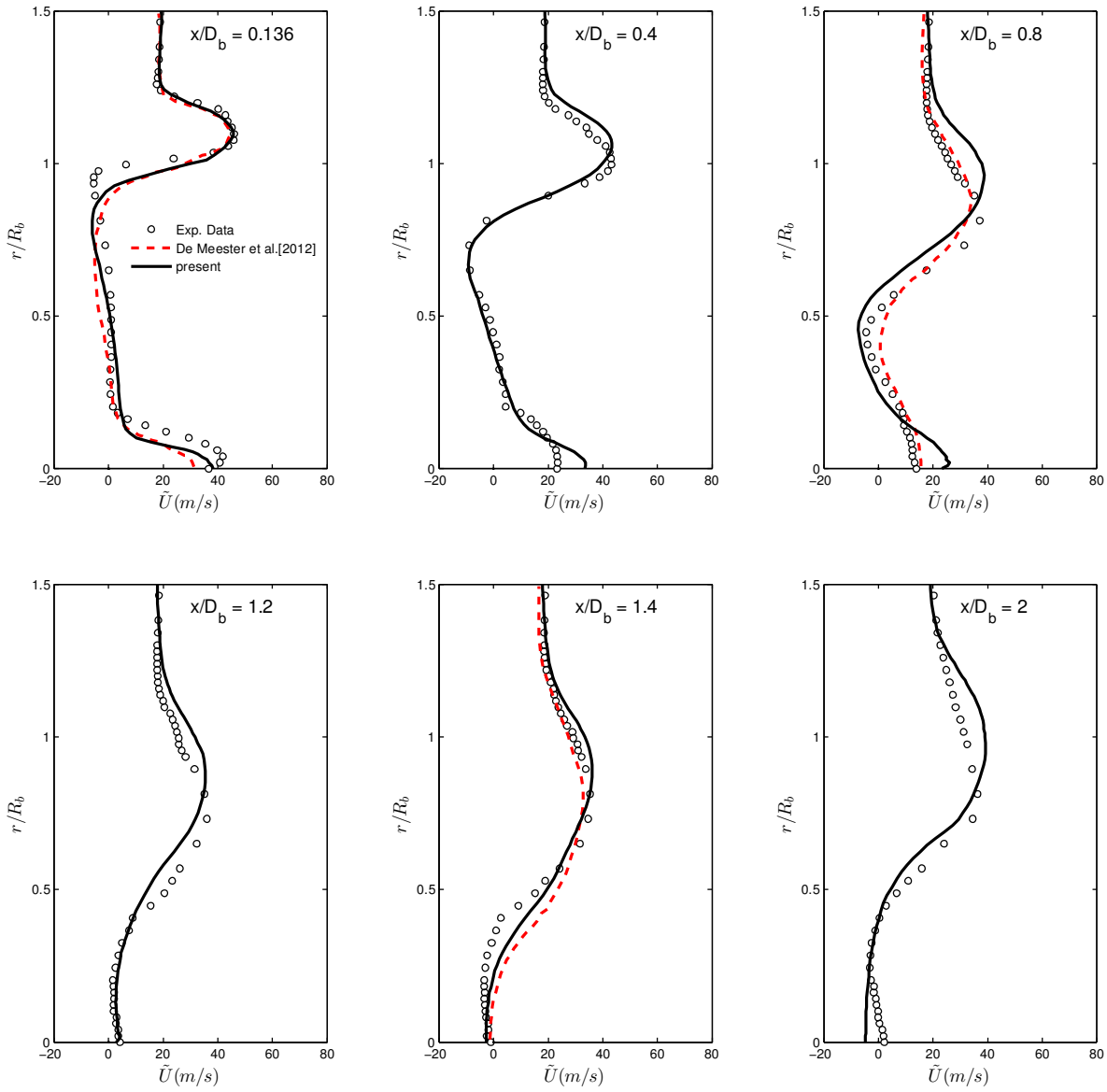


Figure 4.6: The radial profiles of mean axial velocity compared with the experimental data [75] and the numerical results of De Meester et al. [8].

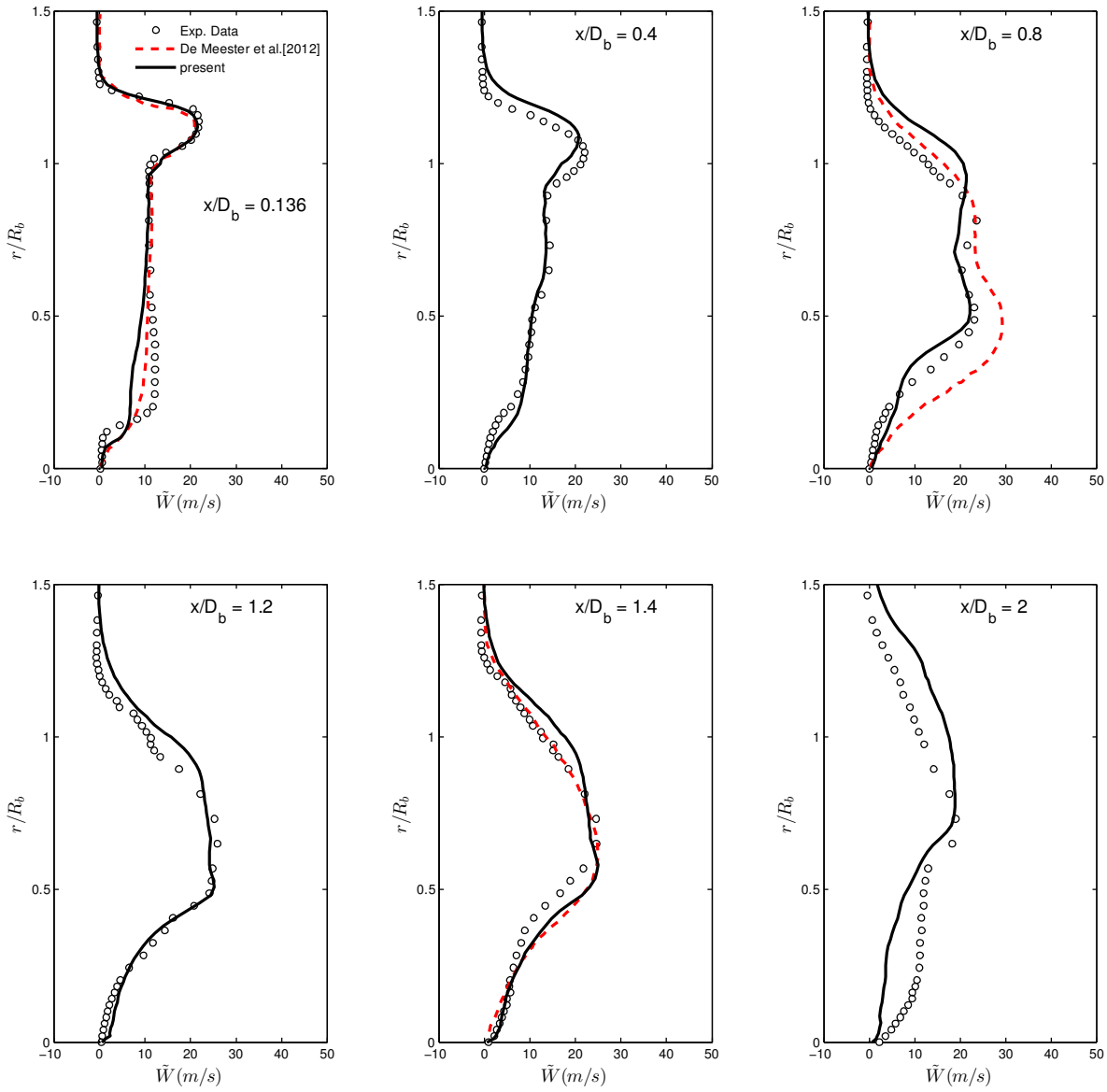


Figure 4.7: The radial profiles of mean tangential velocity compared with the experimental data [75] and the numerical results of De Meester et al. [8].

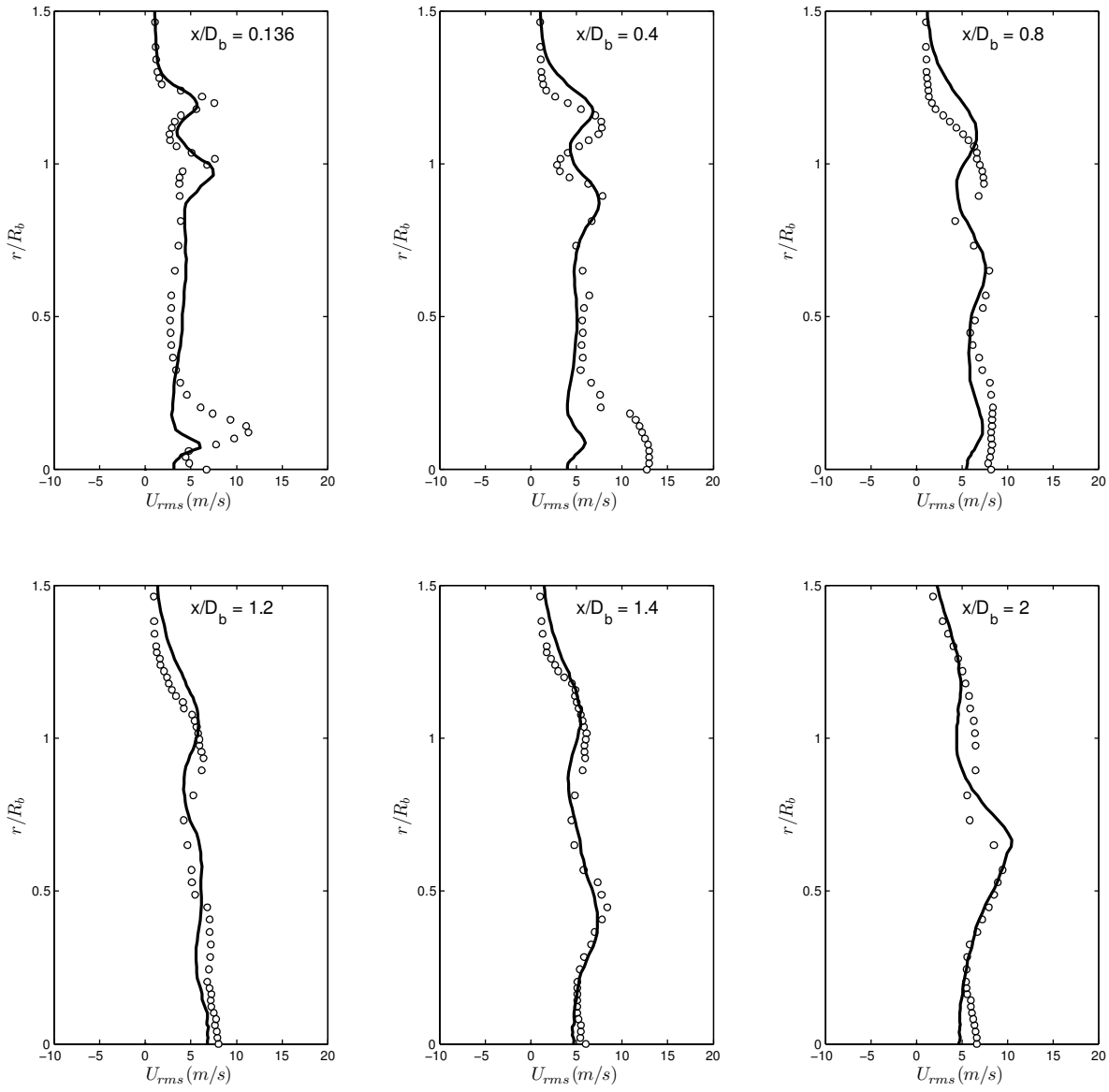


Figure 4.8: The radial profiles of rms axial velocity compared with the experimental data [75].

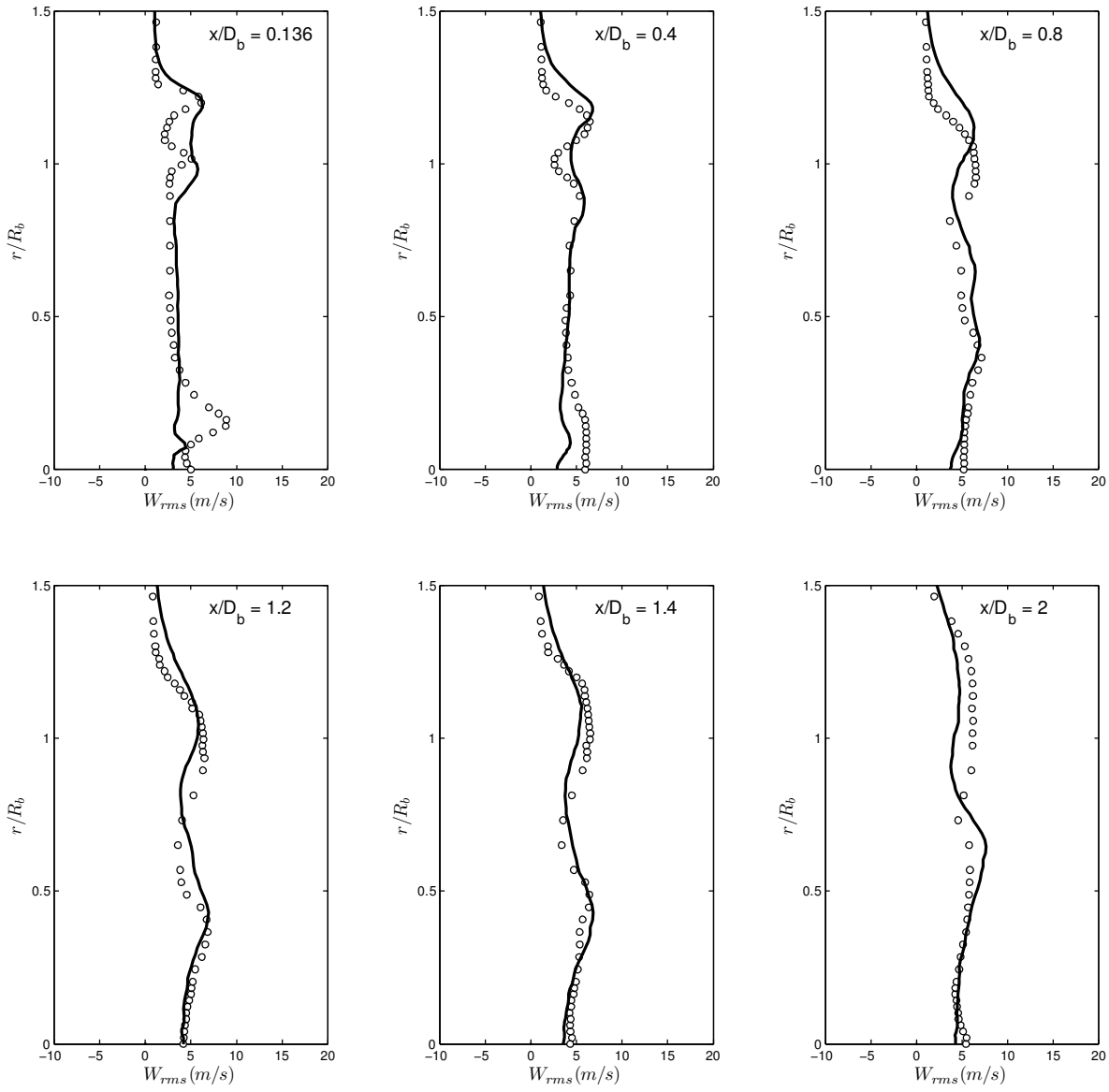


Figure 4.9: The radial profiles of rms tangential velocity compared with the experimental data [75].

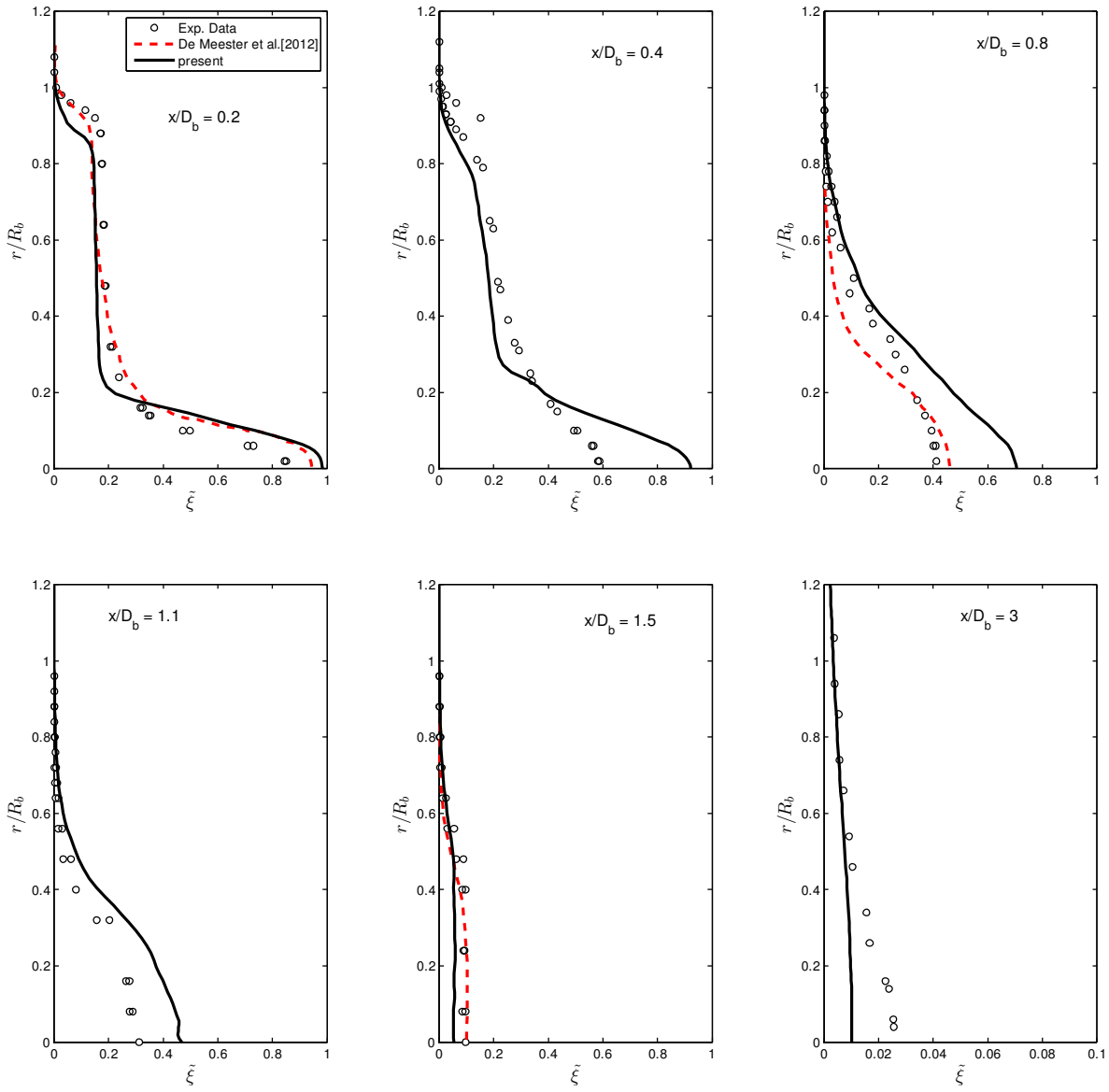


Figure 4.10: The radial profiles of mean mixture fraction compared with the experimental data [75] and the numerical results of De Meester et al. [8].

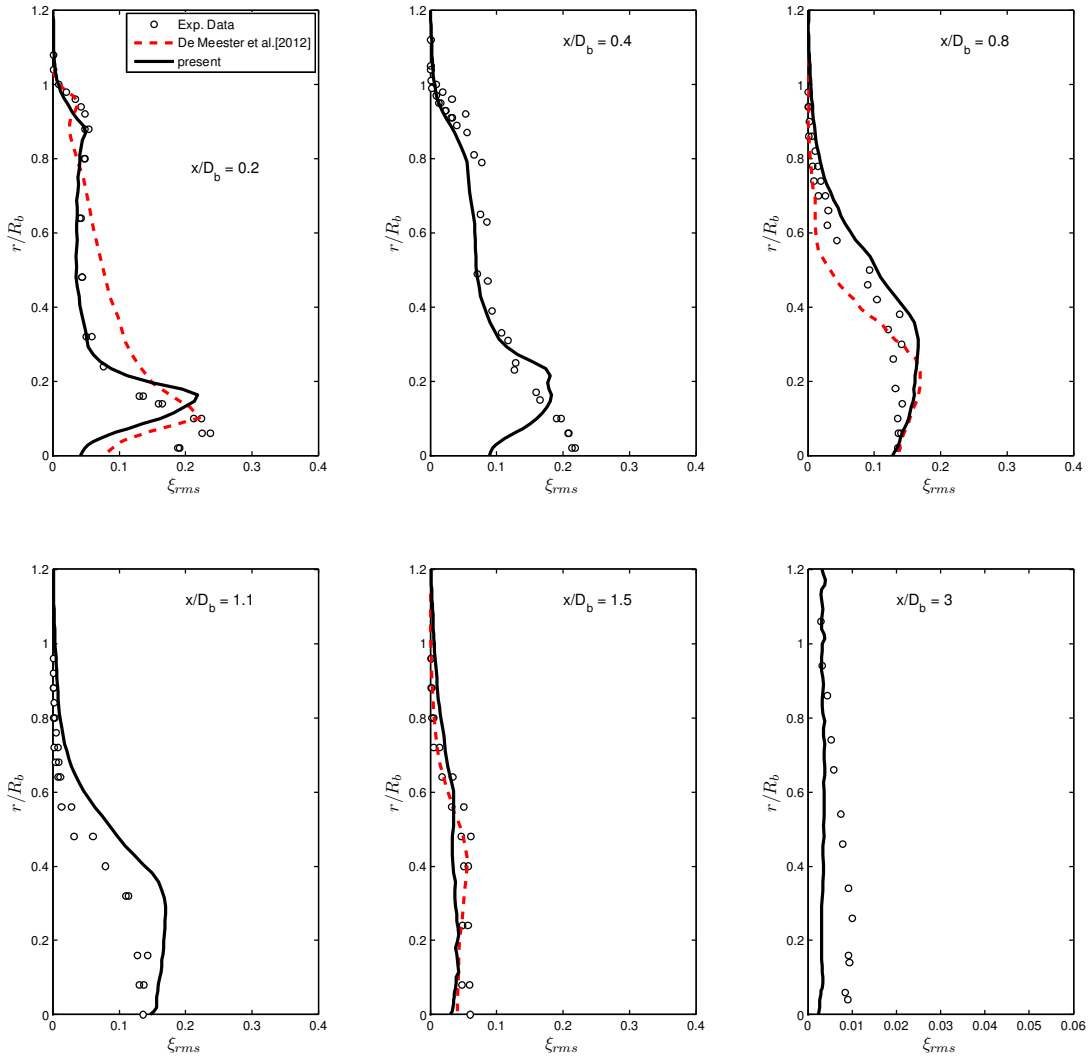


Figure 4.11: The radial profiles of rms mixture fraction compared with the experimental data [75] and the numerical results of De Meester et al. [8].

Chapter 5

Detailed Chemistry Calculations with ISAT

5.1 Introduction

The chemistry has been described using a simple flamelet model in the previous chapters. The flamelet approach is a extension of the flame sheet model which assumes that chemical reactions take place infinitely fast such that the reaction zone is an infinitely thin layer. Assuming the equal diffusivity of all compositions under constant pressure combustion without heat loss, the thermo-chemical properties are determined completely by the local mixing state. The flamelet approach relaxes the infinitely fast chemistry assumption by introducing the scalar dissipation rate as a parameter to describe the degree of departure from the equilibrium state. Nevertheless, the flamelet model still relies on the assumption that the time scales for chemical kinetics are much shorter than the convection and diffusion time scales. Under this condition of widely separated time scales, the combustion takes place within asymptotically thin layers embedded in the turbulent flow in a quasi-steady state and thus adjusts immediately to local flow conditions. Each layer can be viewed as a laminar

flame and called as flamelet. The greatest feature of the flamelet approach is that the instantaneous thermochemical state of the mixture is related to a conserved scalar known as mixture fraction. The main advantage of the flamelet model is that the chemistry can be preprocessed and tabulated so that only the mixing problem needs to be solved in actual flame simulations. Then the thermodynamic state (temperature, density and compositions) is simply obtained through a simple look up operation using the instantaneous mixture fraction, which saves tremendous computational time. Although flamelet-based models have been successfully used to model a wide range of laboratory scale and industrial turbulent flames [44], they fail to provide sufficient description of chemical kinetics when the chemical time scales are comparable to the convective and diffusive times scales so that there are significant turbulence-chemistry interactions in the flame zone. In particular, the key processes of local extinction and re-ignition that are responsible for flame stability, emission and blow off occur due to strong interactions between turbulence and finite-rate chemical kinetics. Therefore the finite-rate detailed chemistry models are of crucial importance for accurate modeling of combustion systems where strong turbulence-chemistry interactions occur.

The detailed description of combustion chemistry typically involves tens of species, hundreds of reactions, and timescales from 10^{-9} s to 1 s. The computational cost of making calculations for turbulent flames including detailed chemistry is usually deemed to be prohibitive due to the stiffness problem caused by the large disparity in chemical time scales. To overcome this difficulty, several approaches have been proposed. The first approach is to use the flamelet-based models which substantially reduces computational cost but fails to describe chemical kinetics when there are significant turbulence-chemistry interactions as discussed above. The second method is to simplify the chemical reaction mechanism using various approaches. Dimension reduction techniques can be used to obtain a wide range of reduced mechanisms from skeletal mechanisms involving a few species and reactions to augmented reduced

mechanisms involving tens of species and reactions. Reduces mechanisms compromise between level of description and computational cost. The intrinsic low-dimensional manifolds (ILDM) developed by Maas and Pope [28, 27, 26] is a commonly used dimension reduction technique that aims to reduce the chemical state space globally by means of an eigenvector analysis to identify locally the fastest time scales of the chemical system. Another commonly used approach is the computational singular perturbation (CSP). In this approach, the chemical reactions are grouped into characteristic time scales to effectively reduce dimensionality of the chemical mechanism. It should be noted that the time scale grouping process for CSP is entirely mathematical and no prior knowledge of any optimal parameters or assumption for the particular mechanism is required. By making five such groupings (two fast, two moderate and one slow), Lam and Goussis [23] showed that an accurate representation of the hydrogen-air reactive system for a wide range of conditions can be made. ILDM and CSP are similar in many aspects, particularly the local determination of the fastest chemical time scales by means of basis vectors. The main distinguishing characteristics between the two are that CSP has the ability to reduce the computational stiffness of a mechanism and can categorize a mechanism with a reduced number of variables or groupings (whilst the governing equation system remains large), the ILDM method can also reduce the mechanism stiffness and in addition to reduction of the dimension of the system the governing equations of the system are also reduced.

Although dimension reduction techniques are effective in reducing the dimensionality of the chemical kinetic equations significantly, the reduced mechanisms must still include tens of species and reactions in order to provide a sufficient description of turbulent reacting flows of practical interest. For instance, the augmented reduced mechanism, ARM2, developed by Sung et al. [61] for methane-air combustion based on GRI 2.11 [73] and used in the present simulations involves 19 species and 15 reactions. It is still computationally prohibitive to perform direct integration of the

reduced chemical kinetic equations and further optimization is required to make PDF simulations with a detailed chemistry feasible.

In situ adaptive tabulation (ISAT) method has been developed and proved to reduce the computational cost by up to a factor of 1000 compared to direct integration [53]. The ISAT algorithm is in essence a storage/retrieval technique for the calculation of composition changes due to chemical reaction. In this approach, a look-up table is built on-line or in situ, by doing so the table can be populated with the particular composition space unique to the particular flow being simulated; no prior assumptions of the dimensionality or type of manifold are required for this strategy. The ISAT algorithm is based on the observation that realized compositions of reaction are restricted to a small subset of the composition space called the accessed region. In contrast to the direct integration (DI) of the reaction equation, or a priori table storing the reaction mapping in the whole composition space, the ISAT algorithm builds adaptively an unstructured table of the reaction mapping only for the accessed region. The table is built in the course of the PDF computation, and an in situ data retrieval or DI is performed according to a prescribed error tolerance denoted by ϵ_{tol}. The ISAT algorithm is incorporated into the present hybrid finite-volume/particle method to efficiently perform PDF simulations with a detailed finite-rate chemistry model.

For a given thermo-chemical state of a system $\mathbf{\Phi}(t_0)$ and a prescribed time step Δt, the thermo-chemical composition at $t_0 + \Delta t$ is calculated to obtain $\mathbf{\Phi}(t_0 + \Delta t)$. To determine $\mathbf{\Phi}(t_0 + \Delta t)$ within a specified error tolerance ϵ_{tol}, ISAT utilizes a number of strategies including direct integration (DI), primary retrieve, secondary retrieve, grow and add. The fundamental quantity stored and retrieved in ISAT is reaction mapping $\mathbf{R}(\mathbf{\Phi}(t_0))$, which is defined to be the solution to the reaction equation

$$\frac{d\mathbf{\Phi}}{dt} = S(\mathbf{\Phi}(t)), \tag{5.1}$$

over the time step Δt from the initial condition $\mathbf{\Phi}(t_0)$. This is the quantity needed to integrate the chemical kinetic equations [71]. When a simulation is started, ISAT begins to build a table that stores the solution to the direct integration of the chemical source terms. A table entry in the ISAT consists of the initial composition vector $\mathbf{\Phi}(t_0)$, the mapping $\mathbf{R}(\mathbf{\Phi}(t_0))$, the mapping gradient $\mathbf{A}(\mathbf{\Phi}(t_0))$ and the specification of the ellipsoid of accuracy (EOA) defined as a hyper-ellipsoid centered at $\mathbf{\Phi}(t_0)$. For any $\mathbf{\Phi}(t_0 + \Delta t)$, the linear approximation to the mapping is

$$\mathbf{R}(\mathbf{\Phi}(t_0 + \Delta t)) = \mathbf{R}(\mathbf{\Phi}(t_0)) + \mathbf{A}(\mathbf{\Phi}(t_0))(\mathbf{\Phi}(t_0 + \Delta t) - \mathbf{\Phi}(t_0)). \tag{5.2}$$

By definition, the EOA is the region around $\mathbf{\Phi}(t_0)$ in which the normalized error is less than the specified error tolerance ϵ_{tol} in this approximation. If $\mathbf{\Phi}(t_0 + \Delta t)$ is within the EOA at $\mathbf{\Phi}(t_0)$, then $\mathbf{R}(\mathbf{\Phi}(t_0 + \Delta t))$ is retrieved using the linear approximation according to Eq. 5.2. Otherwise direct integration (DI) is performed to obtain $\mathbf{R}(\mathbf{\Phi}(t_0 + \Delta t))$, and also the error between this new mapping and the approximate mapping is measured. If the error is smaller than ϵ_{tol}, the EOA is grown and $\mathbf{R}(\mathbf{\Phi}(t_0 + \Delta t))$ is returned; otherwise a new record is generated based on $\mathbf{\Phi}(t_0 + \Delta t)$. The details of the ISAT algorithm can be found in [53].

The ISAT algorithm has been implemented in the software package [46], ISAT-CK7, which has been incorporated into the present hybrid finite-volume/particle method to efficiently perform PDF simulations using finite-rate detailed chemistry models. The ARM2 mechanism is employed as the chemical kinetic model for all the simulations presented in this thesis. The present hybrid method coupled with ISAT-CK7 is first applied to the non-swirling bluff-body flame 'HM1' and the results are compared with the earlier PDF simulations of Liu et al. [25]. Then the method is applied to study finite-rate chemistry effects for the swirling bluff-body flame and

the results are compared with the experimental data [75] as well as with the scalar PDF simulations of De Meester et al. [8].

5.2 Non-Swirling Bluff-Body Stabilized Flame

The hybrid algorithm has been applied to a bluff-body flame 'HM1E' using the simple flamelet model in Chapter 3. In this chapter, the ISAT package is incorporated into the hybrid algorithm and then applied to another bluff-body flame 'HM1' using the finite-rate chemistry model ARM2 [61]. The flame 'HM1' is selected as a test case since the detailed measurements of compositions have been made for this flame and it has been previously studied by Liu et al. [25] using the old hybrid algorithm. The inlet boundary conditions for flame 'HM1' are slightly different from 'HM1E' flame as specified in Table 5.1.

Table 5.1: Flow parameters of the case 'HM1'.

case	fuel	$U_c(m/s)$	$U_j(m/s)$	$T_{in}(K)$	ξ_{st}
'HM1'	CH4:H2(1:1)	40	118	298	0.05

In this table, U_c is the velocity of coflowing air, U_j is the velocity of the fuel jet, T_{in} is the temperature of fuel at jet exit plane, and ξ_{st} is the stoichiometric mixture fraction. It is emphasized here that the only difference between 'HM1' and 'HM1E' flames is the bulk velocities of jet and co-flow. Note that U_j and U_c were 108 and 35 m/s, respectively in the flame 'HM1E'.

5.2.1 Results

The hybrid FV/Monte Carlo particle method coupled with the ISAT algorithm is applied to the non-swirling bluff-body flame 'HM1'. The submodels are the same as those used in the flamelet calculations except for the mixing and chemistry models. The EMST [60] and the ARM2 [61] methane oxidation mechanism are used as the

mixing and chemistry models, respectively. The EMST mixing model is preferred here since it outperforms the IEM model especially for the flames where significant local extinction and re-ignition occur due to strong chemistry-turbulence interactions [71]. The most significant feature of the EMST model is that mixing occurs locally in composition space. This is the property that neither the IEM model [9] nor the modified Curl's model [19] satisfies. Localness in composition space is achieved in the EMST model by allowing mixing to occur between particles that are connected by the edges of Euclidean minimum spanning tree in the composition space. The advantage of mixing occurring locally in composition space has been demonstrated by Norris and Pope [42] for a diffusion flame test case and by Xu and Pope [71] for the piloted jet flames. An augmented reduce mechanism of 19 species and 15 reaction steps, ARM2 developed by Sung et al. [61] from the GRI2.11 [73] mechanism (with 276 reactions of 49 species) is used in the present simulations. Some details about the ARM2 mechanism can be found in Appendix C. In joint PDF calculations it is possible to implement an accurate detailed mechanism, such as the GRI2.11. However, the augmented reduced mechanisms such as ARM2 are more attractive for turbulent combustion simulations because they are considerably less expensive compared with GRI2.11 while they provide sufficiently accurate description of chemical kinetics as discussed by Pope [53] and Liu et al. [25]. The ISAT algorithm is used to integrate chemical kinetic equations. The accuracy of the ISAT algorithm depends on a specified ISAT absolute error tolerance which controls the error in the tabulation and the error in retrieving from the ISAT table. Following Liu et al. [25] the ISAT error tolerance is taken as $\epsilon_{\text{tol}} = 10^{-4}$. The boundary conditions are same as the flamelet calculations except for the jet and coflow bulk velocities as mentioned before. The computational domain is also the same as that used in the flamelet calculations. All simulations are performed using a 96×96 grid.

The new hybrid FV/particle method coupled with ISAT-CK7 package is used to simulate the non-swirling bluff-body flame 'HM1'. All calculations are performed using EMST mixing model [60] and ARM2 methane oxidation mechanism [61]. To accelerate computations and guarantee the ignition, the computations are first performed using the flamelet model and then these results are used as the initial conditions for detailed chemistry calculations. Thus the computational cost is decreased substantially. The present results are compared with the experimental data available on-line [75] and also with the earlier PDF simulations of Liu et al. [25].

Mean velocity fields:

Calculations have been performed with the SLM model for velocity, the modified Jayesh-Pope model (JPM) for turbulent frequency, and the Euclidean minimum spanning tree (EMST) [60] model for mixing. The computed velocity fields from the joint PDF calculations are compared with the experimental data [75] obtained for the flame 'HM1E' as recommended by the experimentalist [3]. The wind tunnel at University of Sydney was unable to generate a uniform 40 m/s coflow; maximum was 35 m/s [75]. The jet velocity was accordingly reduced (from 118 m/s to 108 m/s) so that both 'HM1' and 'HM1E' are at the same proportion from the blow-off [75].

The radial profiles of the time-averaged mean axial $\tilde{U}$ and radial $\tilde{V}$ velocities with the experimental data are shown in Figs 5.1 and 5.2, respectively. In spite of slight differences in the jet and co-flow bulk velocities between the experiment and computations, there is reasonable agreement between the PDF results and the experimental data. In the flamelet calculations of the bluff-body flame presented in Chapter 3, we have simulated 'HM1E' flame and discussed the flow field structure extensively. It is found here that the structure of the flame 'HM1' is very similar to 'HM1E'. There is a recirculation zone behind the bluff-body. The recirculation zone extends up to $x/D_b = 1.65$ similar to 'HM1E' flame. It has been observed that there

is no much difference between the flamelet and detailed chemistry calculations for the mean velocity field.

Mean composition fields:

The radial profiles of the mean mixture fraction are shown in Fig. 3.17 at six axial locations i.e., x/D_b =0.26, 0.6, 0.9, 1.3, 1.8, and 2.4. Here, the mixture fraction, ξ is calculated by mass fraction of products using the Bilger's formula [4](see Eq. (2.30)). It can be seen in Fig. 5.3 that the present results are over all in good agreement with the experimental data and also with the computational results of Liu et al. [25]. The discrepancy between the present results and the experimental data increases in axial location $x/D_b = 2.4$ where the mixture fraction is close to the stoichiometric mixture fraction. The radial profiles of the mean mass fractions of H2O are shown in Fig. 5.4. The numerical results are compared with the experimental data. Note that the mass fraction of H2O was not reported in Liu et al. [25]. It can be seen that the results are in good agreement with the experimental data. Figures 5.5–5.7 show the profiles of the mean mass fractions of CO2, CO, and N2 compared with the experimental data and with the numerical results of Liu et al. [25]. There is reasonable agreement between the present results and the experimental data for the mass fractions of CO2, CO, and N2 in most of the sections except for $x/D_b = 2.4$ where the mass fractions are over predicted near the axis. The radial profiles of the mean temperature are shown in Fig. 5.8. The major discrepancies occur behind the bluff-body at section $x/D_b = 0.26$ where the mean temperature is over predicted.

Scatter plots:

In this section, the computed scatter plots of different composition variables against mixture fraction are compared with the measured scatter plots and also with the flamelet calculations. Figures 5.9–5.14 show the scatter plots of the mass fractions of

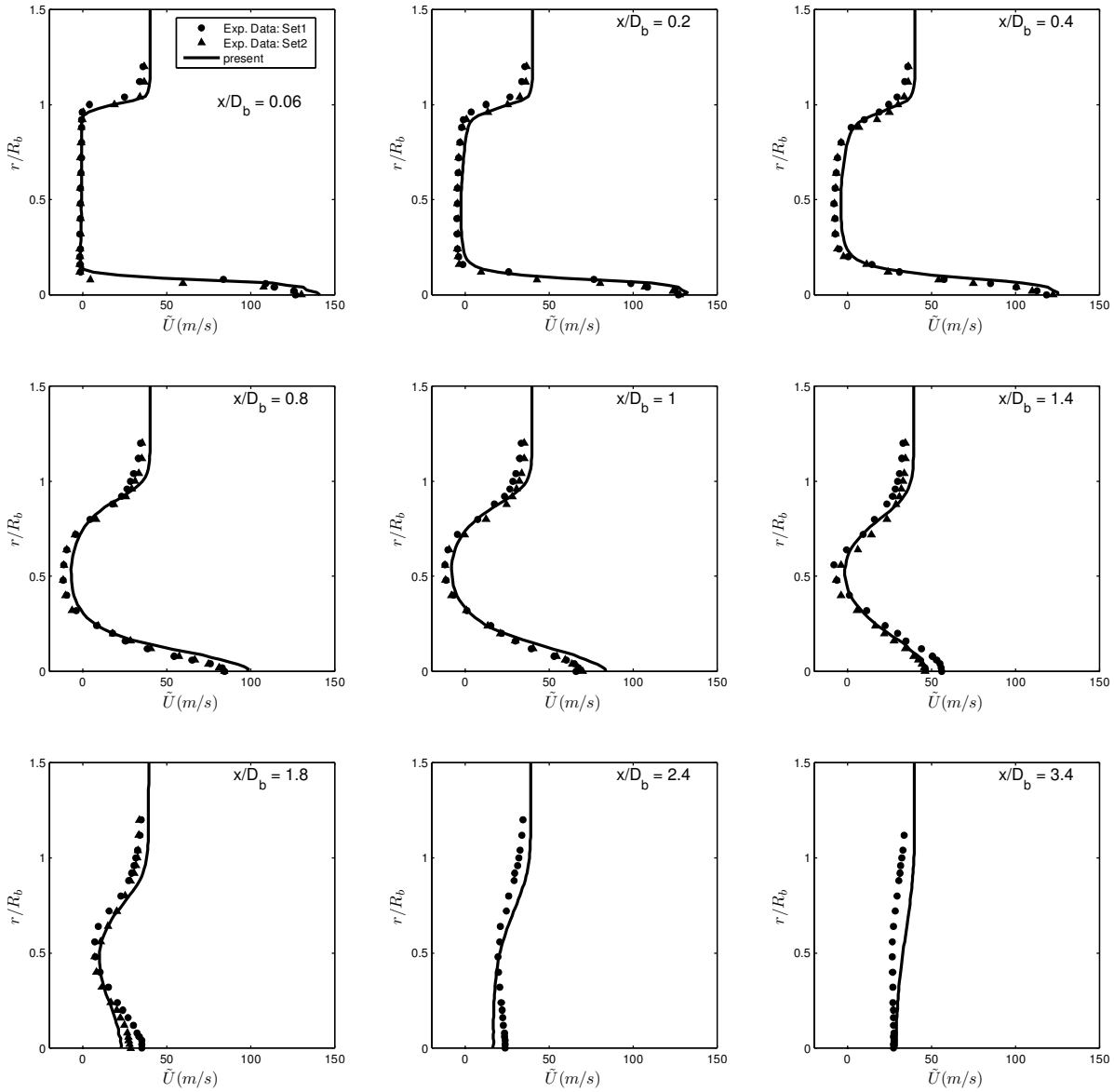


Figure 5.1: The detailed chemistry computations of the bluff-body flame 'HM1' using the ARM2 mechanism. The radial profiles of mean axial velocity compared with the experimental data [75]

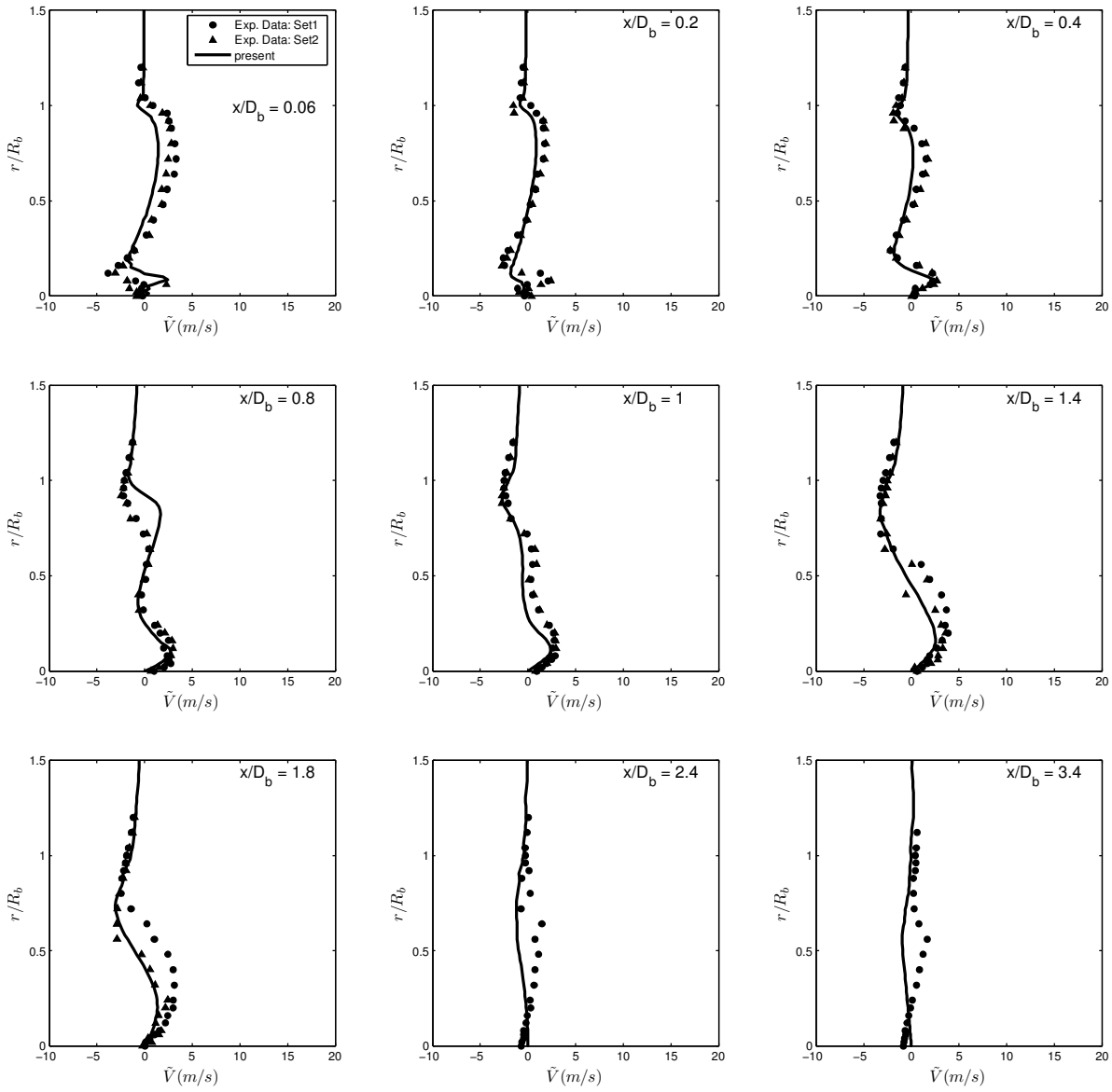


Figure 5.2: The detailed chemistry computations of the bluff-body flame 'HM1' using the ARM2 mechanism. The radial profiles of mean radial velocity compared with experimental data [75].

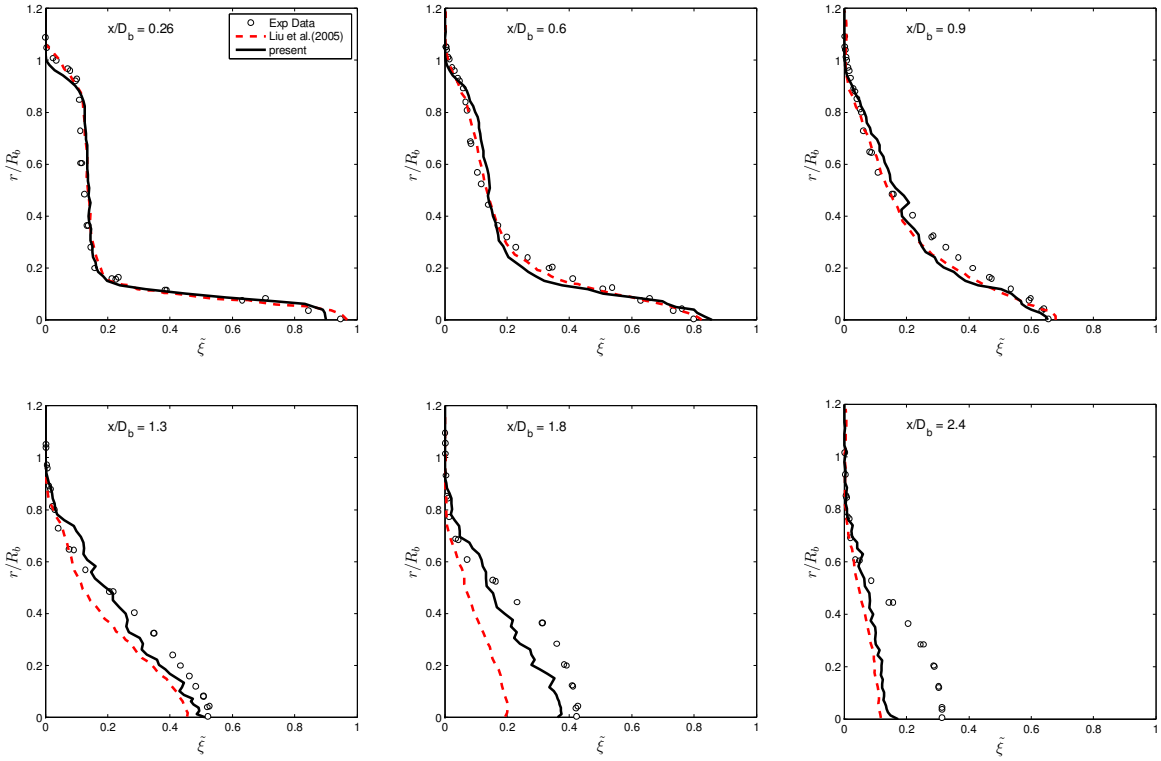


Figure 5.3: The detailed chemistry computations of the bluff-body flame 'HM1' using the ARM2 mechanism. The radial profiles of the mean mixture fraction compared with the experimental data [75].

species CO, CO2, H2O, OH, and O2 against the mixture fraction at the axial locations $x/D_b = 0.6$, 1.3, and 1.8. The scatter plots are made using the the particles with radial locations of $r/R_b < 0.92$. It can be seen that the data bands (the data range at a given mixture fraction) in the joint PDF calculations are narrower than those of the experimental data, which is consistent with the previous observations of Liu et al. [25]. These data bands become wider near the stoichiometric mixture fraction. In Figs. 5.10, 5.12, and 5.14 the temperature scatter plots are shown against the mixture fraction at the axial locations $x/D_b = 0.6$, 1.3, and 1.8. The computed data bands in scatter plots of temperature are again narrower than the experimental data. This is also consistent with the results of Liu et al. [25]. The local extinction is evident in the experimental data at several radial locations in 'HM1' especially at the axial location

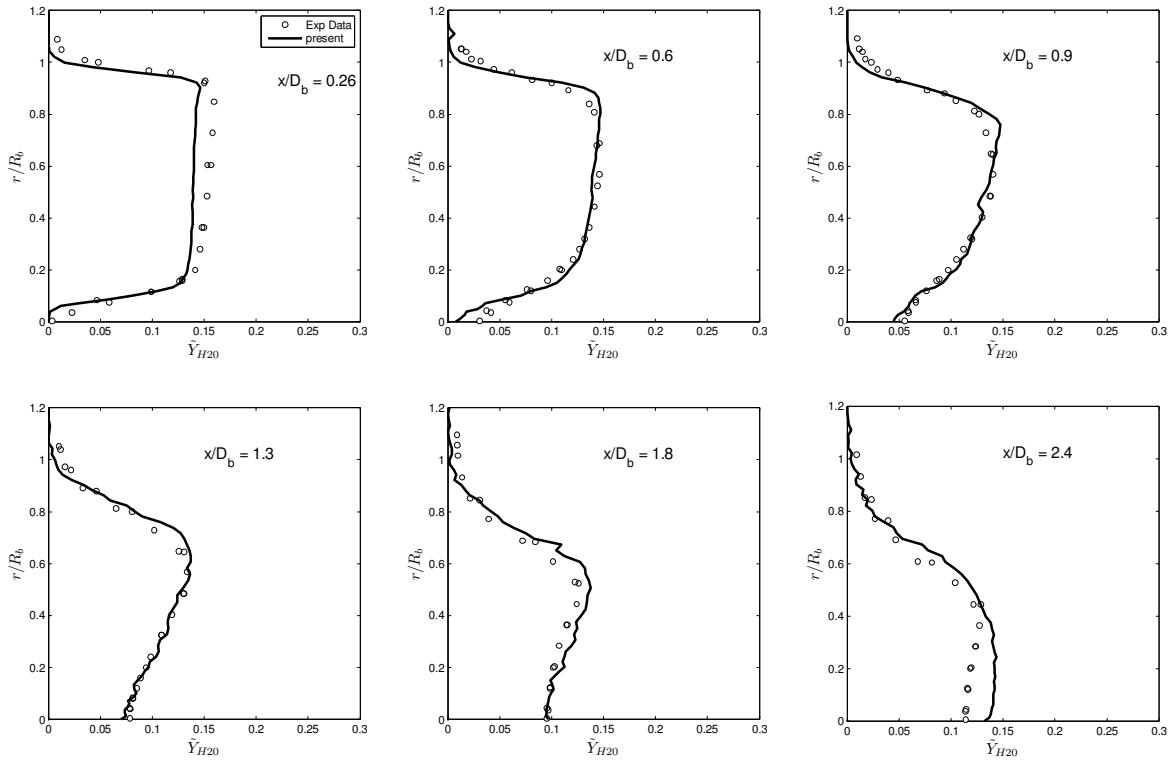


Figure 5.4: The detailed chemistry computations of the bluff-body flame 'HM1' using the ARM2 mechanism. The radial profiles of the mean mass fraction of H2O compared with the experimental data [75].

$x/D_b = 0.6$. But this local extinction is not observed in the current joint PDF calculations and also PDF simulations of Liu et al. [25]. In all of the temperature scatter plots the maximum temperature values obtained by the experimental measurements are greater than the predictions. In Figs. 5.9, 5.11, and 5.13 it is observed that near the stoichiometric mixture fraction, the finite-rate chemistry calculations predict the mass fraction of carbon dioxide (CO2) less than the flamelet model while reversely the mass fraction of carbon monoxide (CO) are estimated greater than the flamelet model. The mass fraction of H2O computed by the finite rate chemistry model is slightly greater than the flamelet model near the stoichiometric mixture fraction but it is about the same at the other mixture fraction values. There are significant discrepancies between scatter plots of OH computed by the finite-rate chemistry model

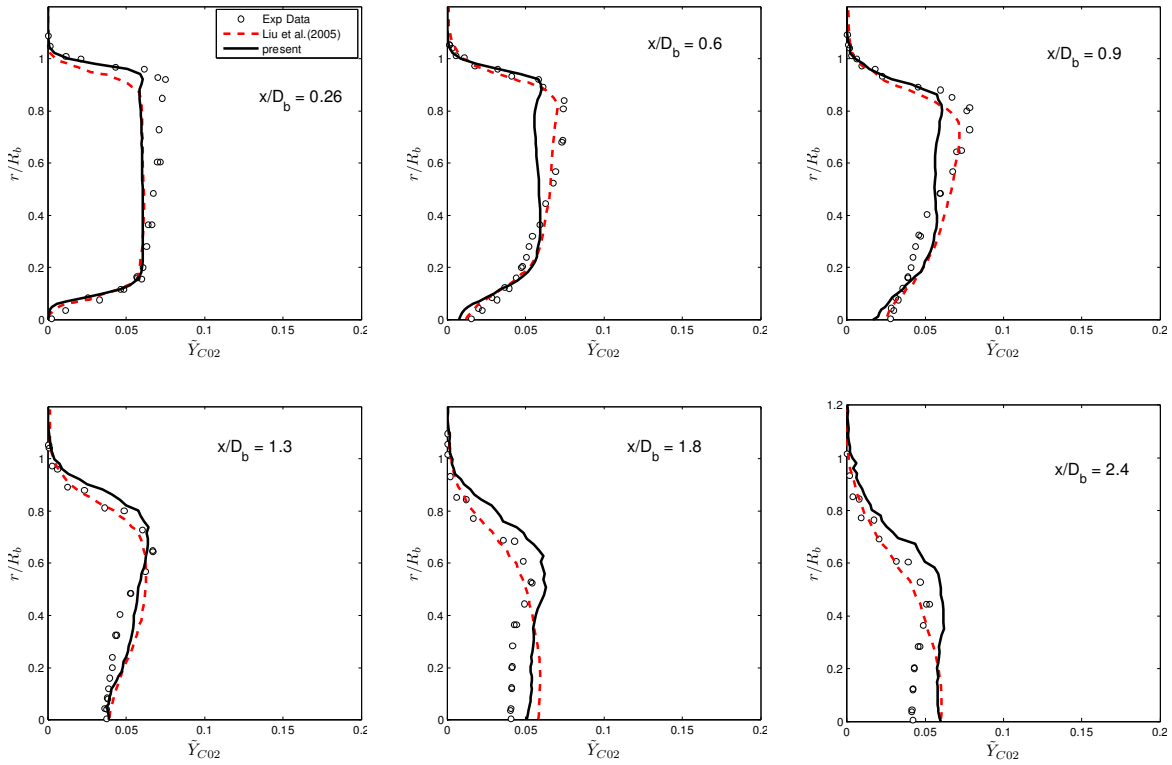


Figure 5.5: The detailed chemistry computations of the bluff-body flame 'HM1' using the ARM2 mechanism. The radial profiles of the mean mass fraction of CO2 compared with the experimental data and with the previous numerical simulations of Liu et al. [25].

(ARM2) and with flamlet model as well as with the experimental measurements. Considering the low values of mass fractions of OH with respect to the other species, e.g., CO, this may be improved by taking smaller values for the ISAT error tolerance. But reducing the ISAT error tolerance increases the computational time of simulations significantly.

5.3 Swirl-Stabilized Bluff-Body Flame 'SM1'

In Chapter 4, the JPDF simulations of the Sydney swirl-stabilized bluff-body flame 'SM1' studied experimentally by Al-Abdeli and Masri [1, 2], Kalt et al. [22], and Masri et al. [31] were performed using a simple flamelet model. In this chapter, the

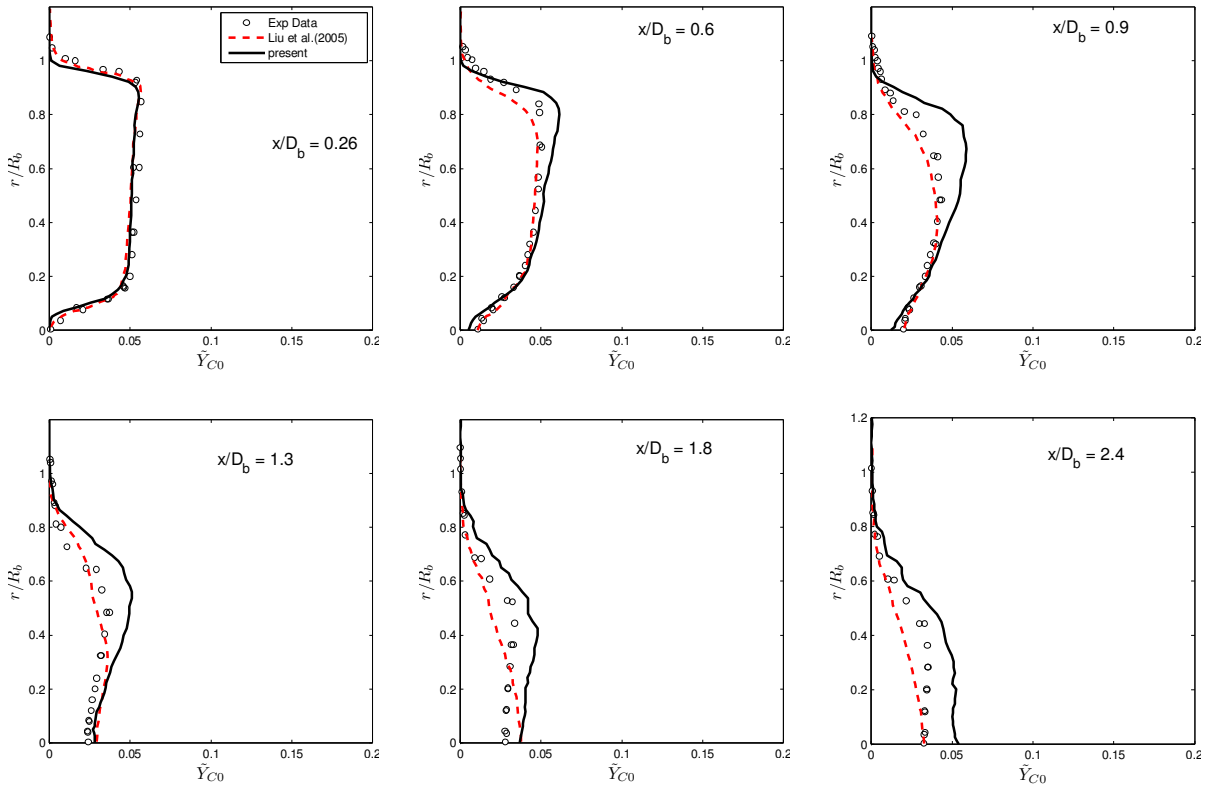


Figure 5.6: The detailed chemistry computations of the bluff-body flame 'HM1' using the ARM2 mechanism. The radial profiles of the mean mass fraction of CO compared with the experimental data and with the previous numerical simulations of Liu et al. [25].

hybrid algorithm is applied to this flame using the ARM2 [61] finite-rate chemistry model.

Figure 4.1 shows the configuration of the Sydney swirl burner and Table 4.1 summarizes the charactristic of the flame 'SM1'. The same computational domain and boundary conditions are used as in the flamelet case discussed in Section 4.3.

5.3.1 Results

Detailed chemistry calculations are performed for the swirling bluff-body flame 'SM1'. The submodels are the same as those used in the flamelet calculations except for the mixing and chemistry models. The EMST [60] and the ARM2 [61] methane

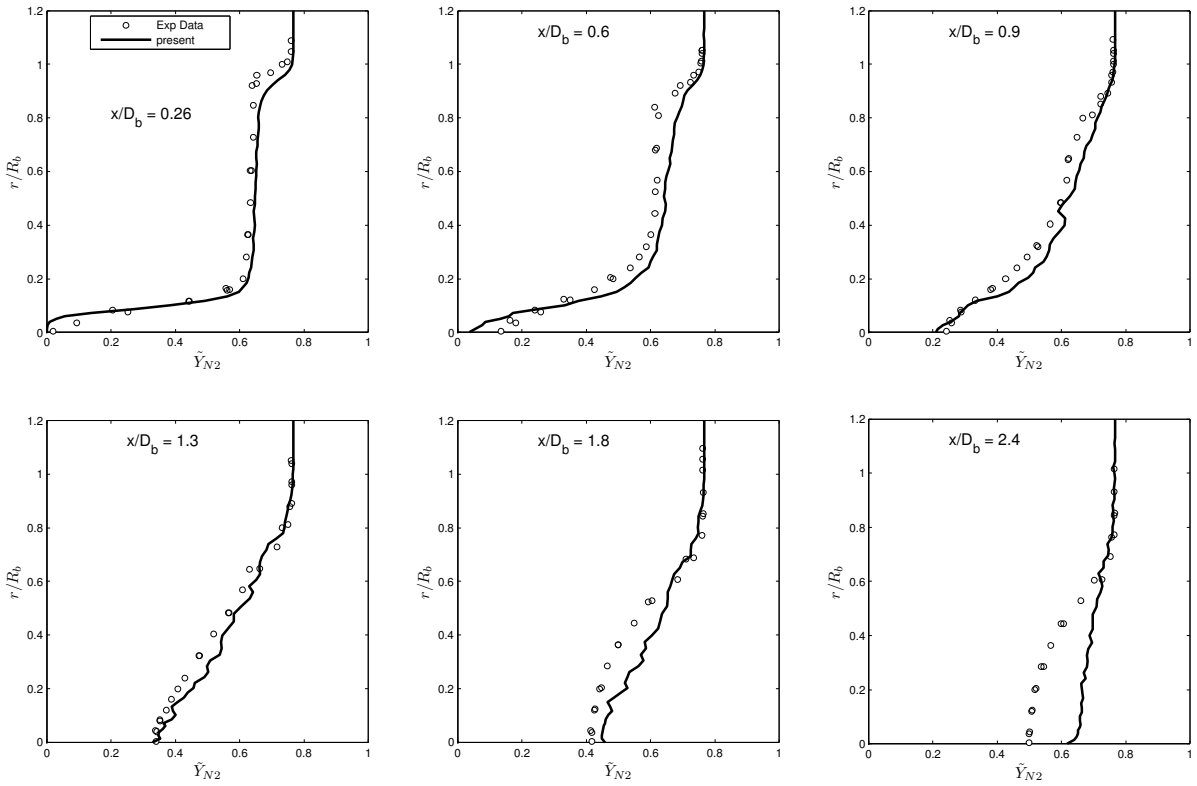


Figure 5.7: The detailed chemistry computations of the bluff-body flame 'HM1' using the ARM2 mechanism. The radial profiles of the mean mass fraction of N2 compared with the experimental data [75].

oxidation mechanism are used for the mixing and chemistry models, respectively. The ISAT error tolerance is again taken as $\epsilon_{\text{tol}} = 10^{-4}$ similar to the 'HM1' flame. The boundary conditions are same as the flamelet calculations of this flame as discussed in Chapter 4 except or the compositions that are provided by ISAT. All simulations are performed using a 96×96 grid.

Mean velocity field:

First the flow field obtained using the ARM2 chemistry model is compared with the experimental data [75] and also with the scalar PDF simulations of De Meester et al. [8]. For this purpose, the radial profiles of the time averaged mean axial $\tilde{U}$ and tangential $\tilde{W}$ velocities at axial locations of $x/D_b = 0.136$, 0.4, 0.8, 1.2, 1.4, and

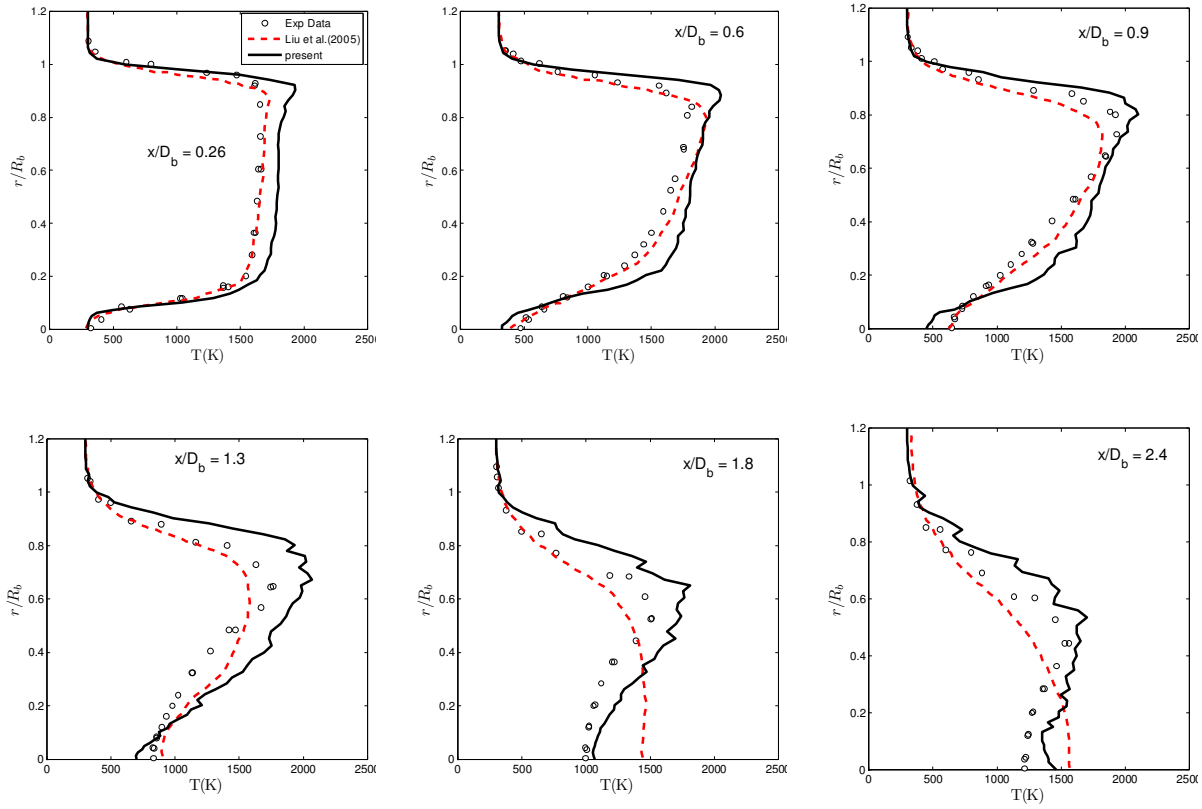


Figure 5.8: The detailed chemistry computations of the bluff-body flame 'HM1' using the ARM2 mechanism. The radial profiles of the mean temperature compared with the experimental data and with numerical simulations of Liu et al. [25].

2.0 are shown in Figs. 5.15 and 5.16, respectively. It can be seen in these figures that there is no significant difference between the flamelet and the detailed chemistry results. Since the flow field computed using the detailed chemistry model is essentially same as that computed using the flamelet model, the reader is referred to Chapter 4 for a detailed discussion of the flow field predictions.

Mean composition fields:

The Favre-averaged mean mass fraction of species and temperature are shown at axial locations $x/D_b = 0.2, 0.4, 0.8, 1.1, 1.5$, and 3. The computed results are compared with the experimental data which are available in the website of University of Sydney [75]

and with the earlier scalar PDF calculations of De Messter et al. [8] who used EMST model for mixing and a progress variable model for the chemistry.

Figure 5.17 shows the computed radial profiles of the mean mass fraction of H2O compared with the experimental data. At most of the axial locations the present results are in good agreement with the experimental data. In Fig. 5.18 the radial profiles of the mean mass fraction of CO2 are compared with the experimental data and with the simulations of De Messter et al. [8]. Although there are some discrepancies in the centerline, there is overall reasonable agreement with the experimental measurements. As can be seen in Fig. 5.19 the mass fraction of CO is well predicted by the calculations even in the downstream locations. Figure 5.20 compares the mean temperature with the experimental data. Except in immediate vicinity of the bluff-body, i.e., $x/D_b = 0.2$ the results are in good agreement with the experimental data. In Fig. 5.21 the mean mixture fraction at different axial locations are compared with the experimental data and also with the PDF simulations of De Meester et al. [8]. As can be seen in the figure the present results are similar to those obtained using the flamelet model except for the axial location $x/D_b = 0.2$ where the mean mixture fraction is underestimated by the detailed chemistry model.

Scatter plots:

Figures 5.22–5.24 show the scatter plots of temperature and the mass fractions of species CO and CO2 against the mixture fraction at locations $x/D_b = 0.4$, 0.8, and 1.5. In these figures the detailed chemistry results are compared with the flamelet and also with the experimental results [75]. It is found that the data bands in the joint PDF calculations are narrower than those of the experimental data similar to the non-swirling bluff-body case. The measured temperature scatter plots show that there are significant local extinction at all the axial locations. However, similar to the 'HM1' flame no significant local extinction is observed in the PDF simulations

of 'SM1' flame. Also the computed maximum temperature values at different axial locations are under predicted compared to the experimental measurements. Failure in the prediction of local extinction in the present computation affects the prediction of the other parameters especially the mass fraction of species CO2 and CO. In addition, it can be seen that the finite-rate chemistry simulations predict the mass fraction of carbon dioxide (CO2) lower than flamelet model but reversely the mass fraction of carbon monoxide (CO) is estimated higher than the flamelet model especially near the stiochiometric mixture fraction.

5.4 Summary

In this chapter the new hybrid FV/particle Monte Carlo method is coupled with the most recent ISAT algorithm [46] developed by Pope group to perform PDF simulations with finite-rate detailed-chemistry models. First we performed detailed chemistry calculations for the non-swirling bluff-body flame 'HM1' using the ARM2 [61] chemistry model. The earlier PDF simulations of this flame using a detailed chemistry model have been performed by Liu et al. [25]. The mean velocity and composition fields are compared with the experimental data and also with the PDF calculations of Liu et al. [25]. Then scatter plots of temperature and some mass fractions of species are made against the mixture fraction. These results are found to be reasonable agreement with the results reported by Liu et al. [25]. The local extinctions observed experimentally in some locations are not captured by our PDF calculations in agreement with the earlier simulations of Liu et al. [25]. Then the swirling bluff-body flame is simulated using the same detailed chemistry model, ARM2. The mean temperature and mass fractions of species are compared with the experimental data. It is emphasized here that the present study is the first application of the JPDF model with a detailed chemistry model to this class of flames. Present results are compared with the scalar

PDF calculations of De Meester et al. [8]. The results are found to be in reasonable agreement with the experimental data and also with the earlier PDF simulations of De Meester et al. [8]. The scatter plots of temperature and two species are also made against the mixture fraction at various axial locations. Significant local extinctions observed experimentally for this flame are not observed in the present PDF simulations similar to the non-swirling flame case. This failure affected the prediction of the mass fractions of other species such as CO2 and CO.

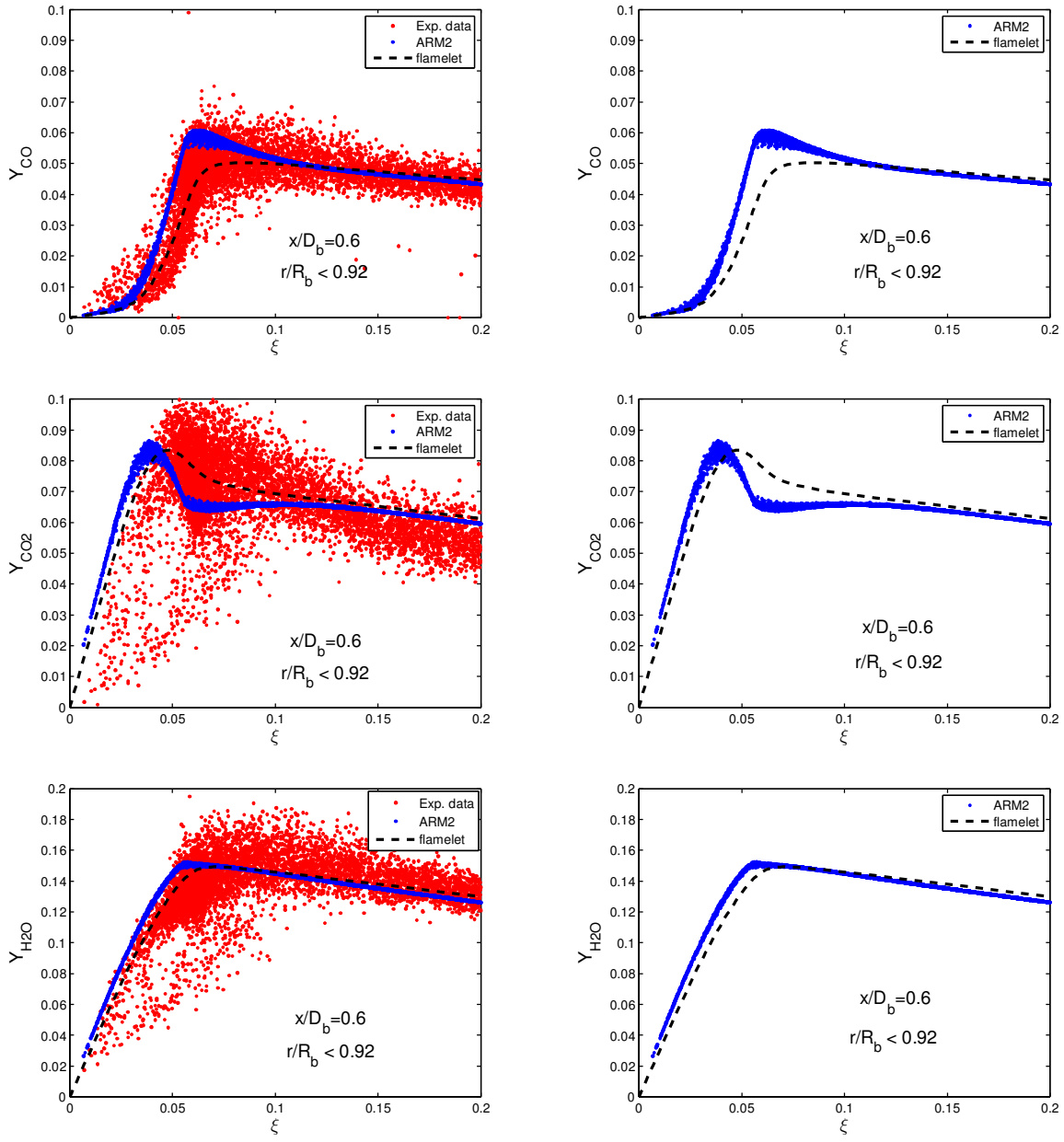


Figure 5.9: The detailed chemistry computations of the bluff-body flame 'HM1' using the ARM2 mechanism. Scatter plots of the mass fractions of CO, CO2, and H2O against mixture fraction at the axial location $x/D_b = 0.6$. The detailed chemistry results (blue-dots) are compared with the flamelet model (dashed-line) and the experimental data (red-dots) [75].

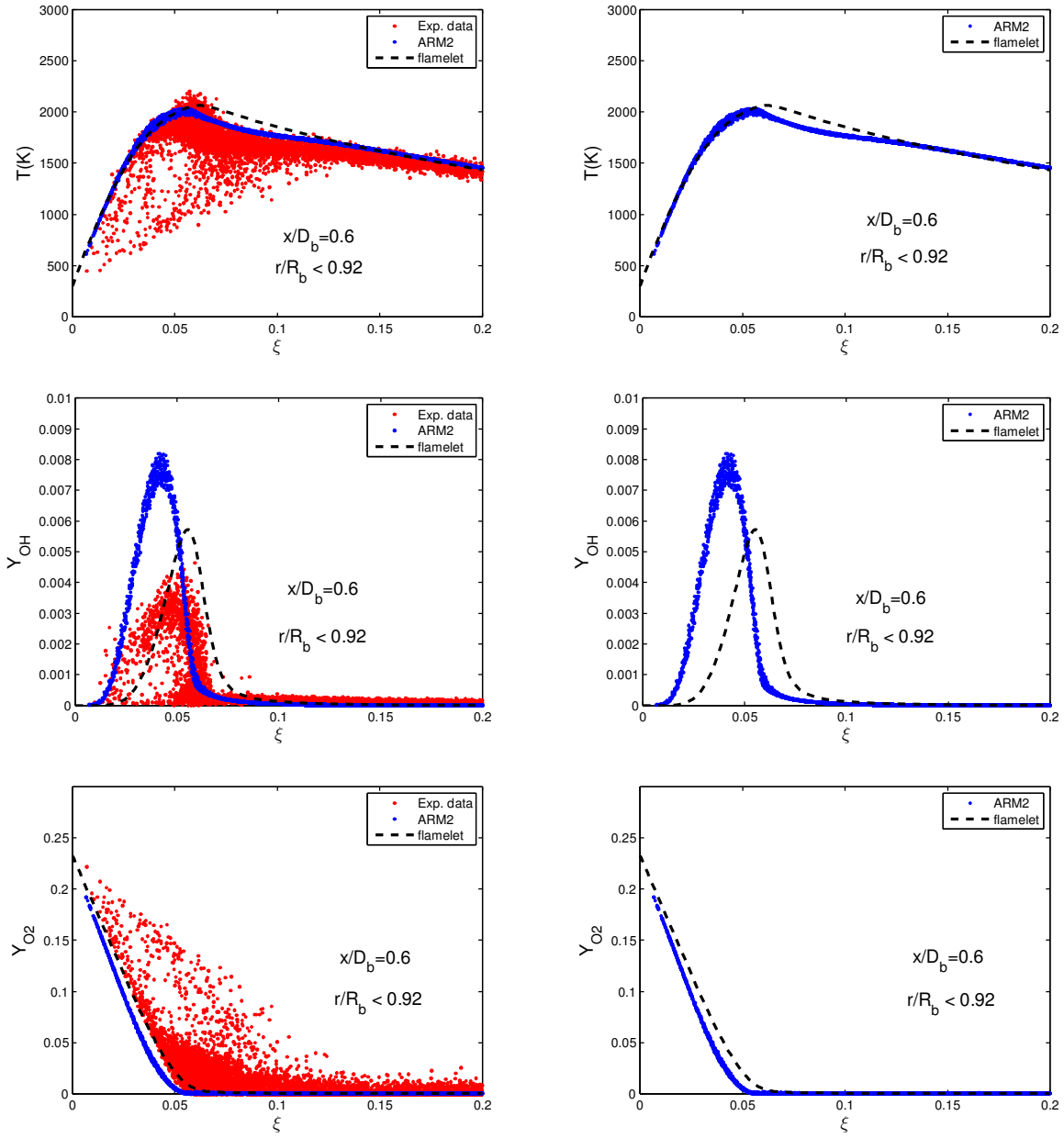


Figure 5.10: The detailed chemistry computations of the bluff-body flame 'HM1' using the ARM2 mechanism. Scatter plots of the mass fractions of OH and O2, and temperature against mixture fraction at the axial location $x/D_b = 0.6$. The detailed chemistry results (blue-dots) are compared with the flamelet model (dashed-line) and the experimental data (red-dots) [75].

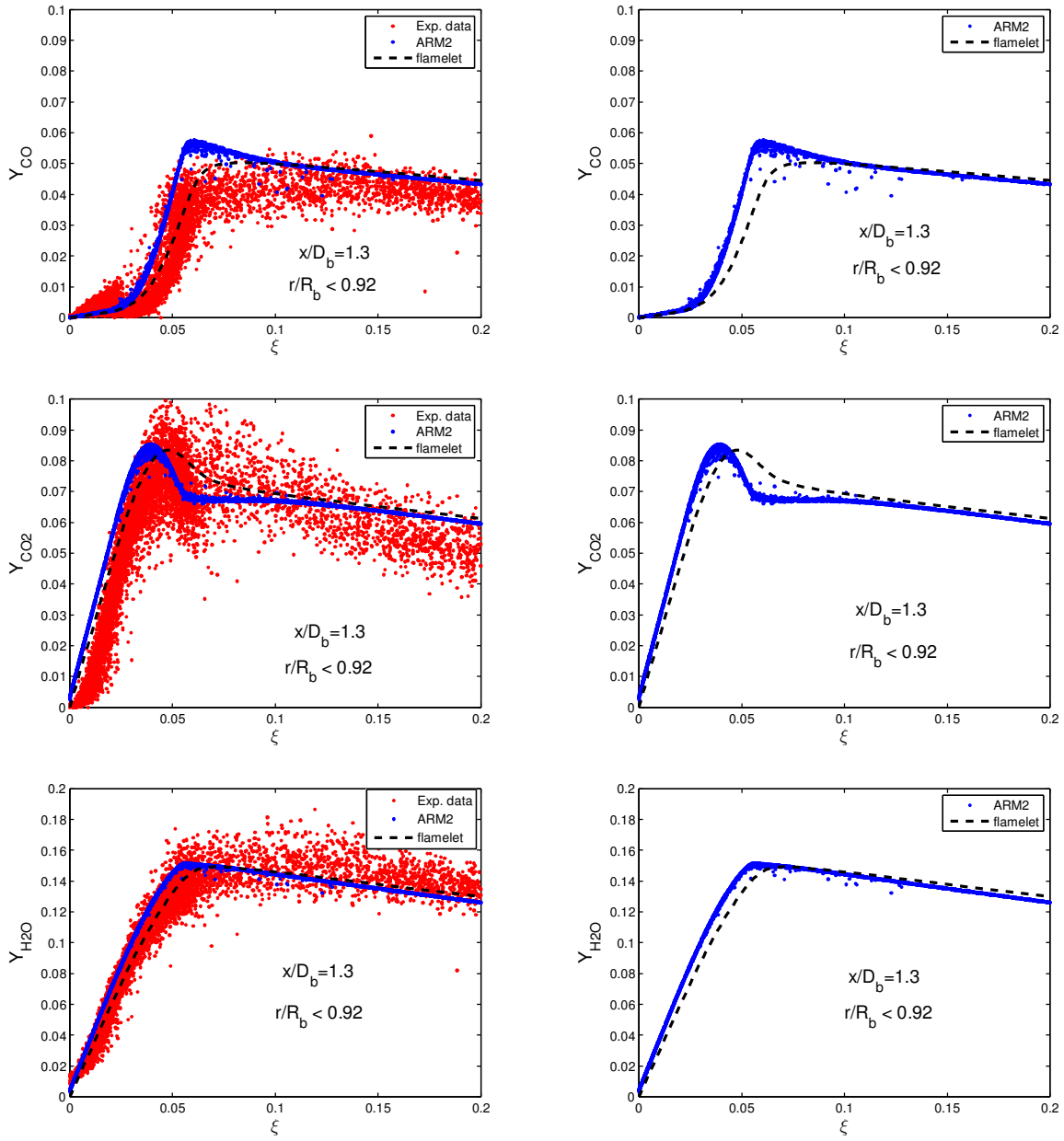


Figure 5.11: The detailed chemistry computations of the bluff-body flame 'HM1' using the ARM2 mechanism. Scatter plots of the mass fractions of CO, CO2, and H2O against mixture fraction at the axial location $x/D_b = 1.3$. The detailed chemistry results (blue-dots) are compared with the flamelet model (dashed-line) and the experimental data (red-dots) [75].

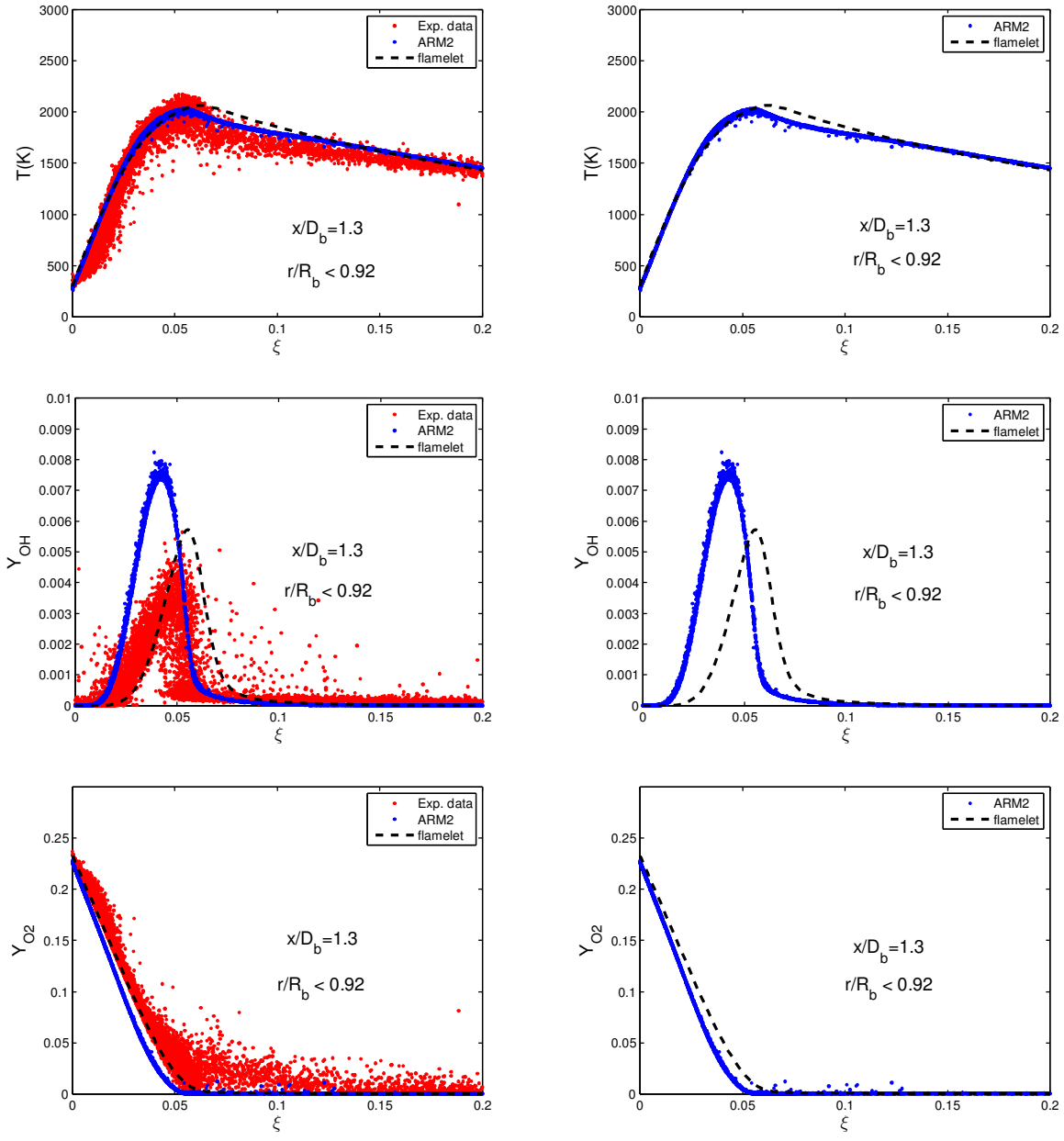


Figure 5.12: The detailed chemistry computations of the bluff-body flame 'HM1' using the ARM2 mechanism. Scatter plots of the mass fractions of OH and O2, and temperature against mixture fraction at the axial location $x/D_b = 1.3$. The detailed chemistry results (blue-dots) are compared with the flamelet model (dashed-line) and the experimental data (red-dots) [75].

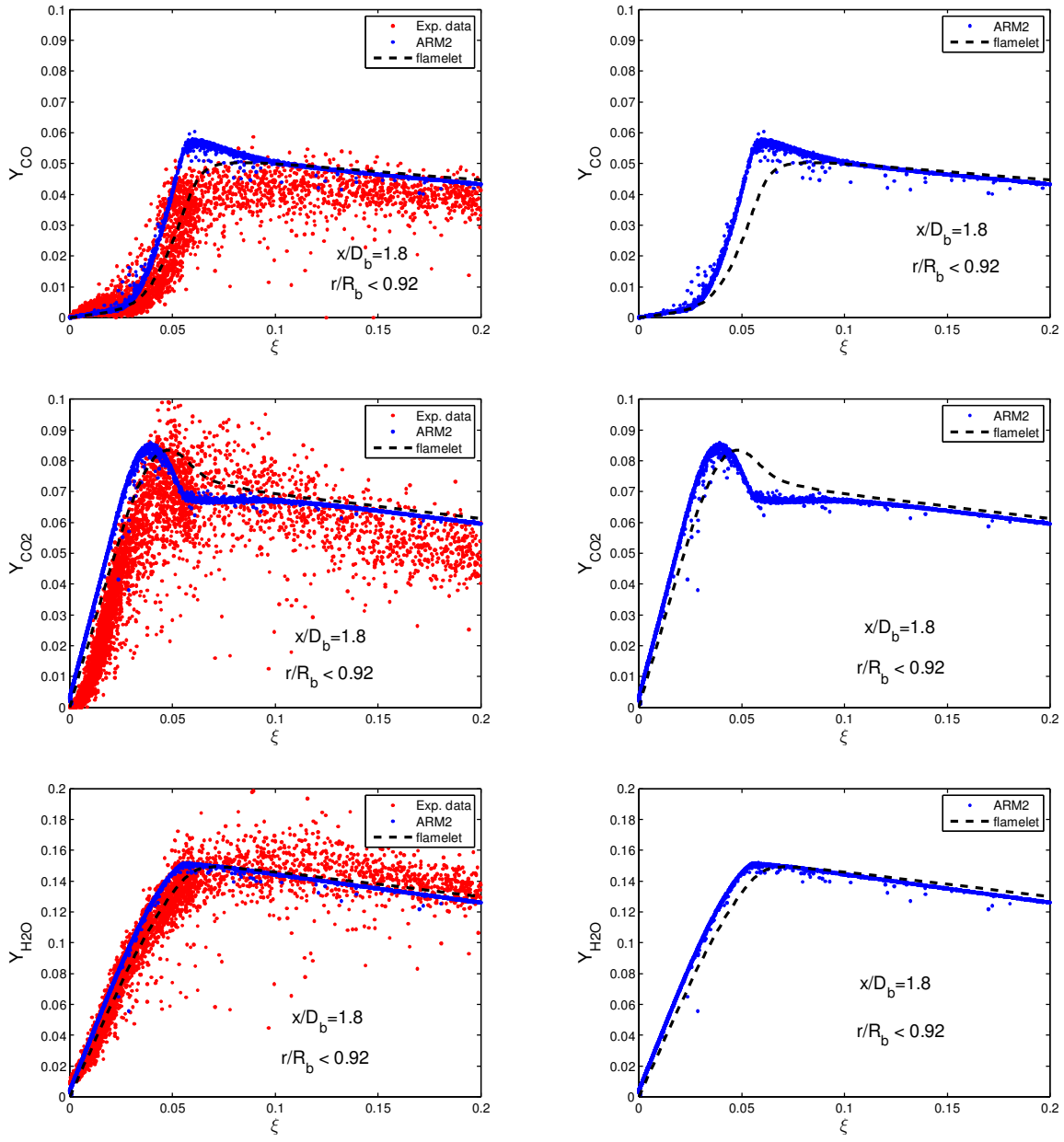


Figure 5.13: The detailed chemistry computations of the bluff-body flame 'HM1' using the ARM2 mechanism. Scatter plots of the mass fractions of CO, CO2, and H2O against mixture fraction at the axial location $x/D_b = 1.8$. The detailed chemistry results (blue-dots) are compared with the flamelet model (dashed-line) and the experimental data (red-dots) [75].

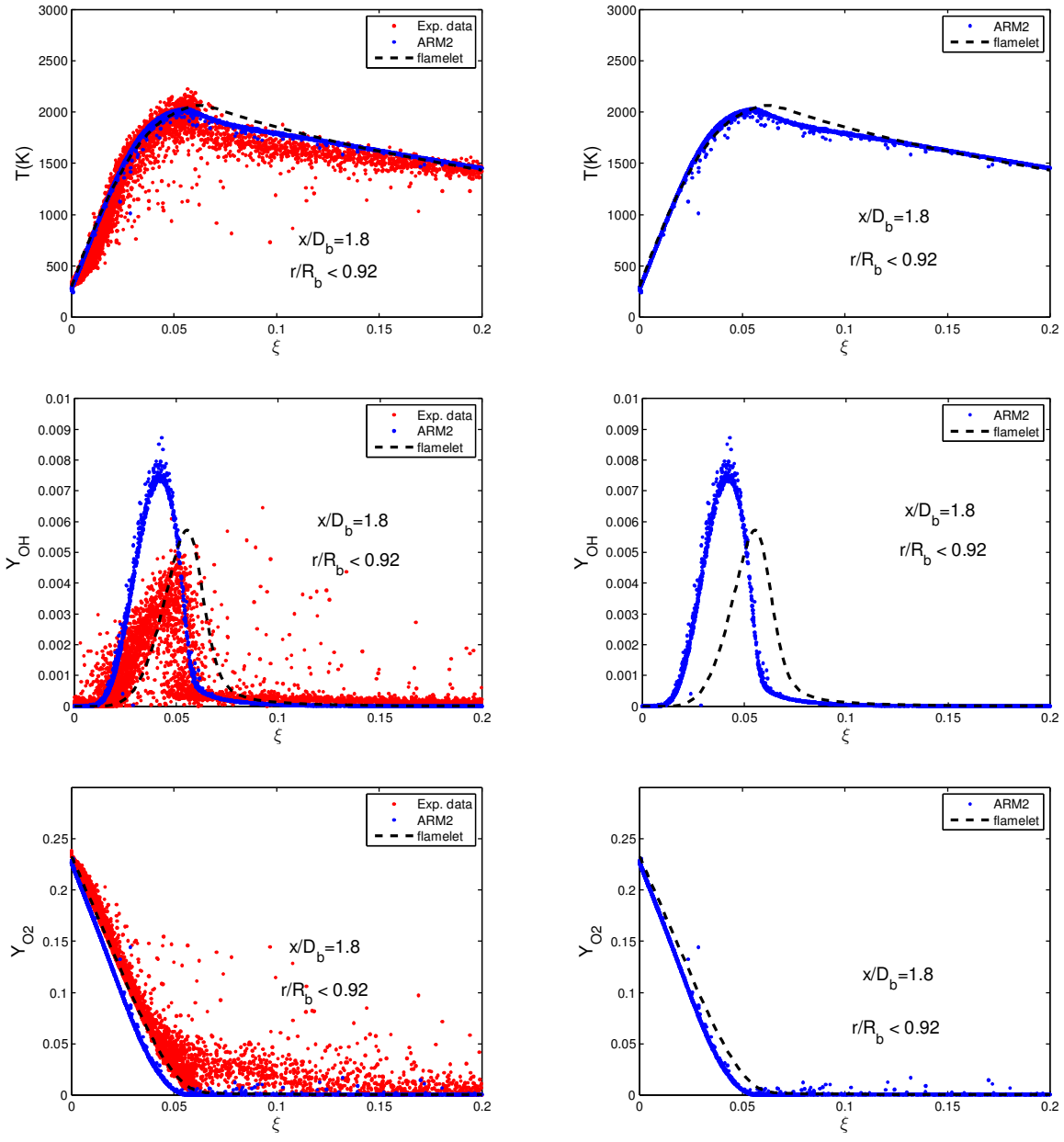


Figure 5.14: The detailed chemistry computations of the bluff-body flame 'HM1' using ARM2 mechanism. Scatter plots of the mass fractions of OH and O2, and temperature against mixture fraction at the axial location $x/D_b = 1.8$. The detailed chemistry results (blue-dots) are compared with the flamelet model (dashed-line) and the experimental data (red-dots) [75].

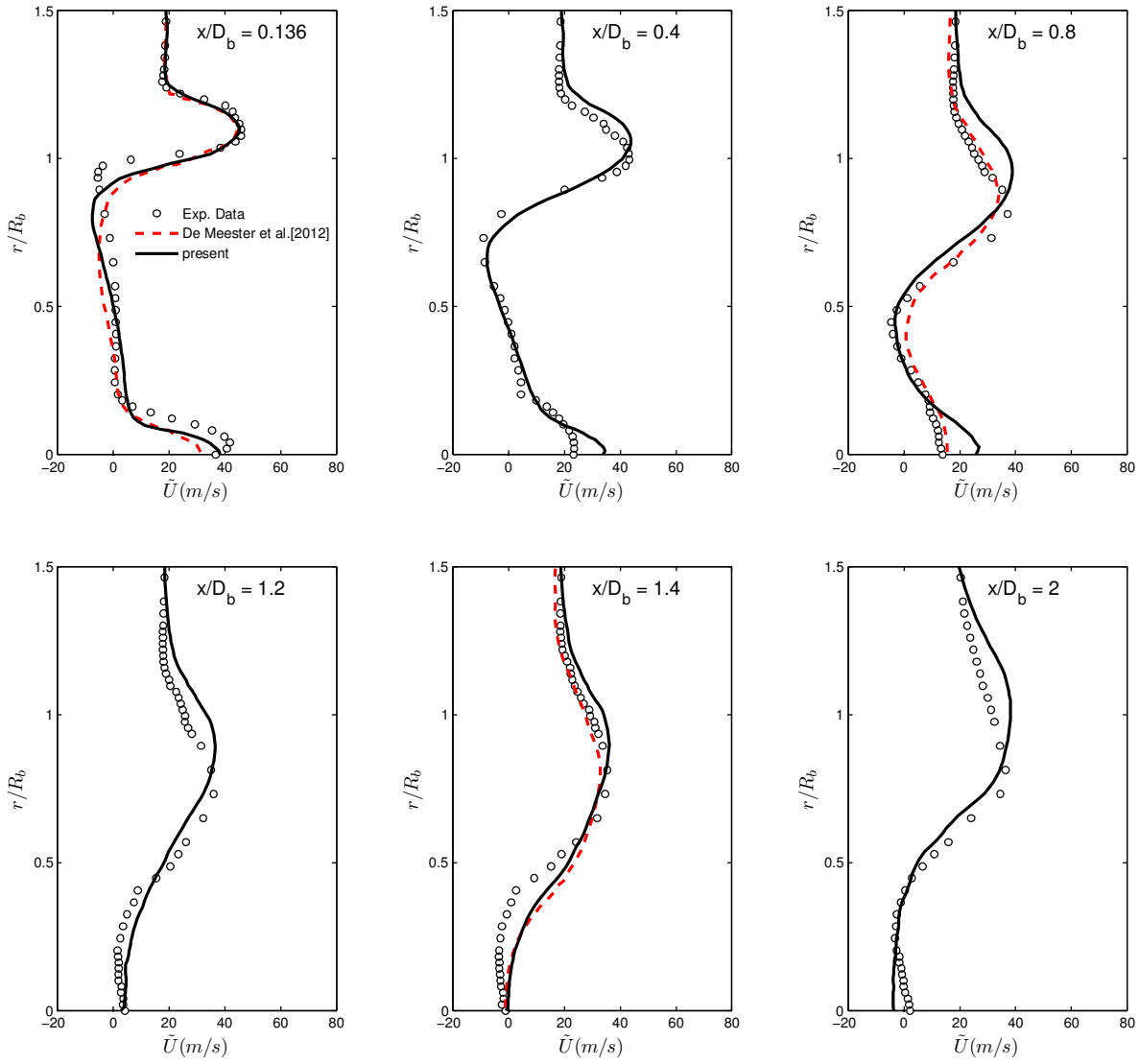


Figure 5.15: The detailed chemistry computations of the swirling bluff-body flame 'SM1' using the ARM2 mechanism. The radial profiles of the mean axial velocity compared with the experimental data [75] and the numerical results of De Meester et al. [8].

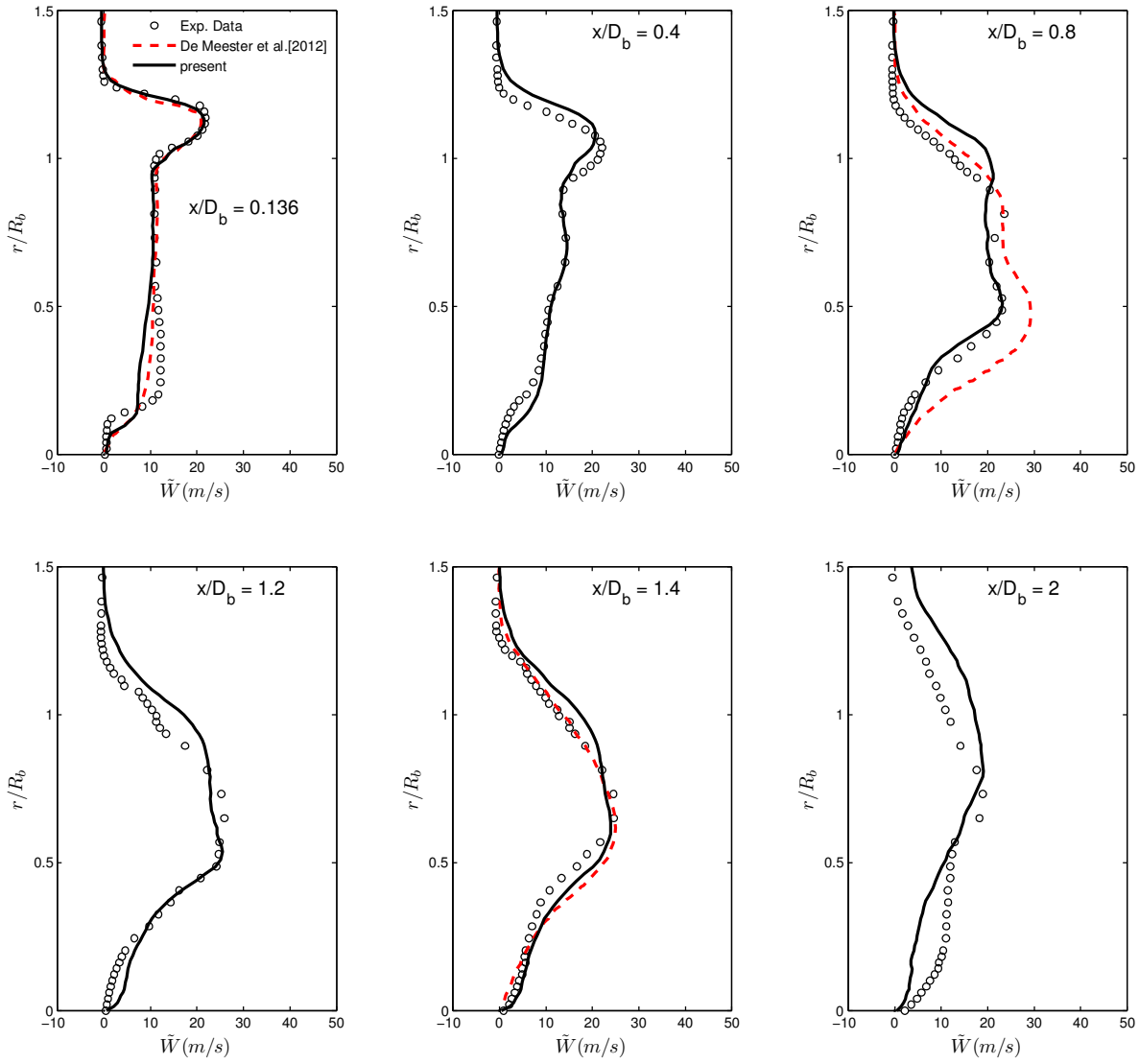


Figure 5.16: The detailed chemistry computations of the swirling bluff-body flame 'SM1' using the ARM2 mechanism. The radial profiles of the mean axial velocity compared with the experimental data [75] and the numerical results of De Meester et al. [8].

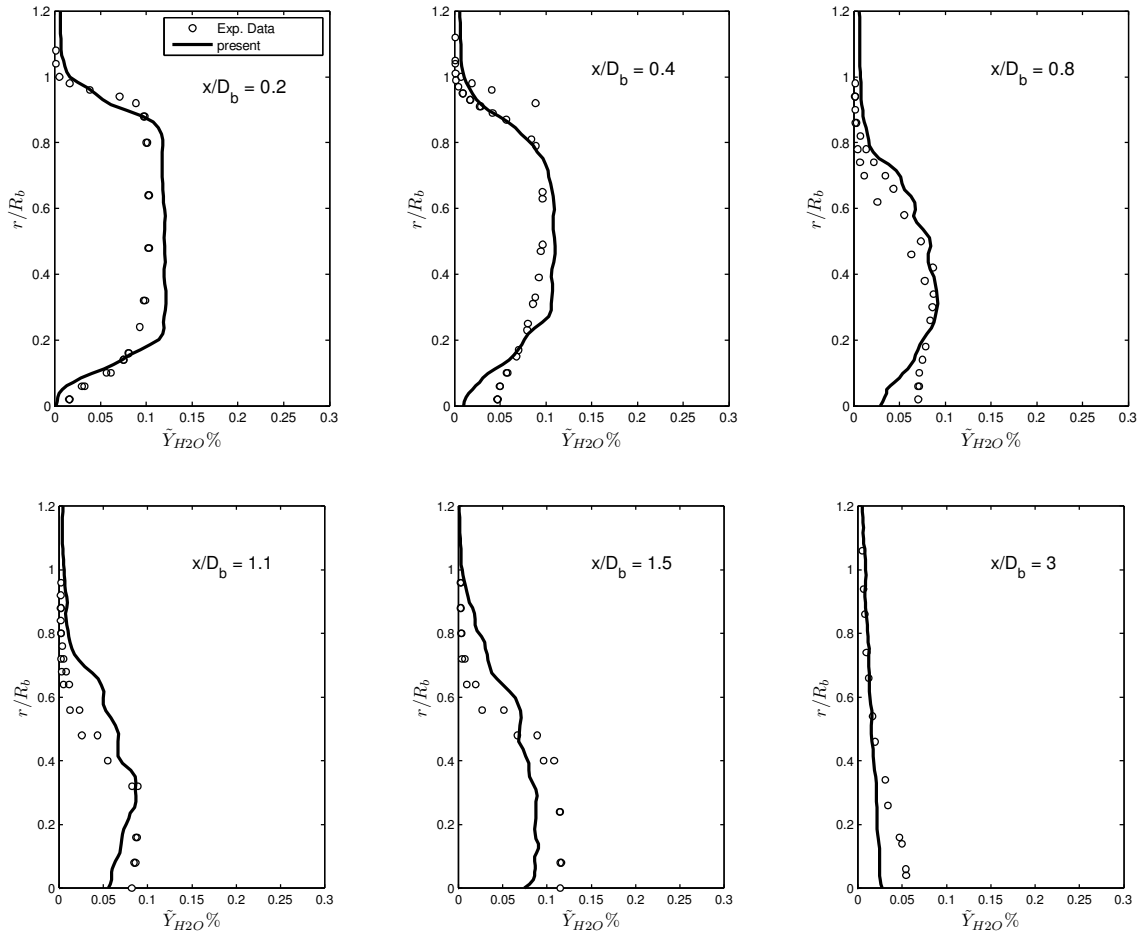


Figure 5.17: The detailed chemistry computations of the swirling bluff-body flame 'SM1' using the ARM2 mechanism. The computed radial profiles of the mean mass fraction of H2O (solid line) compared with the experimental data (symbols) [75].

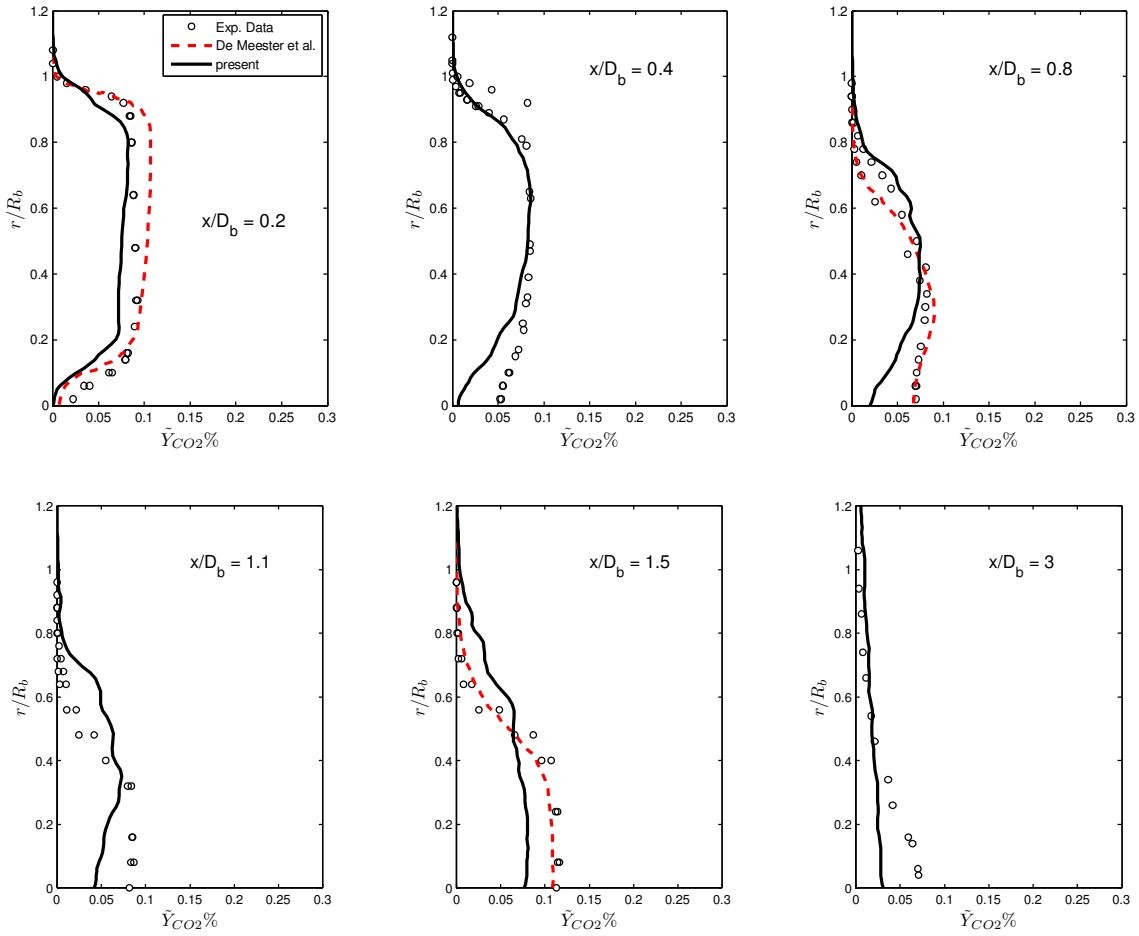


Figure 5.18: The detailed chemistry computations of the swirling bluff-body flame 'SM1' using the ARM2 mechanism. The computed radial profiles of the mean mass fraction of CO2 (solid line) compared with the experimental data (symbols) [75] and also with the earlier PDF calculation of De Meester et al. (dashed-line) [8].

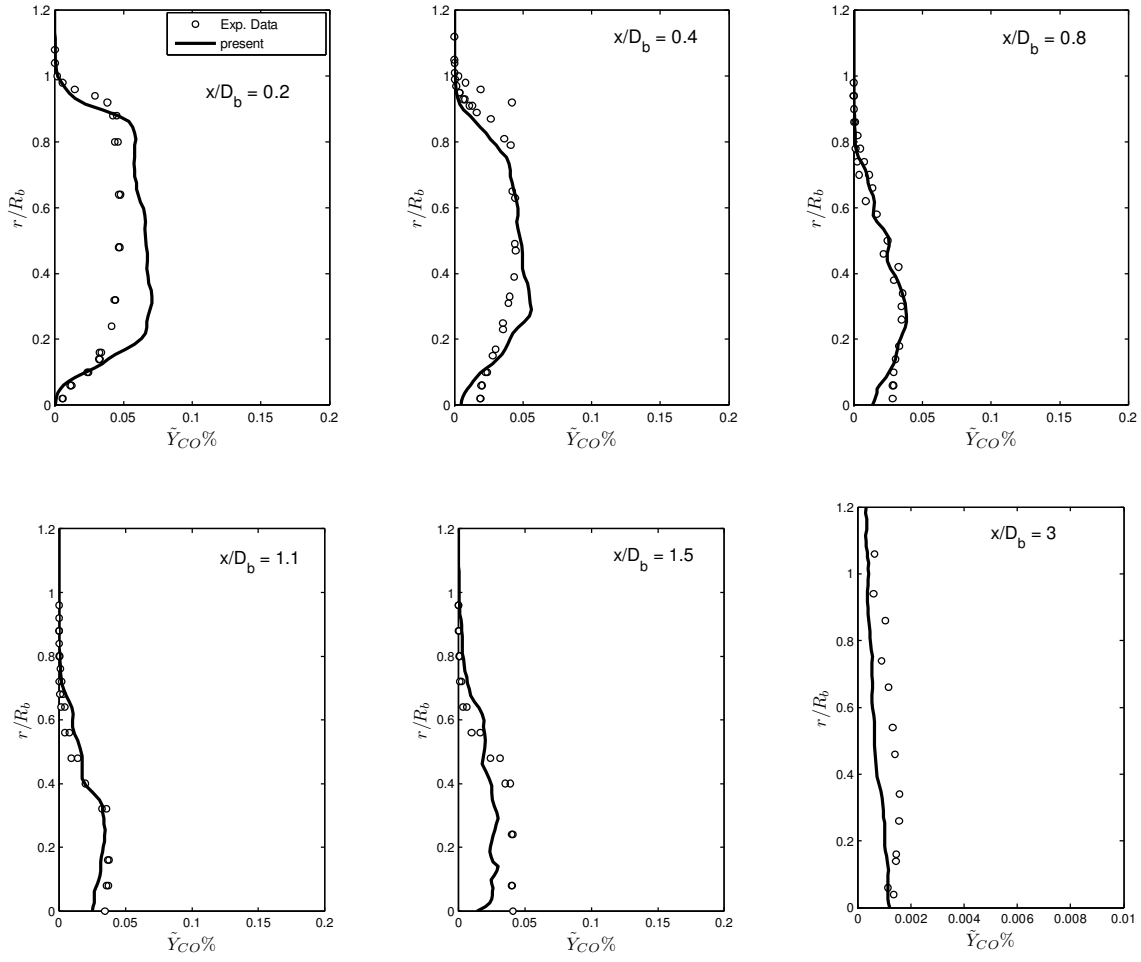


Figure 5.19: The detailed chemistry computations of the swirling bluff-body flame 'SM1' using the ARM2 mechanism. The computed radial profiles of the mean mass fraction of CO (solid line) compared with the experimental data (symbols) [75].

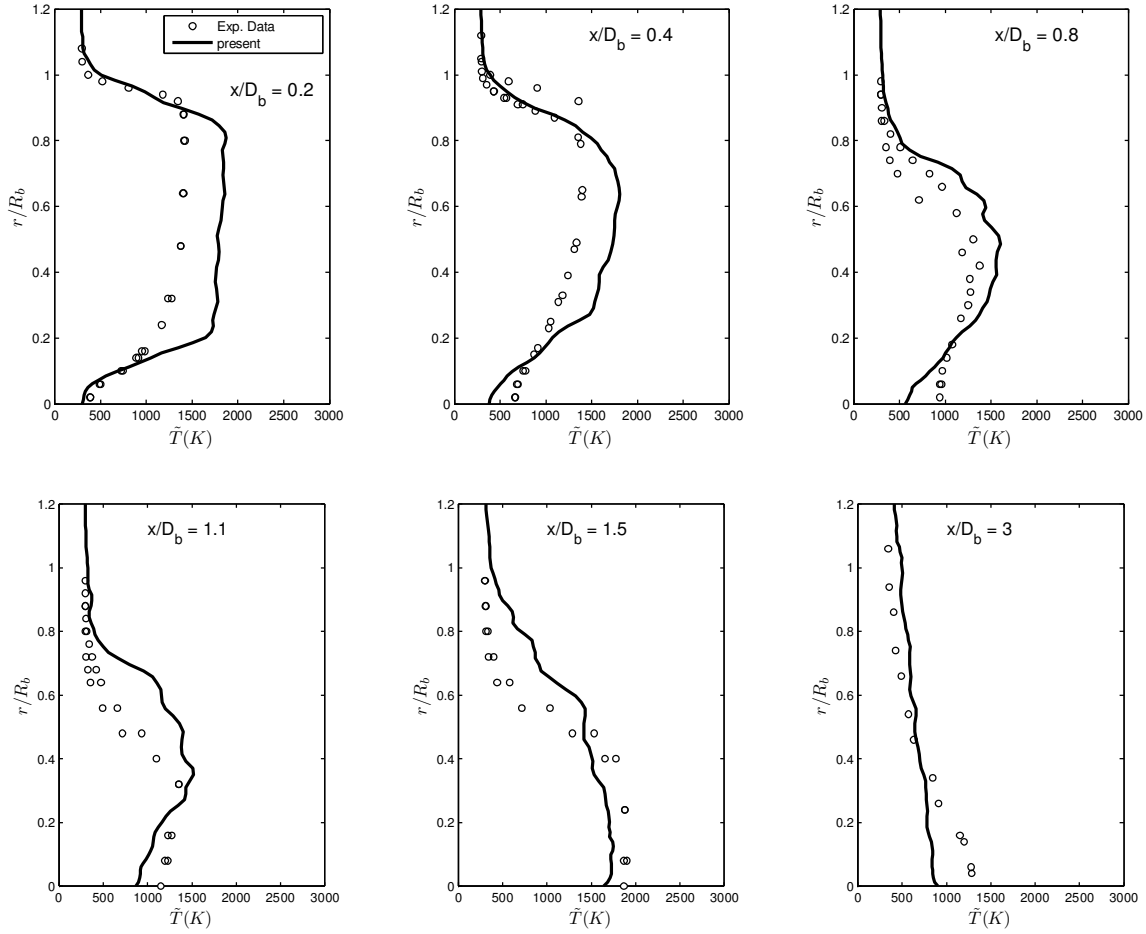


Figure 5.20: The detailed chemistry computations of the swirling bluff-body flame 'SM1' using the ARM2 mechanism. The computed radial profiles of the mean temperature (solid line) compared with the experimental data (symbols) [75].

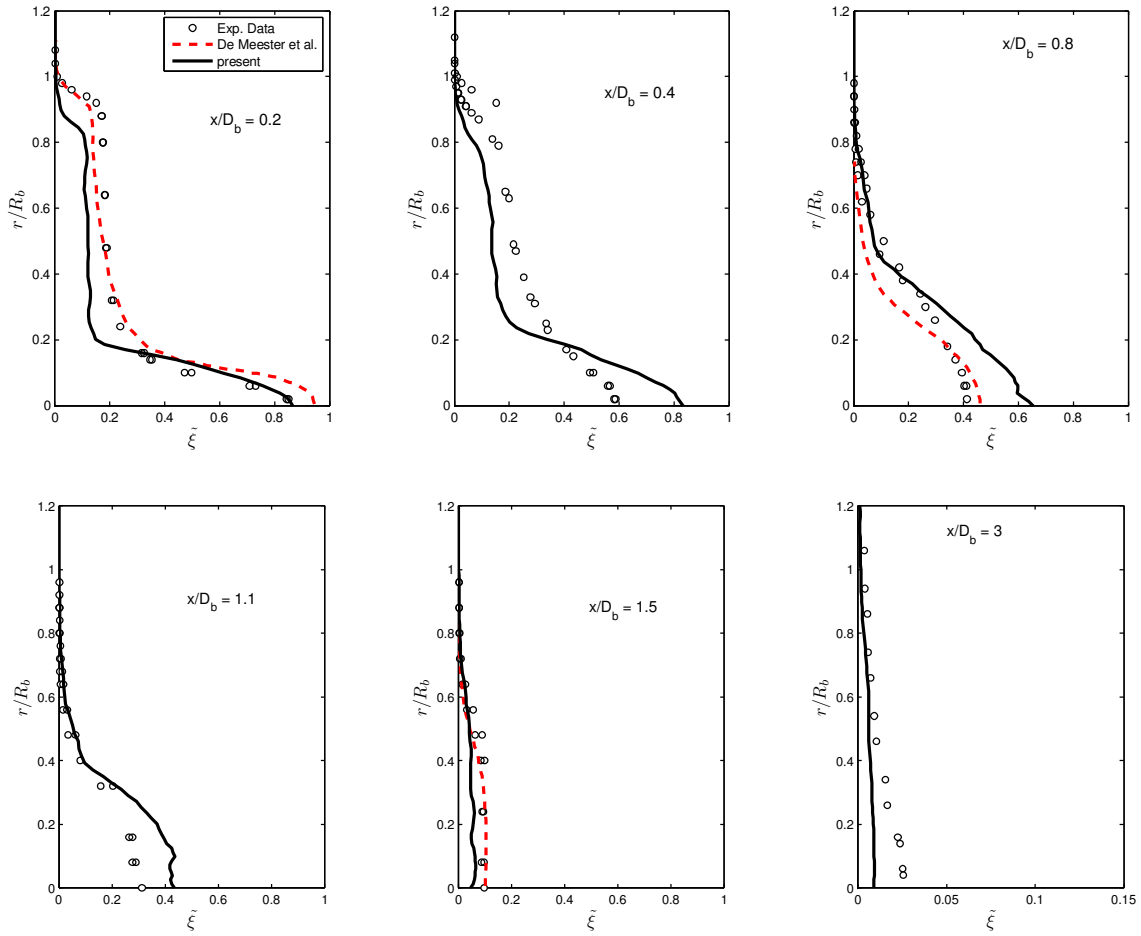


Figure 5.21: The detailed chemistry computations of the swirling bluff-body flame 'SM1' using the ARM2 mechanism. The computed radial profiles of the mean mixture fraction (solid line) compared with the experimental data (symbols) [75] and also with the earlier PDF calculation of De Meester et al. (dashed-line) [8].

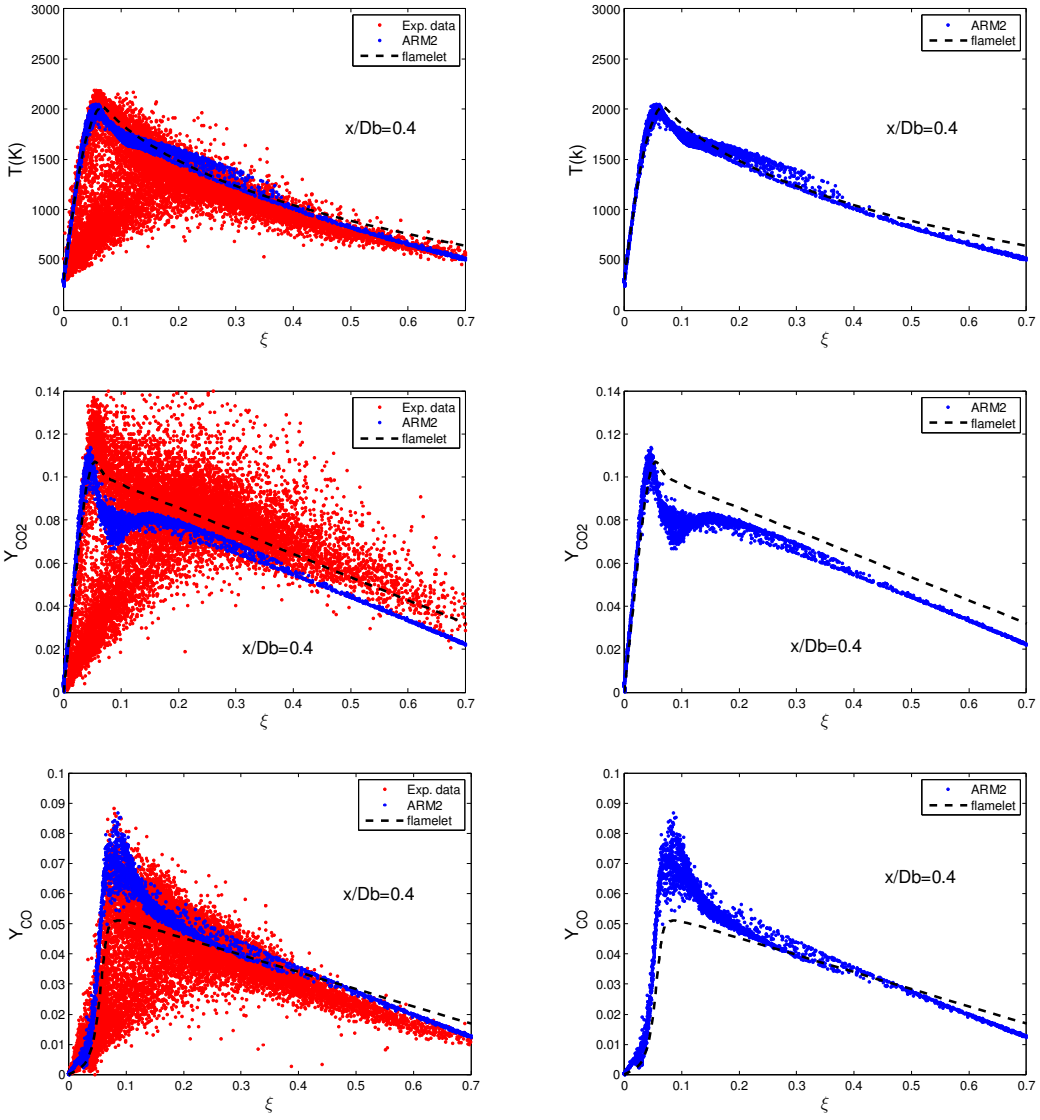


Figure 5.22: The detailed chemistry computations of the swirling bluff-body flame 'SM1' using the ARM2 mechanism. Scatter plots of temperature and mass fractions of CO2 and CO against mixture fraction at $x/D_b = 0.4$. The detailed chemistry results (blue-dots) are compared with the flamelet model (dashed-line) and the experimental data (red-dots) [75].

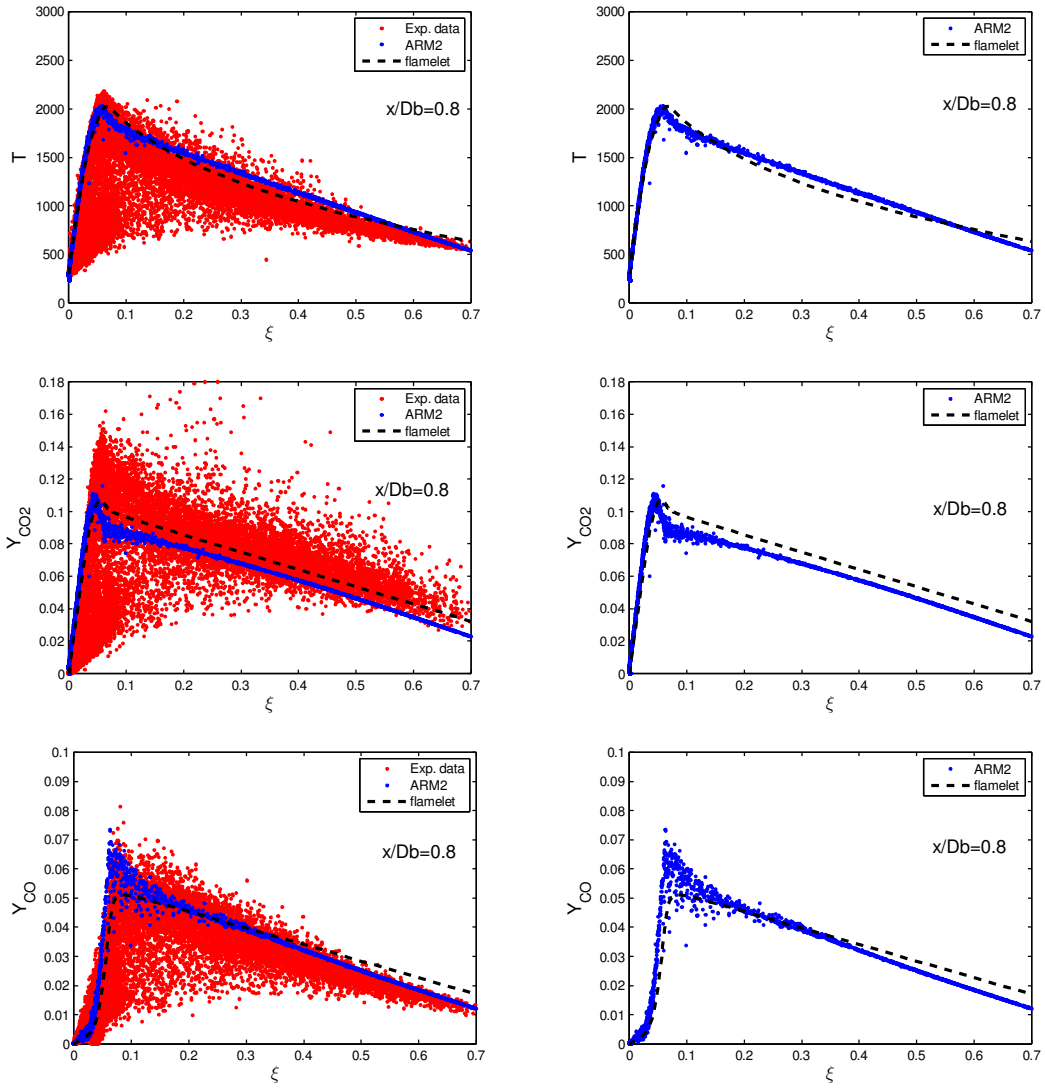


Figure 5.23: The detailed chemistry computations of the swirling bluff-body flame 'SM1' using the ARM2 mechanism. Scatter plots of temperature and mass fractions of CO2 and CO against mixture fraction at $x/D_b = 0.8$. The detailed chemistry results (blue-dots) are compared with the flamelet model (dashed-line) and the experimental data (red-dots) [75].

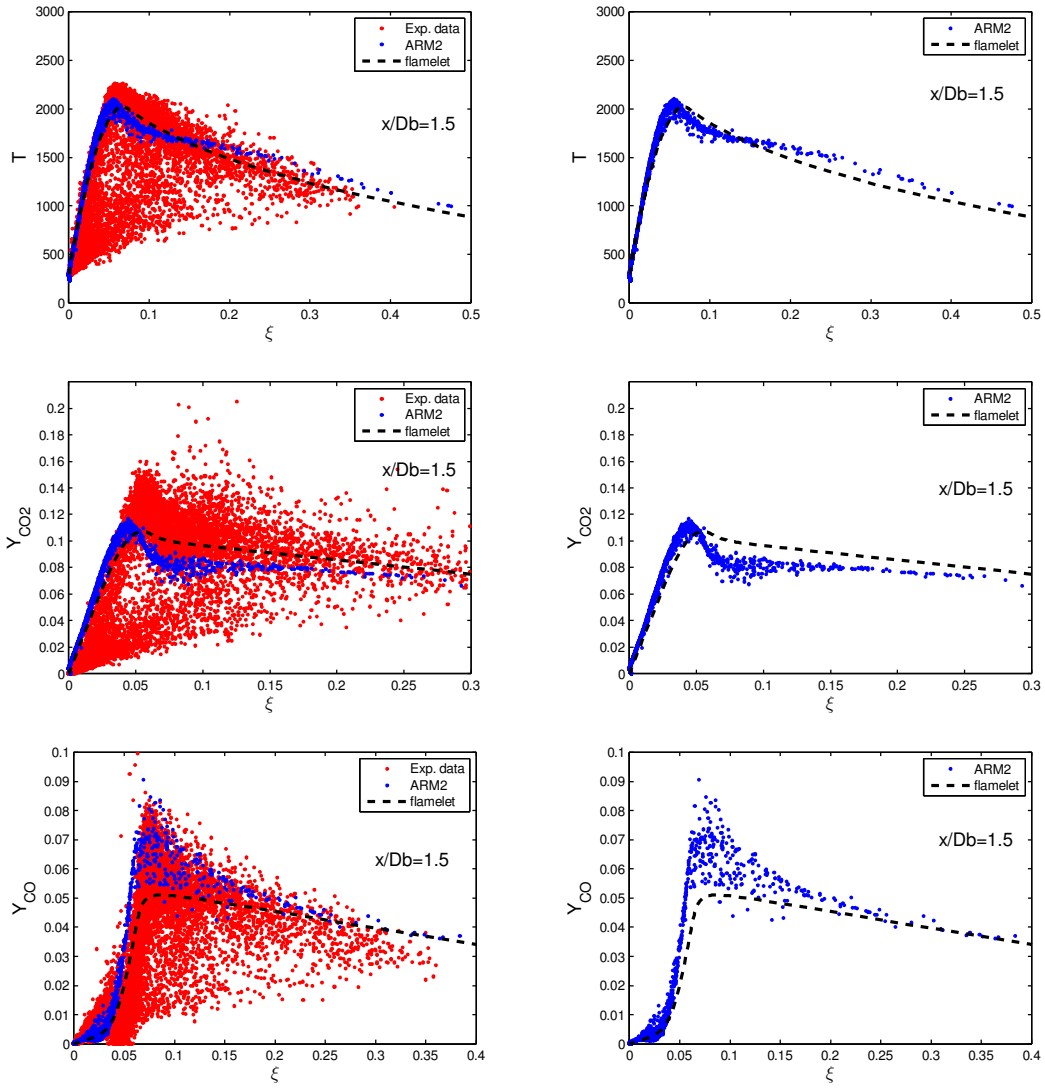


Figure 5.24: The detailed chemistry computations of the swirling bluff-body flame 'SM1' using the ARM2 mechanism. Scatter plots of temperature and mass fractions of CO2 and CO against mixture fraction at $x/D_b = 1.5$. The detailed chemistry results (blue-dots) are compared with the flamelet model (dashed-line) and the experimental data (red-dots) [75].

Chapter 6

Conclusions

A new robust hybrid finite-volume (FV)/particle-base Monte Carlo method has been developed for solving joint PDF model equations of turbulent reactive flows. In the present hybrid method, a pressure-based PISO-FV solver is combined with the particle-based Monte Carlo algorithm. The mean density field is extracted from the particles and passed to the FV solver. This is in contrast with the original hybrid approach in which the mean energy conservation equation is solved by the FV method and mean density field is subsequently computed from the mean equation of state. Thus the redundant FV density field is removed in the present approach. This is of significance since it makes the new hybrid algorithm more consistent at the numerical solution level and eliminates the need for the energy correction algorithm. In spite of noisy mean density field, the FV algorithm is found to be very robust. The velocity and position correction algorithms developed by Muradoglu et al. [39] are adopted to make the new hybrid method fully consistent at the numerical solution level. The local time stepping method developed by Muradoglu and Pope [38] has been also incorporated into the present hybrid algorithm and found to accelerate convergence to a statistically stationary solution significantly especially when a highly stretched grid is used.

The new hybrid algorithm is first applied to simulate the non-swirling cold bluff-body flow. In contrast with the original hybrid method, the new hybrid algorithm is found to be very robust with respect to grid refinement, i.e., it does not result in any unphysical vortex shedding even when a highly fine grid is used. It is thus concluded that the unphysical vortex shedding observed in the old loosely-coupled hybrid method was not due to the deficiency of the models employed but rather due to the excessive numerical dissipation in its density-based FV solver. The method is then applied to simulate the non-swirling reacting bluff-body flame 'HM1E'. It is found that the new hybrid method predicts the flow field in the recirculation region better than the old hybrid algorithm. Extensive simulations are then performed for this flame to assess the numerical properties of the present hybrid algorithm. It is demonstrated that the method is convergent in terms of reaching a statistically stationary state and also in terms of grid refinement and number of particles per cell. It is found that both the bias and spatial errors converge at expected rates and the bias error is much smaller than the spatial error on a typical grid employed in PDF simulations, i.e., the bias error is virtually eliminated. The robustness of the new algorithm is demonstrated by simulating more complicated flow of the Sydney swirling bluff-body flame 'SM1'. The new algorithm is found to be very robust for this difficult test case and the results are in good agreement with the available experimental data and also with the earlier PDF calculations of De Meester et al. [8].

Finally the new algorithm is also coupled with ISAT-CK7 package for enabling the method to deal with the detailed chemistry calculations. First, these calculations are performed for the bluff-body flame 'HM1'. The mass fraction of compositions and also scatter plots of different species are compared with the experimental data and also with the previous PDF results of Liu et al. [25]. Then similar calculations are also performed for the swirling flame 'SM1'. The computed results are found to be

overall in good agreement with the experimental data for the mean fields but failed to predict local extinction observed both in 'HM1' and 'SM1' flames.

The current implementation is extensible for the LES/PDF method. The open source framework of OpenFOAM allows for rapid implementation of existing turbulence and combustion models as well as models to be developed in the future. This will potentially accelerate the new model developments. The OpenFOAM framework also makes it easier to apply PDF methodology to industrial scale problems such as gas turbine combustors.

Appendix A

Supplementary Results

In this Appendix, more results are presented to demonstrate the grid convergence of the hybrid method for the non-reacting bluff-body flow and the swirl-stabilized bluff-body flame 'SM1'. In Section 3.3 the grid convergence was shown for the cold bluff-body flow only at one axial cross-section. Here the results are presented at axial locations of x/D_b =0.06, 0.2, 0.4, 0.8, 1, 1.2, 1.3, 1.8, 2.4, 3.4 and 4.4 for the mean axial velocity, mean radial velocity, rms axial velocity and rms radial velocity in Figs. A.1–A.4, respectively.

The Sydney swirl-stabilized flame 'SM1' was simulated in Chapter 4. The grid convergence was also shown only for one axial location for this flame. Here the grid convergence for all the sections where experimental data are available is shown in Figs. A.5–A.10.

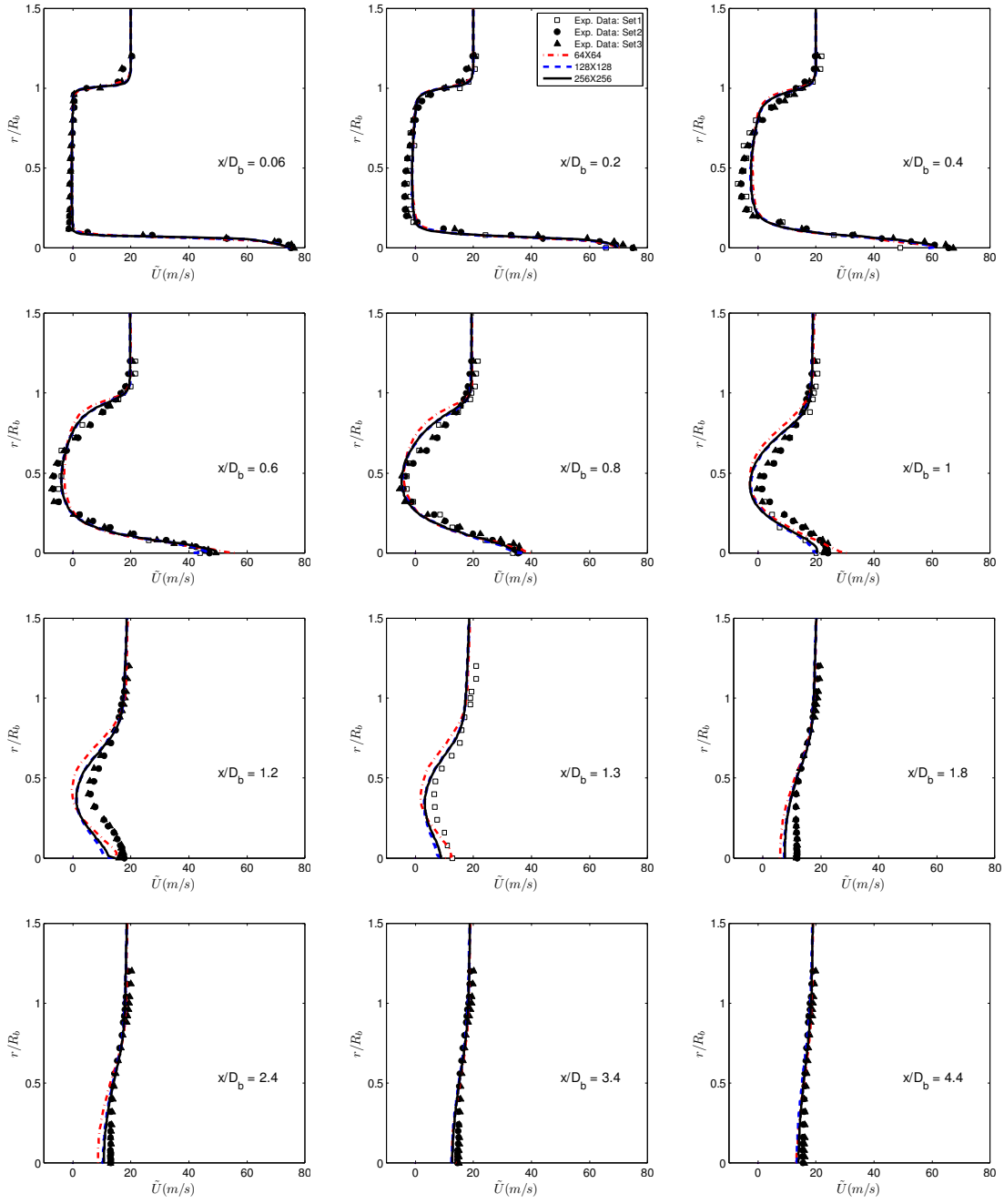


Figure A.1: Grid convergence for the cold bluff body flow. The radial profiles of the mean axial velocity for three different grids, i.e., 64×64, 128×128, and 256×256, are compared with the experimental measurements [75].

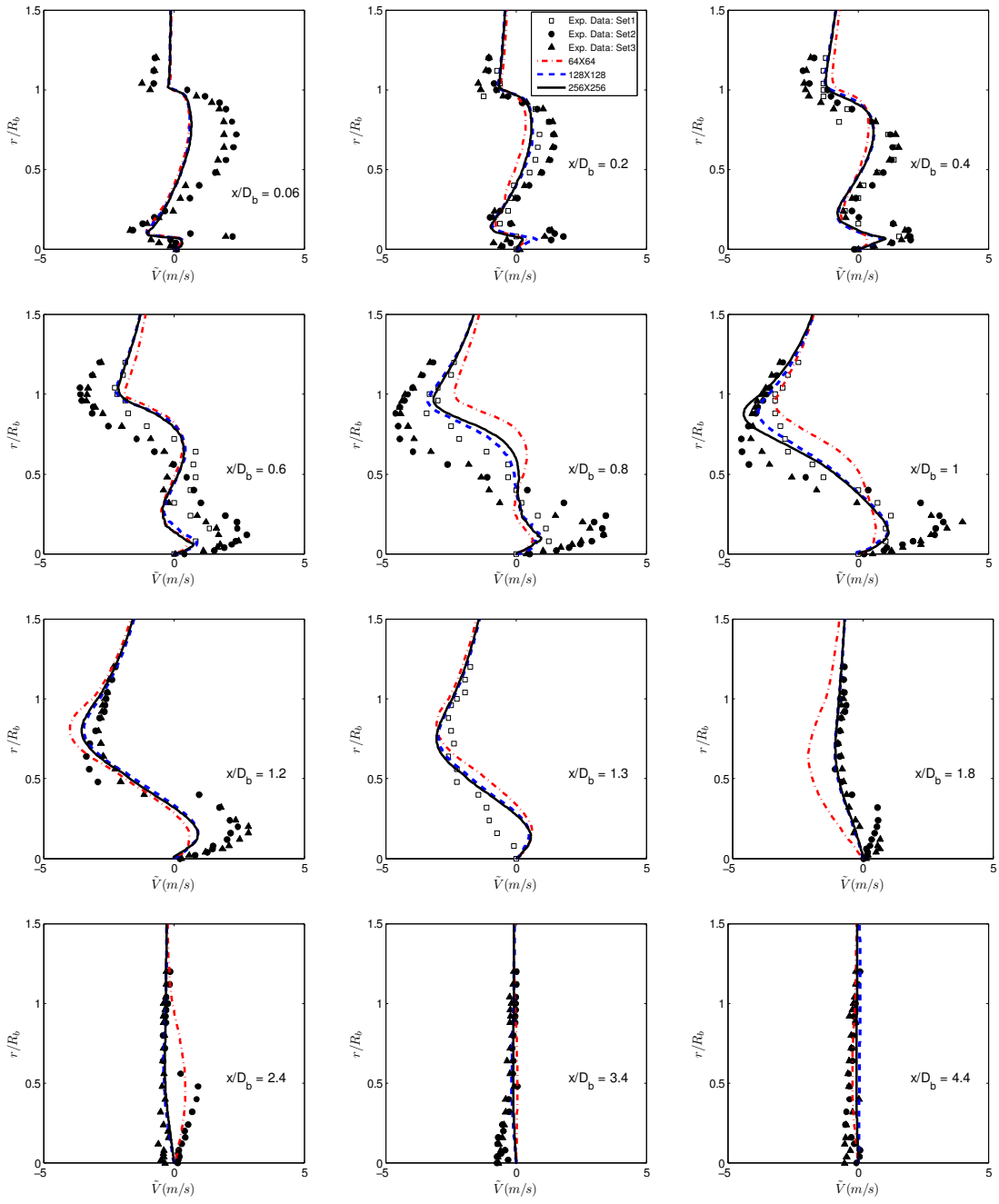


Figure A.2: Grid convergence for the cold bluff body flow. The radial profiles of the mean radial velocity for three different grids, i.e., 64×64, 128×128, and 256×256, are compared with the experimental measurements [75].

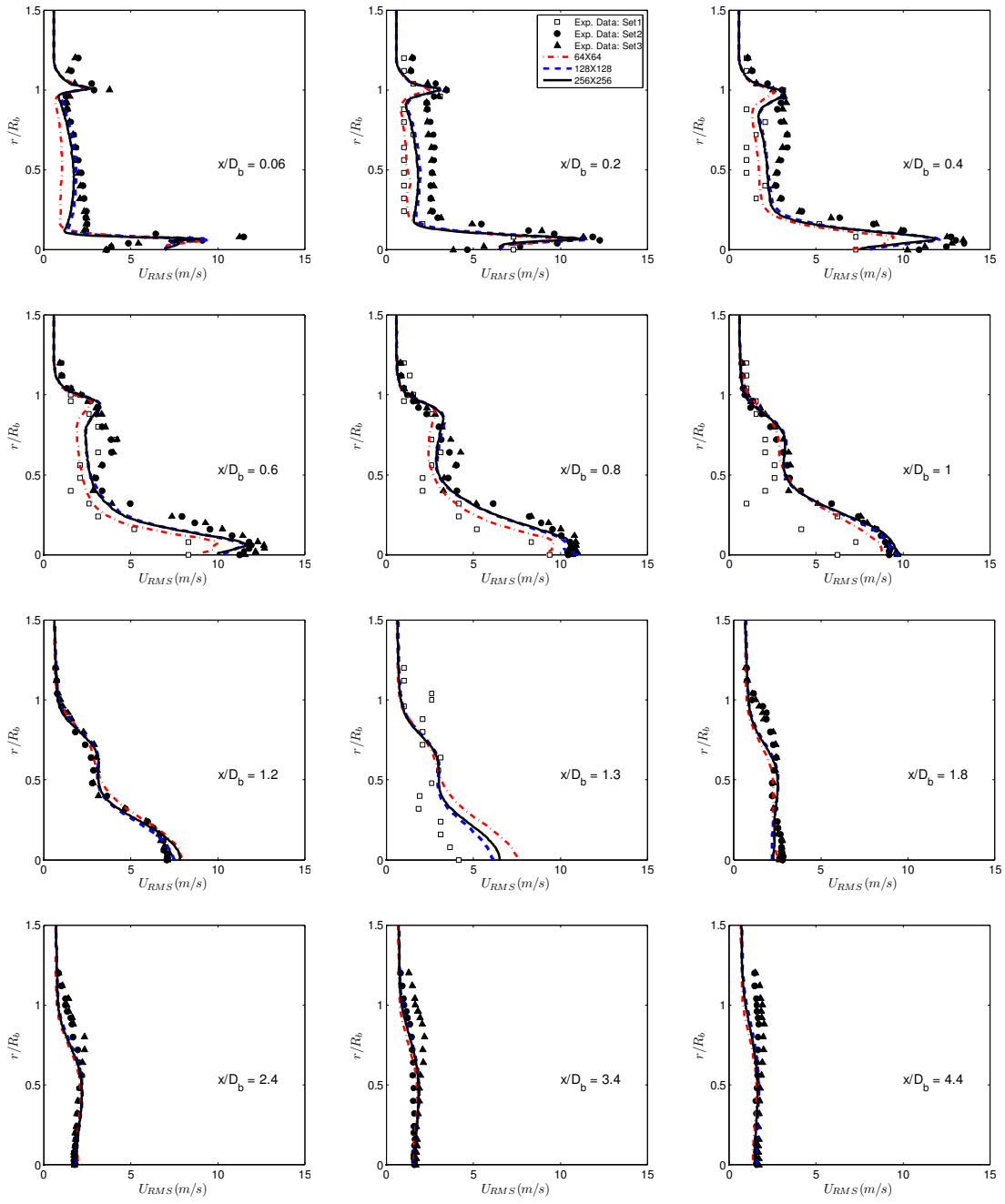


Figure A.3: Grid convergence for the cold bluff body flow. The radial profiles of the rms axial velocity for three different grids, i.e., 64×64, 128×128, and 256×256, are compared with the experimental measurements [75].

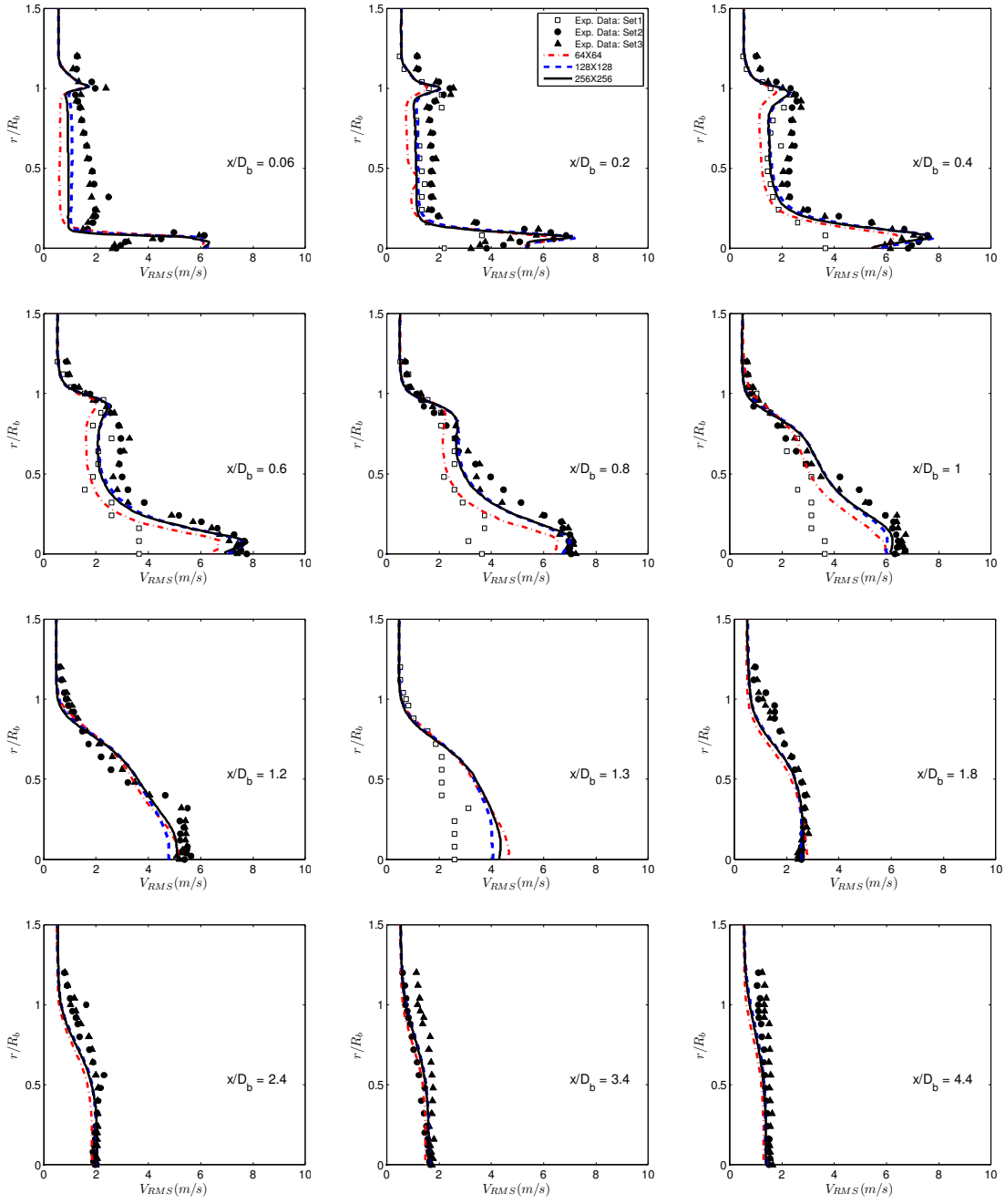


Figure A.4: Grid convergence for the cold bluff body flow. The radial profiles of the rms radial velocity for three different grids, i.e., 64×64, 128×128, and 256×256, are compared with the experimental measurements [75].

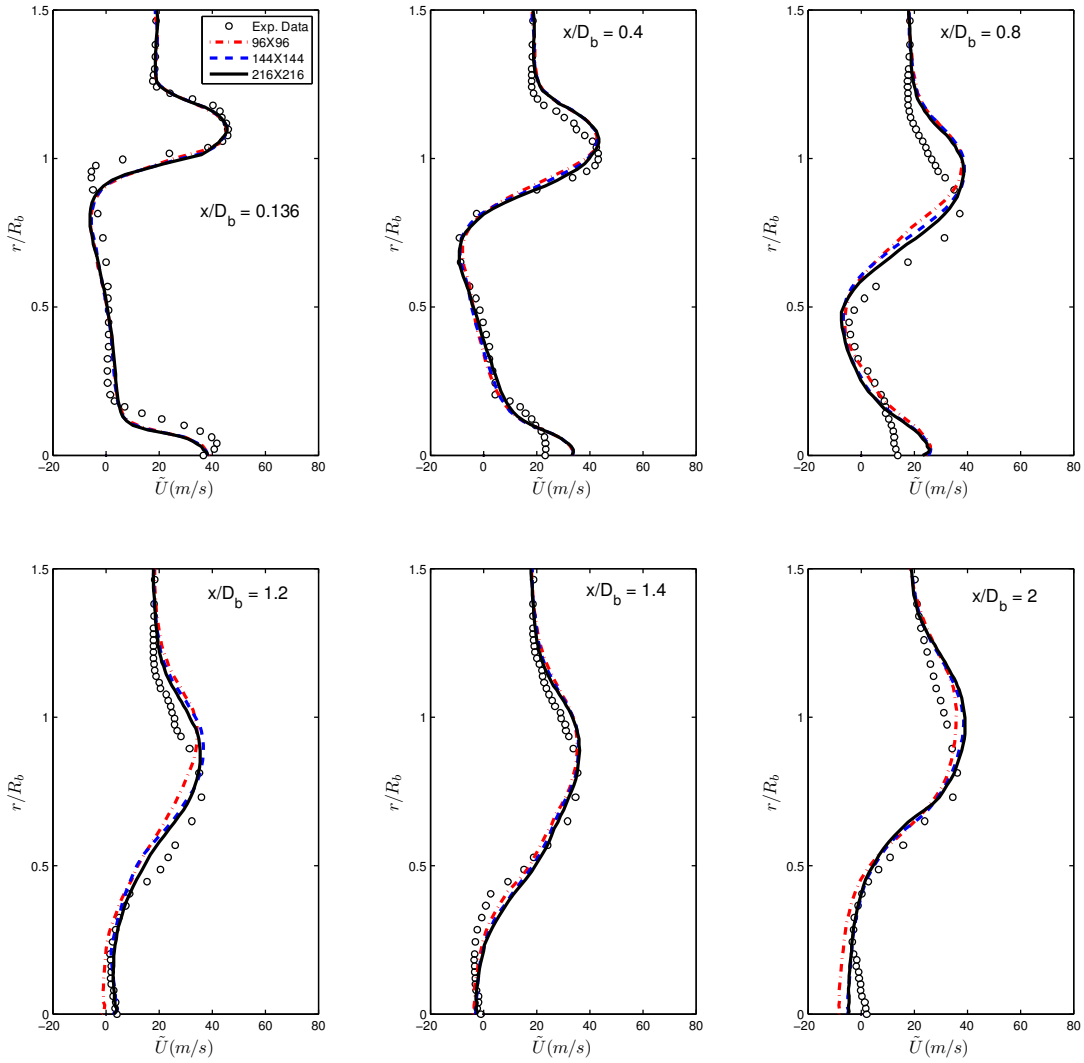


Figure A.5: Grid convergence for the swirling flame 'SM1'. The radial profiles of the mean axial velocity for three different grids, i.e., 96×96, 144×144, and 216×216, are compared with the experimental measurements [75].

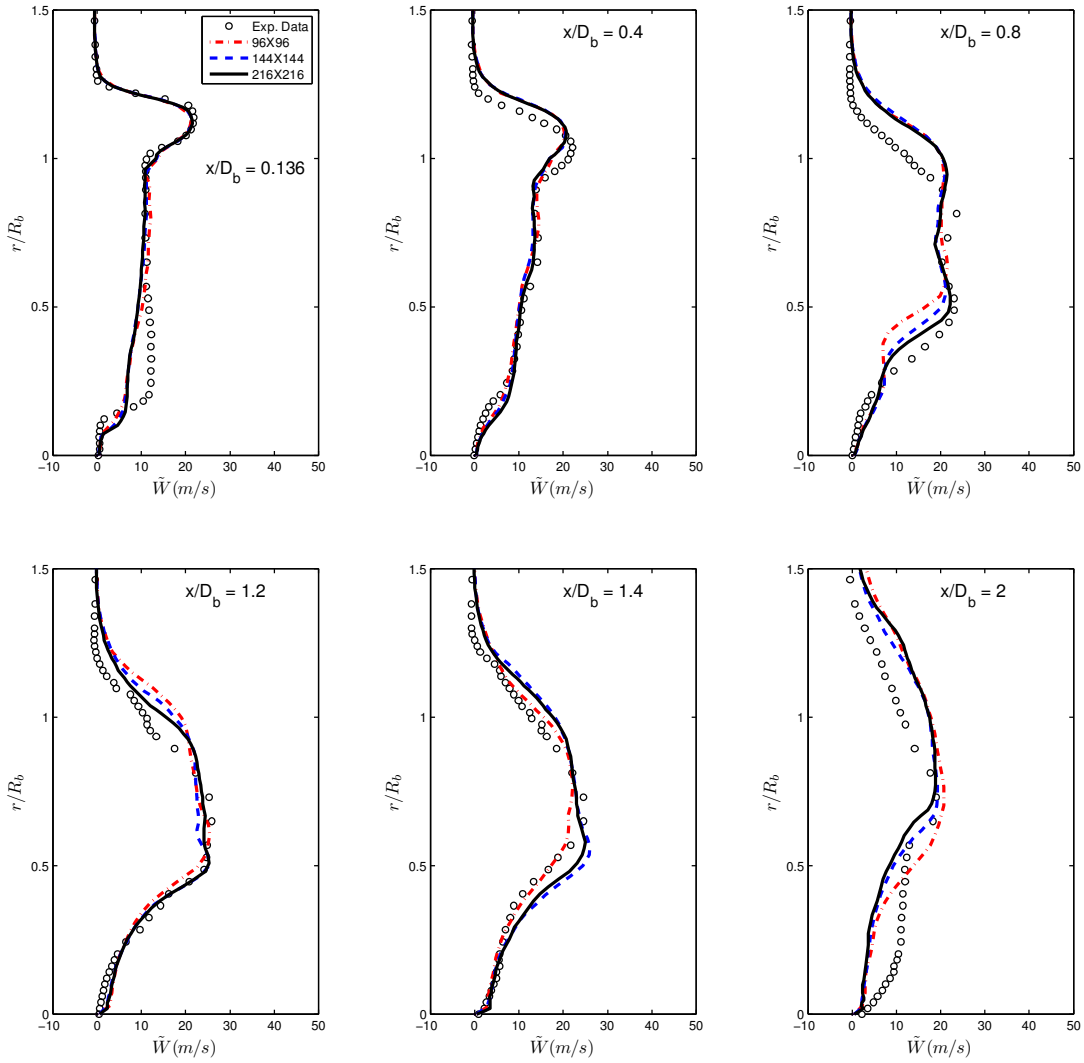


Figure A.6: Grid convergence for the swirling flame 'SM1'. The radial profiles of the mean tangential velocity for three different grids, i.e., 96×96, 144×144, and 216×216, are compared with the experimental measurements [75].

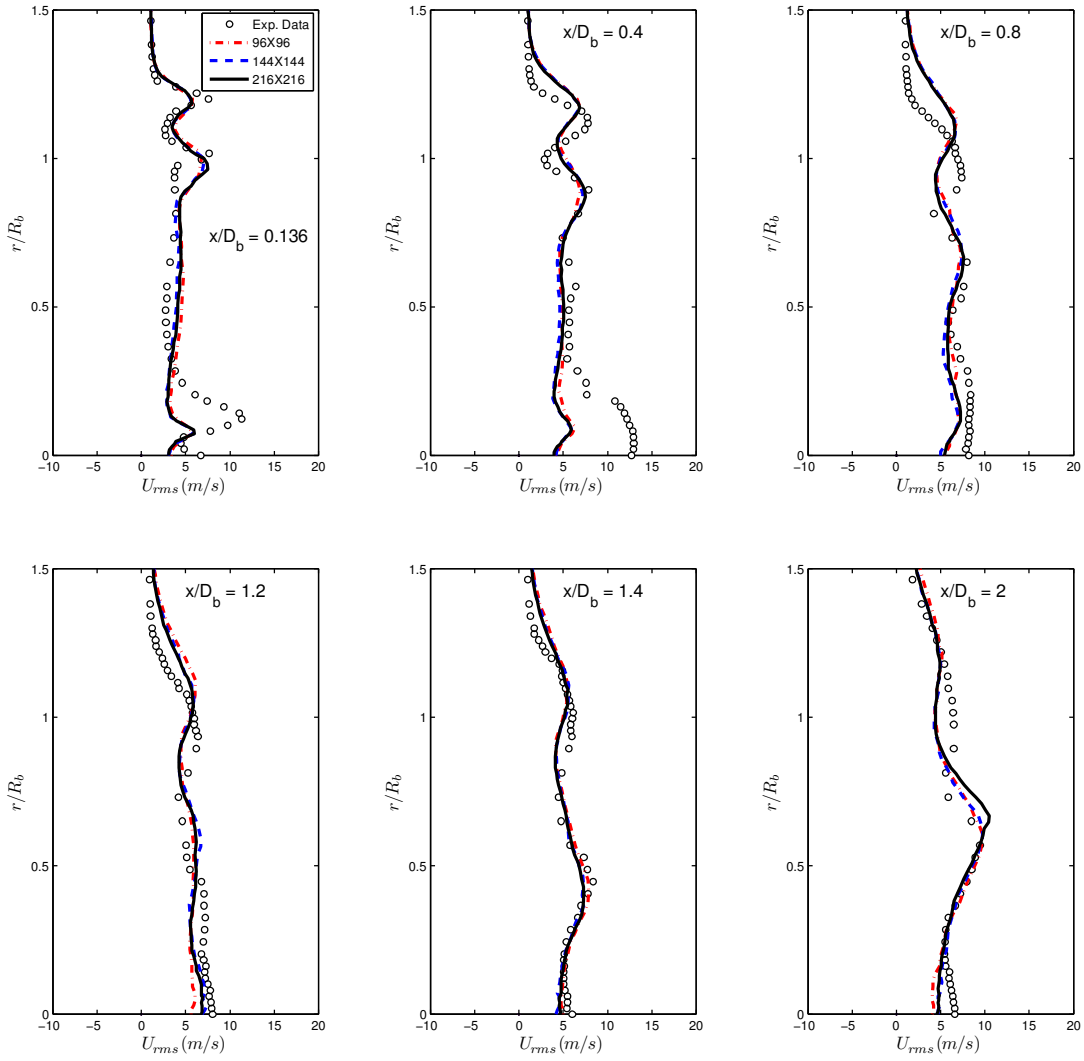


Figure A.7: Grid convergence for the swirling flame 'SM1'. The radial profiles of the rms axial velocity for three different grids, i.e., 96×96, 144×144, and 216×216, are compared with the experimental measurements [75].

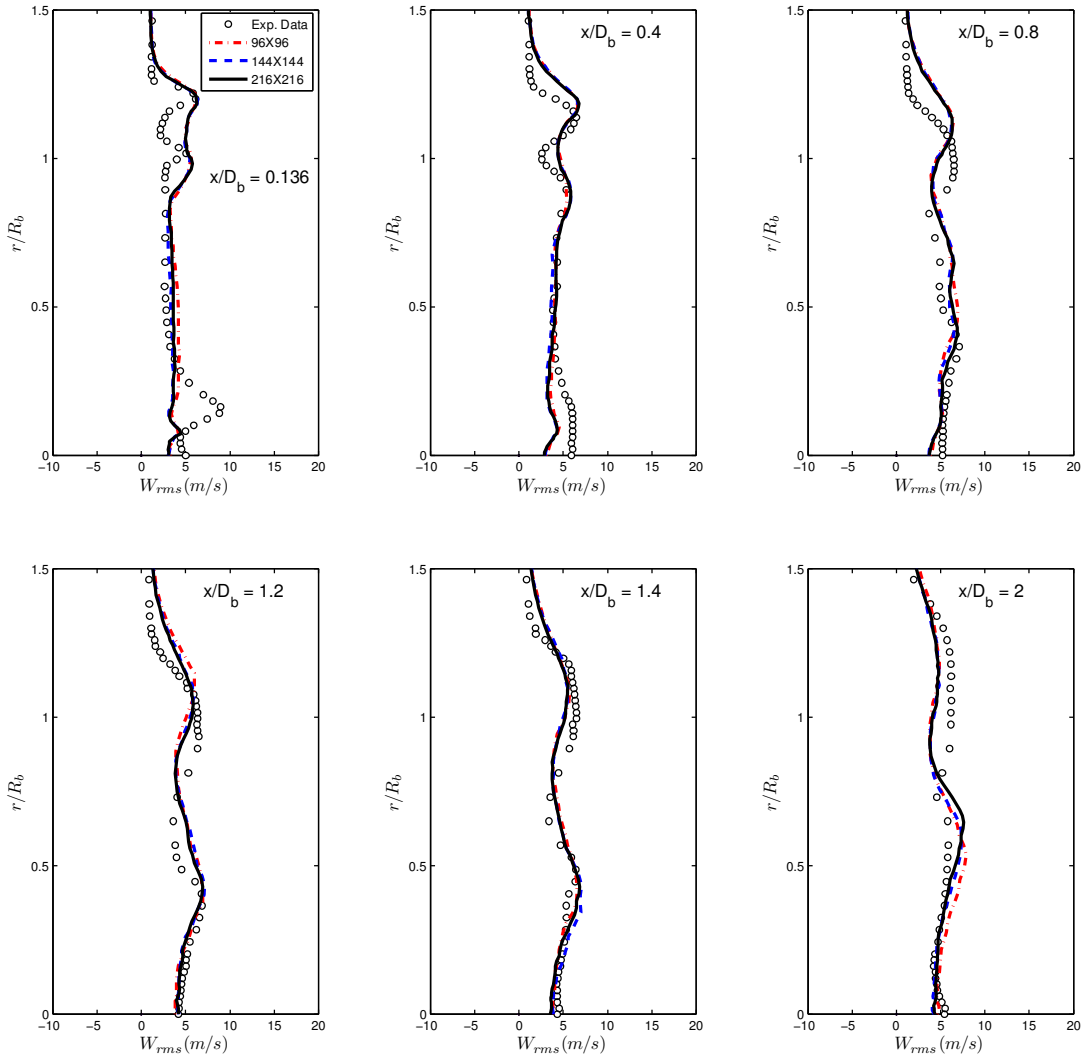


Figure A.8: Grid convergence for the swirling flame 'SM1'. The radial profiles of the rms tangential velocity for three different grids, i.e., 96×96, 144×144, and 216×216, are compared with the experimental measurements [75].

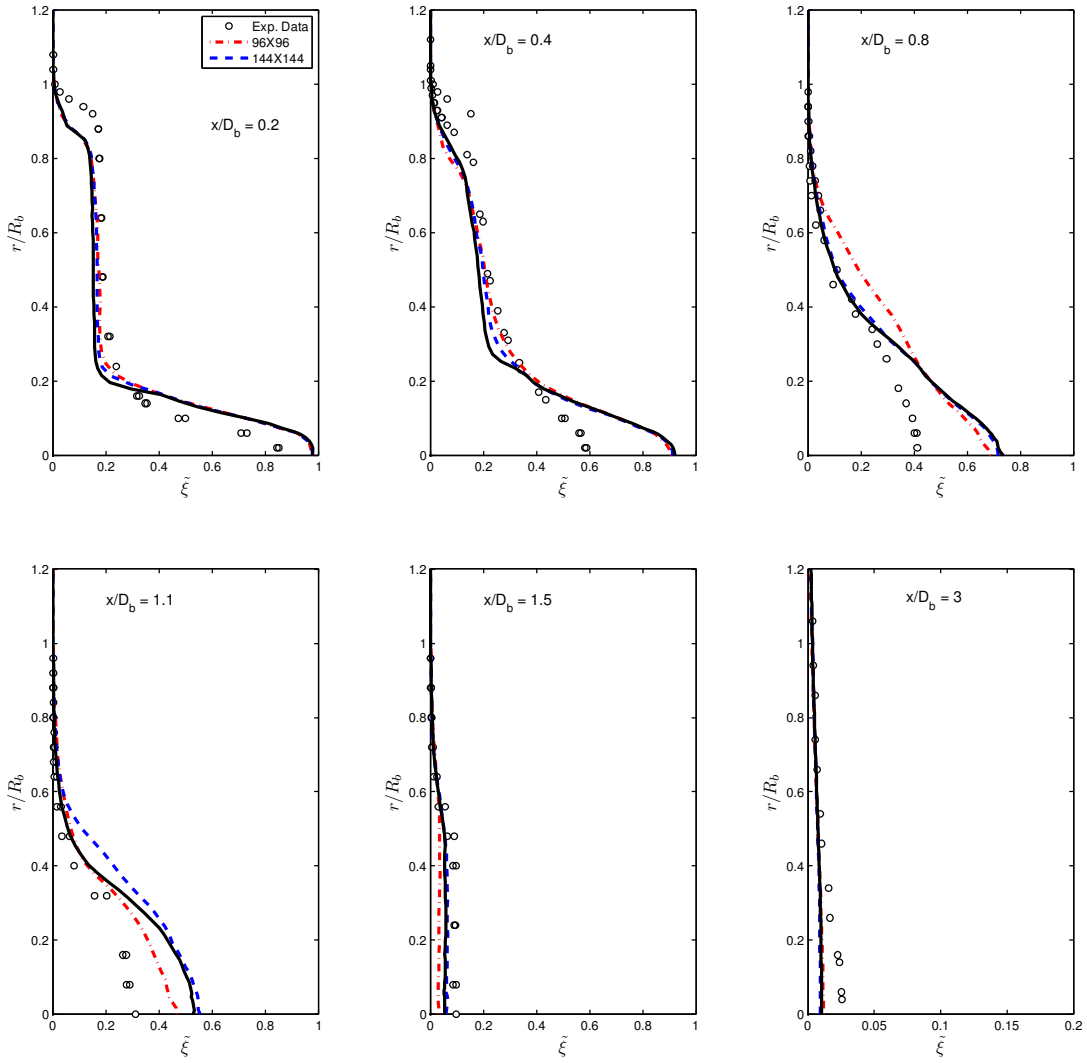


Figure A.9: Grid convergence for the swirling flame 'SM1'. The radial profiles of the mean mixture fraction for three different grids, i.e., 96×96, 144×144, and 216×216, are compared with the experimental measurements [75].

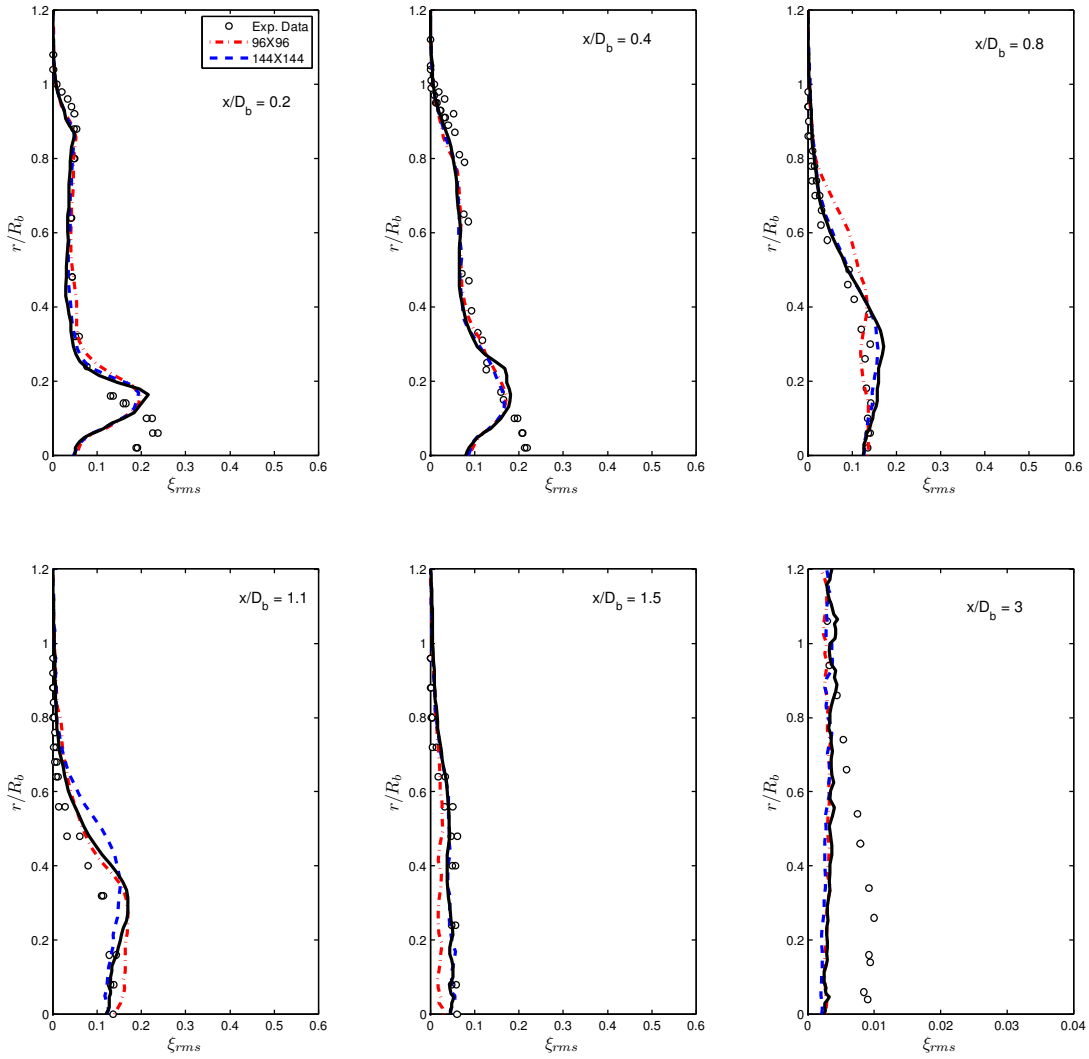


Figure A.10: Grid convergence for the swirling flame 'SM1'. The radial profiles of the rms mixture fraction for three different grids, i.e., 96×96, 144×144, and 216×216, are compared with the experimental measurements [75].

Appendix B

Model Equations in the Cylindrical Coordinate System

Normally model equations are written in the Cartesian coordinate system. Since our method solves axisymmetric flows, model equations must also be solved in the cylindrical coordinate system which introduces new terms in model equations. In this appendix the model equations for velocity, turbulent frequency, and mixing are derived in the cylindrical coordinate system.

B.1 Velocity Model

In the simplified Langevin model (SLM) [48, 17] the fluctuating velocity is written in Cartesian coordinate system as

$$du_i = \underbrace{\frac{1}{\langle\rho\rangle}\frac{\partial\left(\langle\rho\rangle\widetilde{u_i u_j}\right)}{\partial x_j}}_{(I)}dt - \underbrace{u_j\frac{\partial\tilde{U}_i}{\partial x_j}}_{(II)}dt - \left(\frac{1}{2}+\frac{3}{4}C_0\right)\Omega u_i(t)dt + \left(C_0\tilde{k}\Omega\right)^{1/2}d\mathcal{W}_i. \quad \text{(B.1)}$$

The term (I) in Eq. (B.1) can be written as

$$\frac{1}{\langle\rho\rangle} Div\mathbf{R}$$

If tensor $\mathbf{R}$ be

$$\mathbf{R} = \begin{pmatrix} \langle\rho\rangle\widetilde{u_z u_z} & \langle\rho\rangle\widetilde{u_z u_r} & \langle\rho\rangle\widetilde{u_z u_\theta} \\ \langle\rho\rangle\widetilde{u_r u_z} & \langle\rho\rangle\widetilde{u_r u_r} & \langle\rho\rangle\widetilde{u_r u_\theta} \\ \langle\rho\rangle\widetilde{u_\theta u_z} & \langle\rho\rangle\widetilde{u_\theta u_r} & \langle\rho\rangle\widetilde{u_\theta u_\theta}, \end{pmatrix} \tag{B.2}$$

Then the divergence of $\mathbf{R}$ will be

$$\begin{aligned} Div\mathbf{R} = &\left[\frac{\partial}{\partial z}\left(\langle\rho\rangle\widetilde{u_z u_z}\right) + \frac{\partial}{\partial r}\left(\langle\rho\rangle\widetilde{u_z u_r}\right) + \frac{1}{r}\left(\langle\rho\rangle\widetilde{u_z u_r}\right)\right]\mathbf{e_z} \\ + &\left[\frac{\partial}{\partial z}\left(\langle\rho\rangle\widetilde{u_z u_r}\right) + \frac{\partial}{\partial r}\left(\langle\rho\rangle\widetilde{u_r u_r}\right) + \frac{1}{r}\left(\langle\rho\rangle\widetilde{u_r u_r} - \langle\rho\rangle\widetilde{u_\theta u_\theta}\right)\right]\mathbf{e_r} + \\ &\left[\frac{\partial}{\partial z}\left(\langle\rho\rangle\widetilde{u_z u_\theta}\right) + \frac{\partial}{\partial r}\left(\langle\rho\rangle\widetilde{u_r u_\theta}\right) + \frac{2}{r}\left(\langle\rho\rangle\widetilde{u_r u_\theta}\right)\right]\mathbf{e}_\theta. \end{aligned} \tag{B.3}$$

The term (II) in Eq. (2.36) can be written as:

$$(\mathbf{u}\cdot\nabla)\tilde{\mathbf{U}} = \left(u_z\frac{\partial}{\partial z} + u_r\frac{\partial}{\partial r} + \frac{1}{r}u_\theta\frac{\partial}{\partial\theta}\right)\tilde{\mathbf{U}}. \tag{B.4}$$

The standard Cartesian and cylindrical coordinate systems are shown in Fig. B.1 Let (X, Y, Z) and (r, θ, z) be the standard Cartesian and cylindrical coordinates, respectively. The corresponding unit vectors in the Cartesian and cylindrical coordinates are denoted by $(\mathbf{e}_X, \mathbf{e}_Y, \mathbf{e}_Z)$ and $(\mathbf{e}_r, \mathbf{e}_\theta, \mathbf{e}_z,)$ as shown in Fig. B.1. First and second order tensors are represented by suffix notation and by using the unit vectors. The

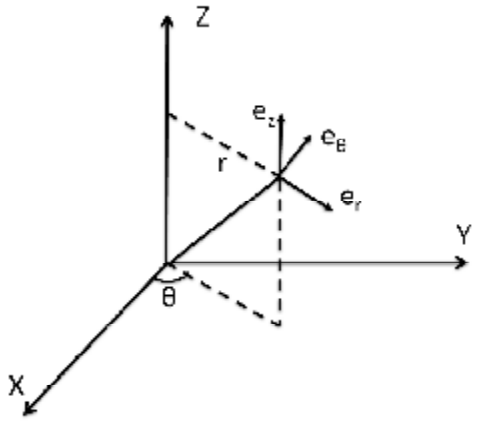


Figure B.1: Standard cylindrical coordinate system

unit vectors in Cartesian and cylindrical coordinates are related as

$$\begin{aligned} \mathbf{e}_r &= \mathbf{e}_X \cos\theta + \mathbf{e}_Y \sin\theta, \\ \mathbf{e}_\theta &= -\mathbf{e}_X \sin\theta + \mathbf{e}_Y \cos\theta, \\ \mathbf{e}_z &= \mathbf{e}_Z, \end{aligned} \tag{B.5}$$

and

$$\begin{aligned} \mathbf{e}_X &= \mathbf{e}_r \cos\theta - \mathbf{e}_\theta \sin\theta, \\ \mathbf{e}_Y &= \mathbf{e}_r \sin\theta + \mathbf{e}_\theta \cos\theta, \\ \mathbf{e}_Z &= \mathbf{e}_z. \end{aligned} \tag{B.6}$$

We can easily deduce from Eq. (B.5) that

$$\begin{aligned} \frac{\partial \mathbf{e}_r}{\partial\theta} &= \mathbf{e}_\theta, \\ \frac{\partial \mathbf{e}_\theta}{\partial\theta} &= -\mathbf{e}_r, \\ \frac{\partial \mathbf{e}_r}{\partial r} &= \frac{\partial \mathbf{e}_r}{\partial z} = \frac{\partial \mathbf{e}_\theta}{\partial r} = \frac{\partial \mathbf{e}_\theta}{\partial z} = \frac{\partial \mathbf{e}_z}{\partial r} = \frac{\partial \mathbf{e}_z}{\partial\theta} = \frac{\partial \mathbf{e}_z}{\partial z} = 0. \end{aligned} \tag{B.7}$$

Let $\mathbf{U}$ and $\mathbf{A}$ be a first and second order tensors, i.e.,

$$\begin{aligned}
\mathbf{U} &= U_X\mathbf{e}_X + U_Y\mathbf{e}_Y + U_Z\mathbf{e}_Z = U_r\mathbf{e}_r + U_\theta\mathbf{e}_\theta + U_z\mathbf{e}_z, \\
\mathbf{A} &= \mathbf{e}_X\mathbf{e}_X A_{XX} + \mathbf{e}_X\mathbf{e}_Y A_{XY} + \mathbf{e}_X\mathbf{e}_Z A_{XZ} \\
&+ \mathbf{e}_Y\mathbf{e}_X A_{YX} + \mathbf{e}_Y\mathbf{e}_Y A_{YY} + \mathbf{e}_Y\mathbf{e}_Z A_{YZ} \\
&+ \mathbf{e}_Z\mathbf{e}_X A_{ZX} + \mathbf{e}_Z\mathbf{e}_Y A_{ZY} + \mathbf{e}_Z\mathbf{e}_Z A_{ZZ} \\
&= \mathbf{e}_z\mathbf{e}_z A_{zz} + \mathbf{e}_z\mathbf{e}_r A_{zr} + \mathbf{e}_z\mathbf{e}_\theta A_{z\theta} \\
&+ \mathbf{e}_r\mathbf{e}_z A_{rz} + \mathbf{e}_r\mathbf{r} A_{rr} + \mathbf{e}_r\mathbf{e}_\theta A_{r\theta} \\
&+ \mathbf{e}_\theta\mathbf{e}_z A_{\theta z} + \mathbf{e}_\theta\mathbf{e}_r A_{\theta r} + \mathbf{e}_\theta\mathbf{e}_\theta A_{\theta\theta}.
\end{aligned} \tag{B.8}$$

The Gradient operator is defined as

$$\begin{aligned}
\nabla() &= \mathbf{e}_X\frac{\partial}{\partial X} + \mathbf{e}_Y\frac{\partial}{\partial Y} + \mathbf{e}_Z\frac{\partial}{\partial Z} \\
&= \mathbf{e}_r\frac{\partial}{\partial r} + \mathbf{e}_\theta\frac{1}{r}\frac{\partial}{\partial\theta} + \mathbf{e}_z\frac{\partial}{\partial z}.
\end{aligned} \tag{B.9}$$

Now we can have

$$
\begin{aligned}
(\mathbf{u}\cdot\nabla)\tilde{\mathbf{U}} &= \left(u_z\frac{\partial}{\partial z}+u_r\frac{\partial}{\partial r}+\frac{u_\theta}{r}\frac{\partial}{\partial\theta}\right)\left(\tilde{U}_z\mathbf{e}_z+\tilde{U}_r\mathbf{e}_r+\tilde{U}_\theta\mathbf{e}_\theta\right)\\
&= \left(u_z\frac{\partial\tilde{U}_z\mathbf{e}_z}{\partial z}+u_r\frac{\partial\tilde{U}_z\mathbf{e}_z}{\partial r}+\frac{u_\theta}{r}\frac{\partial\tilde{U}_z\mathbf{e}_z}{\partial\theta}\right)\\
&+ \left(u_z\frac{\partial\tilde{U}_r\mathbf{e}_r}{\partial z}+u_r\frac{\partial\tilde{U}_r\mathbf{e}_r}{\partial r}+\frac{u_\theta}{r}\frac{\partial\tilde{U}_r\mathbf{e}_r}{\partial\theta}\right)\\
&+ \left(u_z\frac{\partial\tilde{U}_\theta\mathbf{e}_\theta}{\partial z}+u_r\frac{\partial\tilde{U}_\theta\mathbf{e}_\theta}{\partial r}+\frac{u_\theta}{r}\frac{\partial\tilde{U}_\theta\mathbf{e}_\theta}{\partial\theta}\right)\\
&= \left(\mathbf{e_z}u_z\frac{\partial\tilde{U}_z}{\partial z}+\mathbf{e_z}u_r\frac{\partial\tilde{U}_z}{\partial r}+\mathbf{e_z}\frac{u_\theta}{r}\frac{\partial\tilde{U}_z}{\partial\theta}\right)\\
&+ \left(\mathbf{e_r}u_z\frac{\partial\tilde{U}_r}{\partial z}+\mathbf{e_r}u_r\frac{\partial\tilde{U}_r}{\partial r}+\left\{\mathbf{e_r}\frac{u_\theta}{r}\frac{\partial\tilde{U}_r}{\partial\theta}+\frac{u_\theta\tilde{U}_r}{r}\frac{\partial\mathbf{e_r}}{\partial\theta}\right\}\right)\\
&+ \left(\mathbf{e}_\theta u_z\frac{\partial\tilde{U}_\theta}{\partial z}+\mathbf{e}_\theta u_r\frac{\partial\tilde{U}_\theta}{\partial r}+\left\{\frac{\mathbf{e}_\theta u_\theta}{r}\frac{\partial\tilde{U}_\theta}{\partial\theta}+\frac{u_\theta\tilde{U}_\theta}{r}\frac{\partial\mathbf{e}_\theta}{\partial\theta}\right\}\right)\\
&= \left(\mathbf{e}_z u_z\frac{\partial\tilde{U}_z}{\partial z}+\mathbf{e}_z u_r\frac{\partial\tilde{U}_z}{\partial r}+\mathbf{e}_x\frac{u_\theta}{r}\frac{\partial\tilde{U}_z}{\partial\theta}\right)\\
&+ \left(\mathbf{e}_r u_z\frac{\partial\tilde{U}_r}{\partial z}+\mathbf{e}_r u_r\frac{\partial\tilde{U}_r}{\partial r}+\left\{\mathbf{e}_r\frac{u_\theta}{r}\frac{\partial\tilde{U}_r}{\partial\theta}+\frac{u_\theta\tilde{U}_r}{r}\mathbf{e}_\theta\right\}\right)\\
&+ \left(\mathbf{e}_\theta u_x\frac{\partial\tilde{U}_\theta}{\partial z}+\mathbf{e}_\theta u_r\frac{\partial\tilde{U}_\theta}{\partial r}+\left\{\frac{\mathbf{e}_\theta u_\theta}{r}\frac{\partial\tilde{U}_\theta}{\partial\theta}+\frac{u_\theta\tilde{U}_\theta}{r}(-\mathbf{e}_r)\right\}\right)\\
&= \mathbf{e}_z\left(u_z\frac{\partial\tilde{U}_z}{\partial z}+u_r\frac{\partial\tilde{U}_z}{\partial r}\right)\\
&+ \mathbf{e}_r\left(u_z\frac{\partial\tilde{U}_r}{\partial z}+u_r\frac{\partial\tilde{U}_r}{\partial r}-\frac{u_\theta\tilde{U}_\theta}{r}\right)\\
&+ \mathbf{e}_\theta\left(u_z\frac{\partial\tilde{U}_\theta}{\partial z}+u_r\frac{\partial\tilde{U}_\theta}{\partial r}+\frac{u_\theta\tilde{U}_r}{r}\right). \qquad \text{(B.10)}
\end{aligned}
$$

Here the derivatives with respect to θ are neglected due to axisymmetry. As you can see, there are two additional terms in r and θ directions. In addition, similar terms

also come from the left hand side of the equations:

$$\begin{aligned} d\mathbf{u} &= d(u_r\mathbf{e}_r + u_\theta\mathbf{e}_\theta + u_z\mathbf{e}_z) \\ &= \mathbf{e}_r du_r + u_r d\mathbf{e}_r + \mathbf{e}_\theta du_\theta + u_\theta d\mathbf{e}_\theta + \mathbf{e}_z du_z + u_z d\mathbf{e}_z. \end{aligned} \tag{B.11}$$

On the other hand,

$$\begin{aligned} d\mathbf{e}_r &= \left(\frac{\partial \mathbf{e}_r}{\partial t} + \mathbf{U}\cdot\nabla\mathbf{e}_r\right)dt \\ &= \left(0 + U_z\frac{\partial \mathbf{e}_r}{\partial z} + U_r\frac{\partial \mathbf{e}_r}{\partial r} + \frac{U_\theta}{r}\frac{\partial \mathbf{e}_r}{\partial \theta}\right)dt \\ &= \mathbf{e}_\theta\frac{\tilde{U}_\theta + u_\theta}{r}dt \\ d\mathbf{e}_\theta &= \left(\frac{\partial \mathbf{e}_\theta}{\partial t} + \mathbf{U}\cdot\nabla\mathbf{e}_\theta\right)dt \\ &= \left(0 + U_z\frac{\partial \mathbf{e}_\theta}{\partial z} + U_r\frac{\partial \mathbf{e}_\theta}{\partial r} + \frac{U_\theta}{r}\frac{\partial \mathbf{e}_\theta}{\partial \theta}\right)dt \\ &= -\mathbf{e}_r\frac{\tilde{U}_\theta + u_\theta}{r}dt \\ d\mathbf{e}_z &= \left(\frac{\partial \mathbf{e}_z}{\partial t} + \mathbf{U}\cdot\nabla\mathbf{e}_z\right)dt \\ &= 0. \end{aligned} \tag{B.12}$$

Then from Eqs. (B.11) and (B.12), one obtains

$$d\mathbf{u} = \mathbf{e}_r\left(du_r - \frac{u_\theta\tilde{U}_\theta + u_\theta u_\theta}{r}dt\right) + \mathbf{e}_\theta\left(du_\theta + \frac{u_r\tilde{U}_\theta + u_r u_\theta}{r}dt\right) + \mathbf{e}_z du_z. \tag{B.13}$$

Then Eq. (2.36) in the cylindrical coordinate system can be written as

$$
\begin{aligned}
du_z &= \frac{1}{\langle\rho\rangle}\left[\frac{\partial}{\partial z}\langle\rho\rangle\widetilde{u_z u_z} + \frac{\partial}{\partial r}\langle\rho\rangle\widetilde{u_z u_r} + \frac{1}{r}\left(\langle\rho\rangle\widetilde{u_z u_r}\right)\right]dt - \left(u_z\frac{\partial\tilde{U}_z}{\partial z} + u_r\frac{\partial\tilde{U}_z}{\partial r}\right)dt \\
&- \left(\frac{1}{2}+\frac{3}{4}C_0\right)\Omega u_z dt + \left(C_0 k\Omega\right)^{1/2} dW_1, \\
du_r &= \frac{1}{\langle\rho\rangle}\left[\frac{\partial}{\partial z}\langle\rho\rangle\widetilde{u_z u_r} + \frac{\partial}{\partial r}\langle\rho\rangle\widetilde{u_r u_r} + \frac{1}{r}\left(\langle\rho\rangle\widetilde{u_r u_r} - \langle\rho\rangle\widetilde{u_\theta u_\theta}\right)\right]dt - \left(u_z\frac{\partial\tilde{U}_r}{\partial x} + u_r\frac{\partial\tilde{U}_r}{\partial r}\right)dt \\
&+ \left(\frac{2u_\theta\tilde{U}_\theta + u_\theta u_\theta}{r}\right)dt - \left(\frac{1}{2}+\frac{3}{4}C_0\right)\Omega u_r dt + \left(C_0 k\Omega\right)^{1/2} dW_2, \\
du_\theta &= \frac{1}{\langle\rho\rangle}\left[\frac{\partial}{\partial z}\langle\rho\rangle\widetilde{u_z u_\theta} + \frac{\partial}{\partial r}\langle\rho\rangle\widetilde{u_r u_\theta} + \frac{2}{r}\left(\langle\rho\rangle\widetilde{u_r u_\theta}\right)\right]dt - \left(u_x\frac{\partial\tilde{U}_\theta}{\partial z} + u_r\frac{\partial\tilde{U}_\theta}{\partial r}\right)dt \\
&- \left(\frac{u_r\tilde{U}_\theta + u_\theta\tilde{U}_r + u_r u_\theta}{r}\right)dt - \left(\frac{1}{2}+\frac{3}{4}C_0\right)\Omega u_\theta dt + \left(C_0 k\Omega\right)^{1/2} dW_3. \qquad \text{(B.14)}
\end{aligned}
$$

B.2 Turbulent Frequency Model

Turbulent frequency model which is used is modified Jayesh-Pope model [67] which can be written in the Cartesian coordinate system is as

$$
d\omega(t) = -C_3\left(\omega - \tilde{\omega}\right)\Omega dt - S_\omega\Omega\omega(t)dt + \left(2C_3C_4\tilde{\omega}\Omega\omega\left(t\right)\right)^{1/2} d\mathcal{W}, \qquad \text{(B.15)}
$$

in Eq. (B.15) the source term S_ω is defined as

$$
S_\omega = C_{\omega 2} - C_{\omega 1}\frac{\mathcal{P}}{\tilde{k}\Omega}, \qquad \text{(B.16)}
$$

where $\mathcal{P} = -\widetilde{u_i u_j}\frac{\partial \tilde{U}_i}{\partial x_j}$ is the turbulence production. In the cylindrical coordinate system the term $\frac{\partial \tilde{U}_i}{\partial x_j}$ in $\mathcal{P}$ can be written as

$$\begin{aligned}
\left(\frac{\partial}{\partial z}\mathbf{e}_z + \frac{\partial}{\partial r}\mathbf{e}_r + \frac{1}{r}\frac{\partial}{\partial \theta}\mathbf{e}_\theta\right)\left(\tilde{U}_z\mathbf{e}_z + \tilde{U}_r\mathbf{e}_r + \tilde{U}_\theta\mathbf{e}_\theta\right) &= \\
\frac{\partial \tilde{U}_z}{\partial z}\mathbf{e}_z\mathbf{e}_z + \frac{\partial \tilde{U}_z}{\partial r}\mathbf{e}_z\mathbf{e}_r + \frac{1}{r}\frac{\partial \tilde{U}_z}{\partial \theta}\mathbf{e}_z\mathbf{e}_\theta + & \\
\frac{\partial \tilde{U}_r}{\partial z}\mathbf{e}_r\mathbf{e}_z + \frac{\partial \tilde{U}_r}{\partial r}\mathbf{e}_r\mathbf{e}_r + \frac{1}{r}\frac{\partial \tilde{U}_r}{\partial \theta}\mathbf{e}_r\mathbf{e}_\theta + & \\
\frac{\partial \tilde{U}_\theta}{\partial z}\mathbf{e}_\theta\mathbf{e}_z + \frac{\partial \tilde{U}_\theta}{\partial r}\mathbf{e}_\theta\mathbf{e}_r + \frac{1}{r}\frac{\partial \tilde{U}_\theta}{\partial \theta}\mathbf{e}_\theta\mathbf{e}_\theta &= \\
\frac{\partial \tilde{U}_z}{\partial z}\mathbf{e}_z\mathbf{e}_z + \frac{\partial \tilde{U}_z}{\partial r}\mathbf{e}_z\mathbf{e}_r + & \\
\frac{\partial \tilde{U}_r}{\partial z}\mathbf{e}_r\mathbf{e}_z + \frac{\partial \tilde{U}_r}{\partial r}\mathbf{e}_r\mathbf{e}_r + & \\
\frac{\partial \tilde{U}_\theta}{\partial z}\mathbf{e}_\theta\mathbf{e}_z + \frac{\partial \tilde{U}_\theta}{\partial r}\mathbf{e}_\theta\mathbf{e}_r. &
\end{aligned} \tag{B.17}$$

So the turbulence production $\mathcal{P}$ in the cylindrical coordinate system will be

$$\begin{aligned}
\mathcal{P} = -\widetilde{u_z u_z}\frac{\partial \tilde{U}_z}{\partial z}\mathbf{e}_z\mathbf{e}_z - \widetilde{u_z u_r}\frac{\partial \tilde{U}_z}{\partial r}\mathbf{e}_z\mathbf{e}_r & \\
-\widetilde{u_r u_z}\frac{\partial \tilde{U}_r}{\partial z}\mathbf{e}_r\mathbf{e}_z - \widetilde{u_r u_r}\frac{\partial \tilde{U}_r}{\partial r}\mathbf{e}_r\mathbf{e}_r & \\
-\widetilde{u_\theta u_z}\frac{\partial \tilde{U}_\theta}{\partial z}\mathbf{e}_\theta\mathbf{e}_z - \widetilde{u_\theta u_r}\frac{\partial \tilde{U}_\theta}{\partial r}\mathbf{e}_\theta\mathbf{e}_r. &
\end{aligned} \tag{B.18}$$

B.3 Mixing and Combustion Model

For modeling combustion a simple flamelet mode is used. For micro-mixing the IEM model [9] is applied. This model can be written as following, which is the same for any coordinate system

$$\frac{d\mathbf{\Phi}}{dt} = -\frac{1}{2}C_\phi\Omega(\mathbf{\Phi} - \tilde{\mathbf{\Phi}}). \tag{B.19}$$

Appendix C

The ARM2 Augmented Reduced Chemistry Mechanism

In this appendix, some details of the ARM2 chemistry mechanism are presented. The augmented reduced mechanism ARM2 has been derived from the GRI2.11 mechanism [73] (with 276 reactions of 49 species) by Sung et al. [61]. The first version, namely, ARM1 [62], includes 16 species and 12 reaction steps. The ARM1 mechanism is extended by inclusion of a description for NOx formation, which results in an augmented reduced mechanism of 19 species with 15 reaction steps that is given in Table C.1. The global reaction rates and the corresponding steady-state relations for the ARM2 mechanism can be found in [61].

Table C.1: The global reactions for ARM2 reduced mechanism [61].

CH4 + H	=	CH3 + H2	(R1)
CH3 + OH	=	CH2O + H2	(R2)
CH2O	=	CO + H2	(R3)
C2H6	=	C2H4 + H2	(R4)
C2H4 + OH	=	CH3 + CO + H2	(R5)
C2H2 + O2	=	2CO + H2	(R6)
CO + OH + H	=	CO2 + H2	(R7)
H + OH	=	H2O	(R8)
2H2 + O2	=	2H + 2OH	(R9)
2H	=	H2	(R10)
HO2 + H	=	H2 + O2	(R11)
H2O2 + H	=	H2 + HO2	(R12)
N2 + O2	=	2NO	(R13)
HCN + H + O2	=	H2 + CO + NO	(R14)
NH3 + 3H	=	H2O + 4H2 + NO	(R15)

Bibliography

[1] Y. M. Al-Abdeli and A. R. Masri, "Stability characteristics and flow fields of turbulent non-premixed swirling flames", *Combust. Theor. Model.*, **7**:731–766 (2003).

[2] Y. M. Al-Abdeli and A. R. Masri, "Recirculation and flowfield regimes of unconfined non-reacting swirling flows", *Exp. Therm. Fluid Sci.*, **27**:655–665 (2003).

[3] R. S. Barlow, International workshop on measurement and computation of turbulent non-premixed flames (TNF), http://www.ca.sandia.gov/TNF.

[4] R. W. Bilger, S. H. Starner and R. J. Kee, "On reduced mechanisms for methane-air combustion in non-premixed flames", *Combust. Flame*, **80**:135–149 (1990).

[5] R. Cao, H. Wang and S. B. Pope, "The effect of mixing models in PDF calculations of piloted jet flames", *Proc. Combust. Inst.*, **31**:1543–1550 (2007).

[6] B. B. Dally, A. R. Masri, R. S. Barlow and G. J. Fiechtner, "Instantaneous and mean compositional structure of bluff-body stabilized non-premixed flames", *Combust. Flame*, **114**:119–148 (1998).

[7] B. B. Dally, D. F. Fletcher and A. R. Masri, "Flow and mixing fields of turbulent bluff-body jets and flames", *Combust. Theor. Model.*, **2**:193–219 (1998).

[8] R. De Meester, B. Naud, U. Maas and B. Merci, "Transported scalar PDF calculations of a swirling bluff-body flame ('SM1') with a reaction diffusion manifold", *Combust. Flame*, **159**:2415–2429 (2012).

[9] C. Dopazo and E. E. OBrien, "An approach to the autoignition of a turbulent mixture", *Acta Astronaut*, **1**:1239–1266 (1974).

[10] D. L. Darmofal and P. J. Schmid, "The importance of eigenvectors for local preconditioners of the Euler equations", *J. Comput. Phys.*, **127**:346–362 (1996).

[11] T. D. Dreeben and S. B. Pope, "Nonparametric estimation of mean fields with application to particle methods for turbulent flows", Technical Report FDA, 92–13, Cornell University (1992).

[12] H. El-Asrag and S. Menon, "Large eddy simulation of a swirling non-premixed flame", *AIAA*, **41**:1–15 (2005).

[13] P. Givi, "Model free simulations of turbulent reactive flows", *Prog. Energy Combust. Sci.*, **15**:1–107 (1989).

[14] H. Guillard and C. Viozat, "On the behaviour of upwind schemes in the low Mach number limit", *Computers & Fluids*, **28**:63–86 (1999).

[15] R. W. Hockney and J. W. Eastwood, "Computer simulations using particles", Adam Hilger, NewYork (1988).

[16] D. C. Haworth, "Progress in probability density function methods for turbulent reacting flows", *Prog. Energy Combust. Sci.* **36**:168–259 (2010).

[17] D. C. Haworth and S. B. Pope, "A generalized Langevin model for turbulent flows", *Phys. Fluids.*, **29**:387–405 (1986).

[18] R. I. Issa, "Solution of the implicitly discretized fluid flow equations by operator splitting", *J. Comput. Phys.*, **62**:40–65 (1986).

[19] J. Janicka, W. Kolbe and W. J. Kollman, "Closure of the transport equation for the pdf of turbulent scalar fields", *J. Non-equilib. Thermodyn.*, **4**:47–66 (1979).

[20] P. Jenny, S. B. Pope, M. Muradoglu and D. A. Caughey, "A hybrid algorithm for the joint PDF equation for turbulent reactive flows", *J. Comput. Phys.* **166**:218–252 (2001).

[21] P. Jenny, M. Muradoglu, K. Liu, S. B. Pope and D. A. Caughey, "PDF simulations of a bluff-body stabilized flow", *J. Comput. Phys.*, **169**:1–23 (2001).

[22] P. A. M. Kalt, Y. M. Al-Abdeli, A. R. Masri and R. S. Barlow, "Swirling turbulent non-premixed flames of methane: flow field and compositional structure", *Proc. Combust. Inst.*, **29**:1913–1917 (2002).

[23] S.H. Lam and D. A. Goussis, "Understanding complex chemical kinetics with computational singular perturbation", *Proc. Combust. Inst.*, **22**:931–941 (1988).

[24] P. A. Libby and F. A. Williams, "Fundamental aspects and a review", in *Turbulent reacting flows*, P. A. Libby and F. A. Williams (eds), Academic press, London, pp. 1–61 (1994).

[25] K. Liu, D. A. Caughey and S. B. Pope, "Calculations of bluff-body stabilized flames using a joint probability density function model with detailed chemistry", *Combust. Flame*, **141**:89–117 (2005).

[26] U. A. Maas and S. B. Pope, "Laminar flame calculations using simplified chemical kinetics based on intrinsic low-dimensional manifolds", *Proc. Combust. Inst.*, **25**:1349–1356 (1992).

[27] U. A. Maas and S. B. Pope, "Simplifying chemical kinetics: intrinsic low-dimensional manifolds in composition space", *Combust. Flame*, **88**:239–264 (1992).

[28] U. A. Maas and S. B. Pope, "Implementation of simplified chemical kinetics based on intrinsic low-dimensional manifolds", *Proc. Combust. Inst.*, **24**:103–112 (1992).

[29] W. Malalasekera, K. K. J. Ranga Dinesh, S. S. Ibrahim and M. P. Kirkpatrick, "LES of recirculation and vortex breakdown in swirling flames ", *Combust. Sci. Tech.*, **180**:809–832 (2007).

[30] W. Malalasekera, K. K. J. Ranga Dinesh, S. S. Ibrahim and M. P. Kirkpatrick, "Large eddy simulation of isothermal turbulent swirling jets", *Combust. Sci. Tech.*, **179**:1488–1525 (2007).

[31] A. R. Masri, P. A. M. Kalt and R. S. Barlow, "The compositional structure of swirl-stabilized turbulent non-premixed flames", *Combust. Flame*, **137**:1–37 (2004).

[32] A. R. Masri, S. B. Pope and B. B. Dally, "Probability density function computations of strongly swirling non-premixed flame stabilized on a new burner", *Proc. of Combust. Inst.*, **28**:123–131 (2000).

[33] A. R. Masri, B. B. Dally, R. S. Barlow and C. D. Carter, "The structure of the recirculation zone of a bluff-body combustor", *Proc. Combust. Inst.*, **25**:1301–1307 (1994).

[34] W. Meier, X. Duan and P. Weigand. "Investigations of swirl flames in a gas turbine model combustor: II. Turbulencechemistry interaction", *Combust. Flame*, **144**:225–236 (2006).

[35] D. W. Meyer and P. Jenny, "Micromixing models for turbulent flows", *J. Comput. Phys.*, **228**:1275–1293 (2009).

[36] D. W. Meyer and P. Jenny, "Accurate and computationally efficient mixing models for the simulation of turbulent mixing with PDF methods", *J. Comput. Phys.*, **247**:192–207 (2013).

[37] M. Muradoglu, K. Liu and S. B. Pope, "PDF modeling of a bluff-body stabilized turbulent flame", *Combust. Flame*, **132**:115–137 (2003).

[38] M. Muradoglu and S. B. Pope, "Local time-stepping algorithm for solving probability density function turbulence model equations", *AIAA J.*, **40**:1755–1763 (2002).

[39] M. Muradoglu, S. B. Pope and D. A. Caughey, "The hybrid method for the PDF equations of turbulent reactive flows: consistency conditions and correction algorithms", *J. Comput. Phys.*, **172**:841–878 (2001).

[40] M. Muradoglu, P. Jenny, S. B. Pope and D. A. Caughey, "Hybrid finite-volume/particle method for the PDF equations of turbulent reactive flows", *J. Comput. Phys.*, **154**:342–371 (1999).

[41] M. Muradoglu and D. A. Caughey, "Implicit multigrid solution of the multi-dimensional preconditioned Euler equations", *AIAA paper-98*, 0114 (1998).

[42] A. T. Norris and S. B. Pope, "Modeling of extinction in turbulent diffusion flames by the velocity-dissipation-composition PDF method", *Combust. Flame*, **100**:211–220 (1995).

[43] A. Olivani, G. Solero, F. Cozzi and A. Coghe "Near field flow structure of isothermal swirling flows and reacting non-premixed swirling flames", *Exp. Therm. Fluid Sci.*, **31(5)**:427–436 (2007).

[44] N. Peters, "Laminar flamelet concepts in turbulent combustion", *Proc. Combust. Inst.*, **21**:1231–1250 (1986).

[45] S. B. Pope, "A model for turbulent mixing based on shadow-position conditioning", *Phys. Fluids.*, **25**, 110803 (2013).

[46] S. B. Pope, V. Hiremath, S. R. Lantz, Z. Ren and L. Lu, "A Fortran 90 library to accelerate the implementation of combustion chemistry", http://tcg.mae.cornell.edu/ISATCK7 (2012).

[47] S. B. Pope, "Turbulent flows", Cambridge University Press, Cambridge (2000).

[48] S. B. Pope, "Lagrangian PDF methods for turbulent flows", *Ann. Rev. Fluid Mech.*, **26**:23–63 (1994).

[49] S. B. Pope, pdf2dv: A Fortran code to solve the modelled joint PDF equations for two-dimensional recirculating zones, Unpublished, Cornell University (1994).

[50] S. B. Pope , "On the relationship between stochastic Lagrangian models of turbulence and second-moment closures", *Phys. Fluids*, **6**:973–985 (1994).

[51] S. B. Pope, "Computations of turbulent combustion: progress and challenges", *Proc. Combust. Inst.*, **23**:591–612 (1990).

[52] S. B. Pope, "PDF methods for turbulent reactive flows", *Prog. Energy Combust. Sci.*, **11**:119–192 (1985).

[53] S. B. Pope, "Computationally efficient implementation of combustion chemistry using in situ adaptive tabulation", *Combust. Theor. and Model.*, **1**:41–63 (1997).

[54] V. Raman and H. Pitsch, "Large-eddy simulation of a bluff-body-stabilized non-premixed flame using a recursive filter-refinement procedure", *Combust. Flame*, **142**:329–347 (2005).

[55] C. Rotta, "Statistiche theorie nichthomogener turbulenz", *Z. Phys.*, **129**:547–572 (1951).

[56] D. H. Rowinski and S. B. Pope, "An investigation of mixing in a three-stream turbulent jet", *Phys. Fluids*, **25**, 105105 (2013).

[57] B. Sawford, "Lagrangian modeling of scalar statistics in a double scalar mixing layer", *Phys. Fluids*, **18**, 085108 (2006).

[58] D. G. Sloan, P. J. Smith and L. D. Smoot, "Modelling of swirl in turbulent flow systems", *Prog. Energy Combust. Sci.*, **12**:163–250 (1986).

[59] O. Stein and A. Kempf, "LES of Sydney swirling flame series: A study of vortex breakdown in isothermal and reacting flows", *Proc. Combust. Inst.*, **31**:1755–1763 (2007).

[60] Subramaniam and S. B. Pope, "A mixing model for turbulent reactive flows based on Euclidean minimum spanning trees", *Combust. Flame*, **115**:487–514 (1998).

[61] C. J. Sung, C. K. Law and J. Y. Chen, "Augmented reduced mechanisms for NO emission in methane oxidation", *Combust. Flame*, **125**:906–919 (2001).

[62] C. J. Sung, C. K. Law and J. Y. Chen, "An augmented reduced mechanism for methane oxidation with comprehensive global parametric validation", *Proc. Combust. Inst.*, **27**:295–304 (1998).

[63] M. S. Sweeney, S. Hochgreb, M. J. Dunn and R. S. Barlow, "The structure of turbulent stratified and premixed methane/air flames I: Non-swirling flows", *Combust. Flame*, **159**:2896–2911 (2012).

[64] Q. Tang, J. Xu and S. B. Pope, "Probability density function calculations of local extinction and no production in piloted-jet turbulent methane/air flames", *Proc. Combust. Inst.*, **28**:133–139 (2000).

[65] E. Turkel, R. Radespiel and N. Kroll, "Assessment of preconditioning methods for multidimensional aerodynamics", *Computers & Fluids*, **26**:613–634 (1997).

[66] E. Turkel, "Preconditioned methods for solving the incompressible and low speed compressible equations", *J. Comput. Phys.*, **72**:277–298 (1987).

[67] P.R. Van Slooten, Jayesh and S.B. Pope, "Advances in PDF modeling for inhomogeneous turbulent flows", *Phys. Fluids*, **10**:246–265 (1998).

[68] R. Weber, B. M. Visser and F. Boysan, "Assessment of turbulent modelling for engineering prediction of swirling vortices in the near burner zone", *Int. J. Heat and Fluid Flow*, **11**:225–238 (1990).

[69] P. Weigand, W. Meier, X. Duan, W. Stricker and M. Aigner, "Investigations of swirl flames in a gas turbine model combustor: I. Flow field, structures, temperature, and species distributions", *Combust. Flame*, **144**:205–224 (2006).

[70] J. S. Wong, D. L. Darmofal and J. Peraire, "The solution of the compressible Euler equations at low Mach numbers using a stabilized finite element algorithm", *Comput. Methods Appl. Mech. Engrg.*, **190**:5719–5737 (2001).

[71] J. Xu and S. B. Pope, "PDF calculations of turbulent non-premixed flames with local extinction", *Combust. Flame*, **123**:281–307 (2000).

[72] J. Xu and S. B. Pope, "Assessment of numerical accuracy of PDF/Monte Carlo methods for turbulent reacting flows", *J. Comput. Phys.*, **152**:192–230 (1999).

[73] GRI Mechanism 2.1, available from the World Wide Web site: http://www.gri.org.

[74] OpenFOAM, The open source CFD toolbox, OpenFOAM, http://www.openfoam.com/ (2013).

[75] University of Sydney, Clean combustion research group. http://sydney.edu.au/engineering/aeromech/thermofluids.